# Experimental Investigation into the Influence of Roughness on Friction and Film Thickness in EHD Contacts

By

Johan Guégan

A Thesis Presented in Fulfilment of the Requirements of the Degree of Doctor of Philosophy (Ph.D) and the Diploma of Imperial College

May 2015

Tribology Group

Department of Mechanical Engineering

Imperial College London

# Abstract

The roughness of machined surfaces such as those in bearings and gears is characterized by asperities which cover a wide spectrum of wavelengths and heights. When the height of the asperities becomes comparable to the lubricant film thickness, the roughness is known to influence friction and wear behaviour. This thesis reports an experimental investigation into the effect of roughness on the film thickness and friction in EHD contact. This work focuses on the particular roughness case of ridges oriented parallel to the rolling-sliding direction, such as the ones produced on raceways during the manufacturing process of rolling element bearings. To carry-out this research a ball-on disk test rig was used to model the contact between the ball and the ring of a ball bearing. The disks were made of glass to enable the lubricant film thickness to be measured through an optical technique based on optical interferometry. The ball specimens were made of AISI 52100 steel and they were roughened with a cutting tool, resulting in longitudinally oriented roughness ridges showing a dominant wavelength and amplitude. The friction was measured through a torque meter attached to the ball shaft.

A duo-chromatic system using two LEDs was developed in order to be able to measure the film thickness over a wider range of film thickness. A novel procedure was also introduced to enable the film thickness in rough EHD contacts to be measured accurately.

The film thickness and the friction produced by specimens with various amplitude and wavelength were measured under pure rolling and rolling-sliding conditions. The roughness was found to have a big influence on both film build-up and friction. In particular, under the same operating condition, a rough specimen will generate a thinner minimum film and a

higher friction compared to a smooth specimen. At the top of the asperities, a micro-EHD film was found to form. As suggested by friction and pressure measurements, the conditions in this micro film are severe enough to reach the limiting shear stress of the lubricant.

# Acknowledgements

First I would like to thank my supervisors Pr. Hugh Spikes and Dr. Amir Kadiric for their support throughout this PhD. I particularly appreciated the independence and the freedom I had in my work that allowed me to explore various research direction even if some were not successful in the end. I think it taught me a lot.

I would also like to thank SKF for funding this work and also the people from SKF who I had the opportunity to meet and have always been very helpful, in particular Guillermo, Pascal and Stathis.

I am very grateful for the help I received from Dr. Mark Fowell and Dr. Mourad Chennaoui when I had to implement changes to the test rig and for all the scientific discussion we had.

My time in this working environment had been very enjoyable mostly thanks to my lab mates/friend who introduced me to the English way of having a good time even though none of them were actually English.

Finally, I would like to dedicate this thesis to my family and to Laura who had to hear about it every evening and now probably knows my work better than I do, even though she is not an engineer.

# Declaration of Original Work

I, Johan Guegan, of Imperial College London hereby declare that this thesis is my own work and has not been submitted in any form for another degree or diploma at any other university or institution. Information obtained from published and unpublished work of others has been acknowledged. A list of references is included at the end of this thesis.



Johan Guegan

Date: 28th of May 2015

# Table of Content

# List of Figures

# List of Tables

# Chapter 1 - Introduction

This chapter introduces the PhD thesis. First the context of the research is presented and its objectives are listed. Then the approach chosen is explained, in particular the type of roughness studied is described and the necessity of improving the existing experimental methods is brought up. Finally the layout of the thesis is described.

## 1.1. Context of the Research

Machine elements such as gears and bearings are naturally rough due to their process of manufacture. Their surface asperities can cover a wide distribution of wavelengths and heights. When the contacting surfaces are fully separated by a thick lubricant film this has relatively little consequence. However, over the last few decades engineering components are becoming subject to increasingly severe operating conditions which, in turn, is resulting in a progressive reduction in film thickness down to values that are of the same order or thinner than the roughness asperity height. Thus many components now operate for long periods of time in the mixed-boundary regime, where the load is shared between the lubricant film and the asperities.

In rolling element bearings, the balls are usually very smooth, with root mean square roughnesses (RMS) of a few tens of nanometers. However the raceways are often relatively rough with RMS values of hundreds of nanometers (see Figure 1-1). Furthermore the machining processes used in the manufacture of rolling bearings does not produce isotropic roughness but structures that are dominated by ridges in the circumferential direction *i.e.* parallel to the rolling/sliding direction.

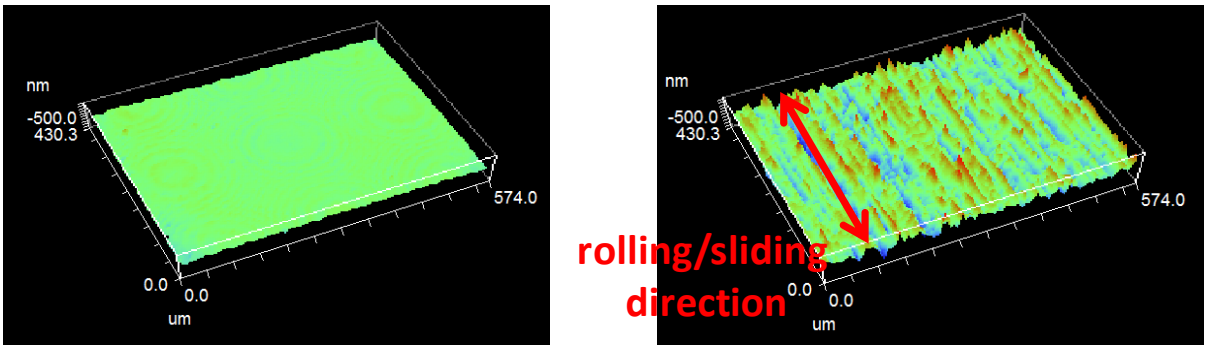


*(a)* *(b)*

***Figure 1-1:** Micro-geometry of (a) a Ball, RMS ≈ 10s of nm and (b) a Raceway, RMS ≈ 100s of nm*

Rolling bearings operate in the elastohydrodynamic (EHD) and mixed boundary/EHD regimes. While there has been extensive research on the EHD lubrication of smooth surfaces much less is known about the way that roughness affects lubrication in EHD and especially mixed EHD/boundary conditions. Of particular interest is the influence of roughness on film thickness and friction. We need to understand how surface roughness influences fluid entrainment and thus film thickness and how and when contacting asperities "lift-off" as the entrainment speed is increased, since this plays a role in surface damage and thus component life. Prediction and minimisation of friction in rolling bearings is becoming of increasing concern in order to improve bearing efficiency and there has been surprisingly little experimental study of how roughness influences friction in mixed EHD/boundary conditions.

## 1.2. Objectives

The objectives of this study are thus to investigate and thereby improve understanding of the influence of roughness texture on lubricant film build-up and the friction. In particular the transition from boundary, through mixed-boundary, to full EHD lubrication will be thoroughly analysed for longitudinal roughness, where the predominant roughness is parallel to the rolling direction, as present in rolling bearing raceways. The proposed formation of a very thin

separating film at the top of the asperities, sometimes known as “micro-EHD”, will be studied and quantified and the influence of “lift-off” on friction investigated.

## 1.3. Experimental Approach

### *1.3.1. Introduction*

In rolling bearings, smooth steel balls roll and slide against relatively rough raceways. In the current study this is mimicked by rolling/sliding roughened steel balls against flat glass surfaces.

The approach taken is a deterministic one, *i.e.* the ball specimens are defined by deliberately chosen geometrical properties with an idealized roughness, dominated by parallel ridges oriented along the rolling/sliding direction. These ridges are characterized by:

- A dominant wavelength λ
- A peak-to-valley height H

An example of a ball micro-geometry studied is shown in Figure 1-2. The specimens were produced by SKF by attaching the balls to a lathe and then carefully roughening them with a cutting tool. By varying the feed rate and the radius of the tool, it was possible to vary the wavelength and the peak-to-valley height of the textures.

As evident in this figure, the roughnesses are not perfect sinusoids but also show a secondary higher frequency. Phenomena involving this higher frequency (e.g. the running-in) are not within the scope of this project.

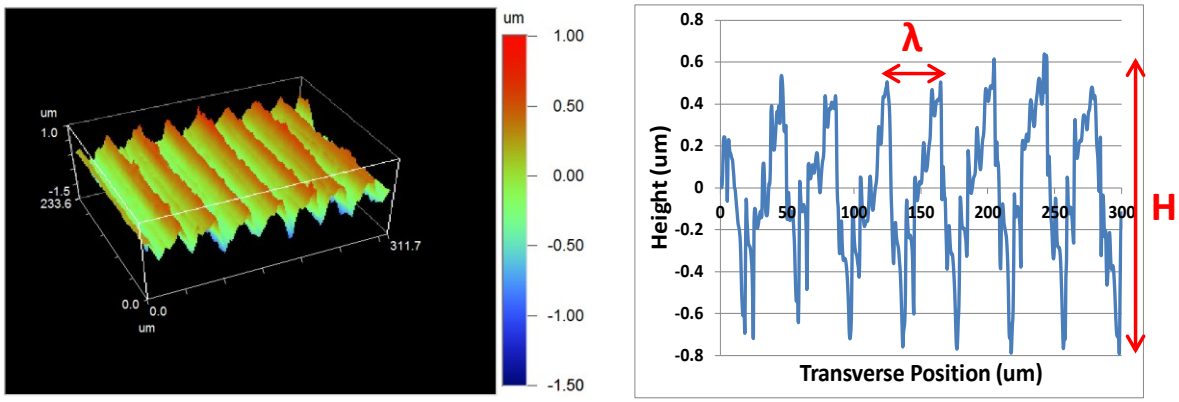


*(a)* *(b)*

***Figure 1-2:** (a) Surface micro-geometry showing the parallel roughness ridges and (b) transverse surface profile*

### *1.3.2. Development of Experimental Method*

The main apparatus used in this study is a customized ball-on-disk test rig. In this set-up a steel ball is loaded against a glass disk in order to produce a concentrated, non-conformal contact. The lubricant film thickness is measured with optical interferometry techniques and the friction force by a load cell attached to the ball shaft. Friction and the film thickness can be measured in parallel under the same operating conditions.

The test rig is normally employed to study smooth surface EHD and had to be modified to enable the study of rough surfaces. First, a new optical set-up, including a high-speed camera and better light sources was designed. Secondly an additional triggering system was developed to enable capture of optical images from the same position on the ball during successive measurements. Finally, the friction signal was diverted and amplified in order to provide a live measurement.

The existing protocol for film thickness measurement was found to be unsuitable to study very rough surfaces. A novel protocol was devised that provides full maps of film thickness in complex surfaces and has the advantage of automating the image processing.

### *1.3.3. Study of Longitudinal Roughness*

The film build-up and friction were measured under the same range of operating conditions for various roughness geometries and also for smooth surfaces.

From the measurements, phenomena such as the surface lift-off and roughness recovery were observed. The parallel measurements of the friction and the film thickness gave some important insights on the transition between the different lubrication regimes. Additionally, the film thickness maps were used in an inverse model to calculate the evolution of pressure with EHD film build up.

## 1.4. Thesis Plan

In this thesis, chapter 2 is an introduction to a number of important tribological concepts, necessary to understand the topic of this research. The basics of contact mechanics and lubricant rheology are introduced. Then the different measures of surface roughness and the different lubrication regimes are briefly described.

Chapter 3 and 4 are a review of the relevant previous experimental and theoretical work on rough surface EHD lubrication. Chapter 3 describes the various experimental methods used in EHD contact studies, in particular optical interferometry-based techniques for film thickness measurement. The effect on the film thickness and friction of the various geometries tested by previous workers is then summarised. Chapter 4 reviews previous theoretical work on rough EHD surfaces. First the techniques and the models used to solve EHD rough problems are presented, in particular the influence coefficient method that has been used to derive the pressure from the deformation is introduced. Some important findings are then listed.

Chapter 5 explains the experimental methods employed in the current study. The optical test rig used is described, along with the protocol and the test specimens. Developments of the test rig made by the author are described and explained. The novel approach to film thickness measurement required for this study is presented in some detail.

Chapter 6 presents film thickness measurements. The effect of the roughness parameters on the surface lift-off and roughness recovery are discussed.

Chapter 7 show the results of the friction measurement and the effect of the different roughness geometries is compared.

Chapter 8 presents the main conclusions from the work carried out and give some ideas for possible future developments.

# Chapter 2 - Background

This chapter introduces a number of common concepts in the field of Tribology. First some basics of contact mechanics are provided, in particular the Hertz theory. Then the importance of the lubricant viscosity for the lubrication of mechanisms is explained in terms of its influence on the friction and the lubricant film thickness. After that, the main parameters used to characterized surface roughness are listed. Finally the different regimes of lubrication are described along with some of their practical applications.

## 2.1. Contact Mechanics

When two bodies are loaded against each other they deform to a certain extent. If the load is small the deformation will be purely elastic and when load is removed the surfaces return to their initial states. If a higher force is applied, some of the features of the surfaces, or even the bulk surfaces themselves (indentation) may deform plastically.

In reality surfaces are always rough, and the pressure at the asperities of contacting bodies often becomes locally higher than the plastic limit. During rubbing, newly-manufactured mechanical components will have their asperity heights reduced until the roughness reaches a steady state; this phenomenon, which involves a combination of plastic deformation and wear, is called “running in”.

Though the roughness may affect the way the two bodies deform, it is also important to understand how ideally-smooth surfaces interact with each other. Two situations can arise depending on the geometry of the bodies. When the surfaces fit closely together, for example in a journal bearing/shaft contact, the contact is said to be *conforming* and the load is

distributed over a relatively large area. Such surfaces can only slide against one another, rolling contact is not possible. On the contrary, when the curvatures of the bodies are quite different the load is supported by a much smaller area and the surface are called *non-conforming*. The latter case is of great practical interest for components whose elements roll as well as slide together such as rolling element bearings and gears.

The theory of how two *non-conforming* smooth bodies deform when they come into contact was first formalized by Hertz [1], but a more accessible version is available in Johnson [2].

The assumptions made are:

- The surfaces are smooth and non-conforming
- The strains are negligible (elastic deformation)
- The domain considered is a half space with the contact size being negligible compared to the thickness of the bodies
- The contact is frictionless

According to Boussinesq, the deformation ***dw*** at a distance *r* caused by a point force ***dP*** is:

$$dw(r) = \frac{1-\nu^2}{\pi E}\frac{dP}{r} \qquad \textbf{(1)}$$

where ***E*** and ***v*** are respectively the Young's modulus and the Poisson's ratio of the material.

Considering the two bodies in contact and integrating over the contact area.

$$w = w_1 + w_2 = \frac{1}{\pi E^*}\iint_S \frac{p(x',y')dx'dy'}{\sqrt{(x-x')^2+(y-y')^2}} \qquad \textbf{(2)}$$

with:

$$\frac{1}{E^*} = \frac{1-\nu_1^2}{E_1} + \frac{1-\nu_2^2}{E_2}$$

$E^*$ is called the reduced modulus and combines the mechanical properties of the two bodies. In the case of a circular area of contact, it can be shown that the pressure distribution:

$$p = p_0\left(1 - \left(\frac{r}{a}\right)^2\right)^{1/2} \quad \textbf{(3)}$$

gives rise to a displacement that satisfies the boundary conditions of two solids in contact.

Here $a$ is the contact radius or semi-width and the maximum pressure $p_0$ is usually referred to as the "Hertz pressure". If $P$ is the applied load, the semi-width is:

$$a = \left(\frac{3}{4}\frac{PR}{E^*}\right)^{1/3} \quad \textbf{(4)}$$

and the Hertz pressure:

$$p_0 = \frac{1}{\pi}\left(\frac{6PE^{*2}}{R}\right)^{1/3} = \frac{3}{2}\frac{P}{\pi a^2} = \frac{3}{2}\bar{p} \quad \textbf{(5)}$$

where $\bar{p}$ is the mean pressure. $R$ is the radius of relative curvature, found by summing the curvatures of the two surfaces ($1/R = 1/R_1 + 1/R_2$), where $R_1$ and $R_2$ are the radii of the contacting bodies).

In most of the experiments described in this thesis the load applied is 20 N and the two solids in contact are a 19.05 mm (¾") diameter steel ball and the flat surface of a glass disk. In the nominally smooth case the contact semi-width is expected from Hertz theory to be 0.135 mm and the Hertz pressure to be 0.53 GPa.

## 2.2. Lubricant Viscosity

The most important property of a lubricant is its viscosity. For example, this becomes visible when a fluid is poured; a fluid with a low viscosity will flow very rapidly while a more viscous one will move more slowly. In simplistic terms this comes from the fact that when a layer of molecules in a fluid moves past a neighbouring layer it will interact with that layer which will generate a shear stress.

In the case of a film of lubricant between two parallel sliding surfaces, the viscosity will generate a force that will oppose to the sliding velocity. This force is usually referred to as the *friction force*. Historically, Newton was the first to link the friction force, through the *shear stress, $\tau$,* to the *strain rate* (or *shear rate*) which is the gradient of velocity through the film thickness.

$$\tau = \eta \frac{dU}{dz} \approx \eta \frac{U_S}{h} \qquad (6)$$

where $\boldsymbol{U_S}$ and $\boldsymbol{h}$ are respectively the sliding velocity and the lubricant film thickness. The friction force is simply the shear stress integrated over the area of the sliding surface. Physically, in a lubricant film every layer of fluid influences the motion of the layers immediately above and below it. If the layer is faster it will slow the other down, if it goes slower it will accelerate it. The parameter $\boldsymbol{\eta}$ that links the motion to the force is called the *dynamic viscosity*. When divided by the density of the fluid, this value gives what is called the *kinematic viscosity.* Newton's hypothesis was that the dynamic viscosity does not depend on the strain rate or the history of the lubricant. This is not always true, so that the category of lubricant that respects those two principles was named after him, they are called *Newtonian Fluids*. However, especially at very high shear rates, lubricants have a tendency to behave in

a non-Newtonian way and most oils show a viscosity drop. This phenomenon is known as *shear-thinning* and can occur when the molecules present in the lubricant align along the shearing direction but also simply when the fluid is subject to very high shear stresses. Various equations have been proposed to describe this phenomenon by relating shear stress to strain rate. In particular the Eyring model is often favoured by many tribologists, while the Carreau-Yasuda model is more widely used by rheologists. The Eyring formula is:

$$\tau = \tau_E sinh^{-1}\left(\frac{\eta(p)\dot{\gamma}}{\tau_E}\right) \quad \textbf{(7)}$$

where $\boldsymbol{\tau}$ is the shear stress, $\boldsymbol{\dot{\gamma}}$ is the strain rate and $\boldsymbol{\eta(p)}$ is the Newtonian dynamic viscosity (the bracketed **(*p*)** indicates that this is dependent on the contact pressure). The "Eyring stress" $\boldsymbol{\tau_E}$ is the shear stress above which shear thinning starts to become significant. Since $\boldsymbol{sinh^{-1}(x) \approx x}$ when $\boldsymbol{x \approx 0}$, if $\boldsymbol{\eta(p)\dot{\gamma} << \tau_E}$ then equation (7) becomes equation (6).

Equation (6) and (7) suggest that the best lubricant should have the lowest viscosity possible in order to obtain a low shear stress and thus a low friction to reduce the energy loss. However in the hydrodynamic and elastohydrodynamic lubrication (EHD) regimes the lubricant film thickness is dependent on the viscosity, so a lower viscosity also leads to a thinner fluid film. For instance, for a given operating condition a lubricant A whose viscosity is three times the viscosity of a lubricant B will generate a film that is more than 2 times thicker in the elastohydrodynamic regime, hence it will require a lower entrainment speed to transition from the mixed-boundary regime to the full EHD regime. (The concepts of hydrodynamic, elastohydrodynamic and mixed lubrication are described in section 2.4 below).

The viscosity of a lubricant depends on both the temperature and the pressure, falling with increasing temperature and increasing with pressure. The dependency on pressure is

extremely important in the elastohydrodynamic regime, where the pressures can reach several GPa. If the viscosity were constant with pressure, in those conditions the fluid film would not be more than a few molecular layers thick. Equation (8) is called the *Barus equation* and gives a relationship between the viscosity at atmospheric pressure $\boldsymbol{\eta_0}$ and the pressure $\boldsymbol{p}$.

$$\eta = \eta_0 e^{\alpha p} \tag{8}$$

The coefficient $\boldsymbol{\alpha}$ is the pressure-viscosity coefficient and for oil-based lubricants its value is usually of order 10 to 20 $GPa^{-1}$. While the Barus equation is usually only accurate up to about $10^8$ Pa, it shows how sensitive viscosity is to pressure for a given lubricant. This effect of the pressure on the viscosity is called *piezo-viscosity*. At higher pressures, other pressure-viscosity equations have been proposed (Chu and Cameron [3], Roelands [4]).

While viscosity increases with increasing pressure, it decreases with increasing temperature. Several equations have attempted to predict the reduction of the dynamic or kinematic viscosity with temperature (Crouch and Cameron [5], Roelands [4]).

The ASTM (American Society for Testing Materials) has a standard method to calculate the drop in kinematic viscosity with temperature for liquid lubricants (ASTM D341-722). It requires the measure of the kinematic viscosity at two temperatures, usually 40°C and 100°C. The viscosity at other temperatures can then be interpolated using this formula:

$$loglog(\nu + 0.7) = a - b\, log(T) \tag{9}$$

The equipment used to measure the viscosity will be described in the chapter 5.

## 2.3. Surface Roughness

Even the most thoroughly polished surface will exhibit some form of surface roughness. This can come from the manufacturing process (*e.g.* honing, grinding) or it can be artificially produced in order to achieve specific tribological performance (*e.g.* laser texturing, see Kligerman et al. [6]).

In the latter case, the deterministic nature of the roughness usually implies that the best description is a geometric one. For example, the knowledge of the depth and the radius of circular dents or the amplitude (or peak-to-valley height) and the wavelength for sinusoidal textures will provide a satisfactory description.

For random roughness, statistical measures are required. To characterize the height distribution of a rough surface, two parameters are usually calculated. The $R_a$ or Centre Line Average (CLA) is the average distance to the centre line, along a line of length L:

$$R_a = \frac{1}{L}\int_0^L |z|\, dx \tag{10}$$

The $R_q$ or *Root-mean-square (**RMS**)* corresponds to the standard deviation of the height distribution:

$$R_q = \sqrt{\frac{1}{L}\int_0^L z^2\, dx} \tag{11}$$

Two surfaces with different roughness can have the same height distribution. For example if the asperities have the same height but the average distance between peaks is double for one of the surface, the $R_a$ and the $R_q$ might not be affected; however the spatial distribution will be completely different. There are different ways to describe the latter; one important

technique consists in calculating the autocorrelation function (see Thomas [7] for a detailed description). This describes how self-similar the surface is.

In the current research, the surface roughnesses studied can be considered semi-deterministic in the sense that they have a definite structure (parallel ridges) but the way they are produced allows a significant random component to their geometry. Usually a mix of statistical parameters ($\boldsymbol{R_a}$ and $\boldsymbol{R_q}$) and deterministic ones (wavelength and peak-to-valley height) will be used.

In real applications both the surfaces in contact are rough and the *composite roughness* is usually calculated:

$$R_q = \sqrt{R_1^2 + R_2^2} \tag{12}$$

## 2.4. Regimes of Lubrication

A contact is said to be "lubricated" when a third body is put between two contacting surfaces in order to avoid direct solid-solid contact between them. The most common lubricants are usually liquids, typically mineral, natural or synthetic oils, which enable the surfaces to be separated and reduce or eliminate direct asperity contact. While solid lubricants such as PTFE coating are very common in kitchenware, they are also present in engineering components either where environmental conditions forbid the use of liquids (*e.g.* at very low temperature for space applications) or in low-cost, lightly-loaded domestic applications to avoid a lubricant supply system. Gases can also be used as lubricant. Hovercrafts hover above water thanks to a cushion of pressurized air. In air bearings the contacting surfaces are only separated by a film of air, thus they have extremely low friction, which is critical in certain high-speed

applications such as dentist drills. However neither the solid nor the gases lubricants provide the same combination of low friction and high load-bearing capacity as fluid lubricants.

Depending on the operating conditions (entrainment speed, load) different lubrication regimes can be identified:

- The *Boundary Regime* where the high spots or "asperities" of the two surfaces are in contact and support all the applied load. The lubricant present does not provide any load support. This is normally the regime where the friction force is the highest, and it can approach the dry (unlubricated) friction coefficient. Friction can be reduced in this regime by using certain additives in the lubricant that adsorb or react on surfaces to form low shear strength films.
- The *Mixed-Boundary Regime* where there is still solid-to-solid contact, but part of the load is born by the pressurised lubricant flowing between the asperities. In these conditions, the friction drops as the entrainment speed and thus the lubricant film thickness increases.
- In full film conditions the entire load is supported by the pressurised lubricant film. If the contact is conformal and the load not high enough to deform the surfaces significantly or increase the lubricant viscosity, the contact operates in the *Hydrodynamic Regime* (HD). If the contact is non-conformal, the high contact pressure will both deform the surfaces and increase the lubricant viscosity and the regime is called *Elastohydrodynamic* (EHL or EHD). Unless thermal effects are extreme (at very high sliding speeds), the friction will rise as the sliding speed and thus the strain rate increases, following equations (6) and (7).

All of the above regimes are important to understand lubrication performance since during their life almost every mechanical component has to operate in the boundary and mixed-boundary regimes, not just in full film conditions. For example at the start-up of a motor the lubricant film in the bearings can be very thin as the entrainment speed is still low or if you consider a piston, its dynamics means that twice per cycle the entrainment speed becomes zero.

Depending on the practical application, a wide range of film thicknesses and also surface roughnesses may be present, so it is not always straightforward to identify the regime of lubrication in which a certain machine operates. Thus researchers and engineers often look at the ratio of the film thickness and the roughness. This parameter is called the *lambda ratio*.

$$\lambda = \frac{h}{R_q} \tag{13}$$

Empirically the following ranges have been found:

- Boundary regime: λ < 0.01
- Mixed-Boundary regime: 0.01 < λ <2-5
- Full film: 2 -5< λ

The EHD regime can be observed in a wide range of applications where the contact is non-conformal such as rolling element bearings, gears or cams. This work focuses on such concentrated contact and looks particularly at the transition from boundary, through mixed to the EHD lubrication.

# Chapter 3 - Review of Previous Experimental Work on EHD

This chapter reviews the existing experimental studies on smooth and rough contact EHD. The studies on film thickness, friction and pressure are described in three different parts. In the first part, various methods of film thickness measurements are described before the emphasis is put on the methods based on optical interferometry. Following that, the characteristics of smooth EHD contacts are explained. Various types of texture geometries and their effect on the lubricant film thickness build-up are examined. In the second part, the topic of EHD friction is addressed. Some important measurements techniques are listed and general findings in the smooth and rough cases are presented. The third part is about the pressure distribution in EHD contacts. The main techniques and their benefits are described along with some important results.

## 3.1. Film Thickness

### *3.1.1. Measurement Techniques*

#### 3.1.1.1. Early Techniques to Measure EHD Film Thickness

The topic of lubrication in non-conforming contacts has been subject to many investigations since the 2nd World War. One of the first issues tribologists addressed was to determine if there is a lubricant film in such contacts and if there is how much there is and how it is distributed.

To answer this question, several techniques were developed, using various physical phenomena. Historically, the first experimental studies were based on the measurement of the lubricant film capacitance in a lubricated roller in line contact by Crook [8] and in point

contact by Archard and Kirk [3]. However this required assumptions of the shape of the contact, which was calculated through Hertz theory (Dyson et al. [10]). For rough surfaces this technique is now often coupled with the contact resistance measurement, in which case the amount of solid-to-solid contact can be estimated since a low resistance means that a lot of asperities are interacting. In particular it can be used to find the lift-off speed at which the lubricant film provide full separation of the contacting surfaces thicker than the highest asperity (see for example Heemskerk et al. [11] ). This speed is important as it is linked to the transition from the mixed lubrication regime to the full EHD regime. Another technique developed in the 1960s involved the use of X-rays which enabled the measurement of film as thin as 50 nm (Sibley and Orcutt [6]).

These early studies were important as they provided the first experimental confirmation of the theoretical predictions of Grubin [13], for example that even at very high pressure there is still a significant lubricant film between the surfaces or that the film thickness drops sharply at the exit of the contact (constriction).

#### 3.1.1.2. Current Techniques

Since these early studies, several other techniques have been invented to measure lubricant film thickness. Table 1 lists the main techniques used nowadays to measure EHD films and gives their respective advantages and disadvantages. Optically-based methods such as interferometry and fluorescence have the major disadvantage of requiring a transparent surface and thus not being directly applicable to real bearings or gears. Moreover the use of a transparent material usually means using glass, which has very different mechanical properties from steel (although using sapphire can address this issue). However they provide the easiest approach to measuring how film thickness varies across a contact and are also

able to span a very wide film thickness range, from films of a few nanometers or less up to several microns.

***Table 1:* Modern techniques used in EHD films investigation**

| | Techniques | Comments | Key Reference |
|---|---|---|---|
| **Electrical Techniques** | Contact Resistance | + Can be used on real mechanism<br>+ Fractional contact measurement<br>− No film thickness measurement | Furey [14] |
| | Capacitance | + Can be used on real mechanisms<br>− Requires the shape of the contact to be well known<br>− Measure the mean film thickness | Heemskerk et al. [11] |
| | Sputtered Capacitance | + Local measurement<br>− One of the surface cannot be conductive | Crook [15] |
| **Optical Techniques** | Ultra-Thin Film Interferometry | + Range: 1 nm to > 1 µm with 1 nm resolution<br>− Requires one transparent and one reflective surface<br>− measurements only at a single point or along a line within the contact (not maps) | Johnston et al. [16] |
| | Space Layer Imaging Method (SLIM) | + Enables thin film measurements with 4 nm resolution<br>+ Gives full film thickness maps<br>− Requires one transparent and one reflective surface<br>− Maximum measurable film limited by light coherence | Cann et al. [17] |
| | Relative Optical Interference Intensity | + Very thin film measurement (< 1 nm)<br>− Limited to thin films | Luo et al. [18] |
| | Fluorescence | + Very thick film measurement (several µm)<br>− No resolution for films below a few 100s nm | Reddyhoff, Choo, et al. [19] |
| **Other** | Ultrasound | + Can be used on real mechanism<br>− Low resolution<br>− Does not work with very thin films | Reddyhoff and Harper [20] |

### 3.1.1.3. Basics of Optical Interferometry

The application of optical interferometry to study of EHD contacts was pioneered by Cameron and Gohar [21], though Kirk [22] made an initial contribution by looking at the Newton's rings in a hydrodynamic contact between crossed cylinder made of Perspex. The advantage of

optical interferometry is that it can give a very detailed map of the film distribution and has a much better accuracy than most other techniques.

To explain the principle of optical interferometry, consider two surfaces separated by a thin layer of air, the upper one being made of a transparent material such as glass, the lower being made of a reflective material such as steel. When light is shone at the contact, part of the beam will be reflected at the interface glass/air because of the difference in refractive index between air and glass; the rest will be reflected by the lower surface. The two beams will have travelled different distances which will generate a phase difference between them. When they recombine, interference fringes will appear depending on this difference of phase.

Liquid lubricants generally have a refractive index of about 1.45 which is very close to the refractive index of glass. Consequently, when the contact is filled with lubricant the beam is not split at the interface glass/oil. Initially authors used special glass with high refractive index (Cameron and Gohar [21]) or even diamond (Gohar and Cameron [23]) to obtain interference fringes. However, with the development of coating technologies it has become more common to coat the lower surface of a plain glass disk with a semi-reflective layer such as chromium (Foord et al. [24]). As shown in Figure 3-1 the wavelengths that interfere will depend on the gap, or film thickness.

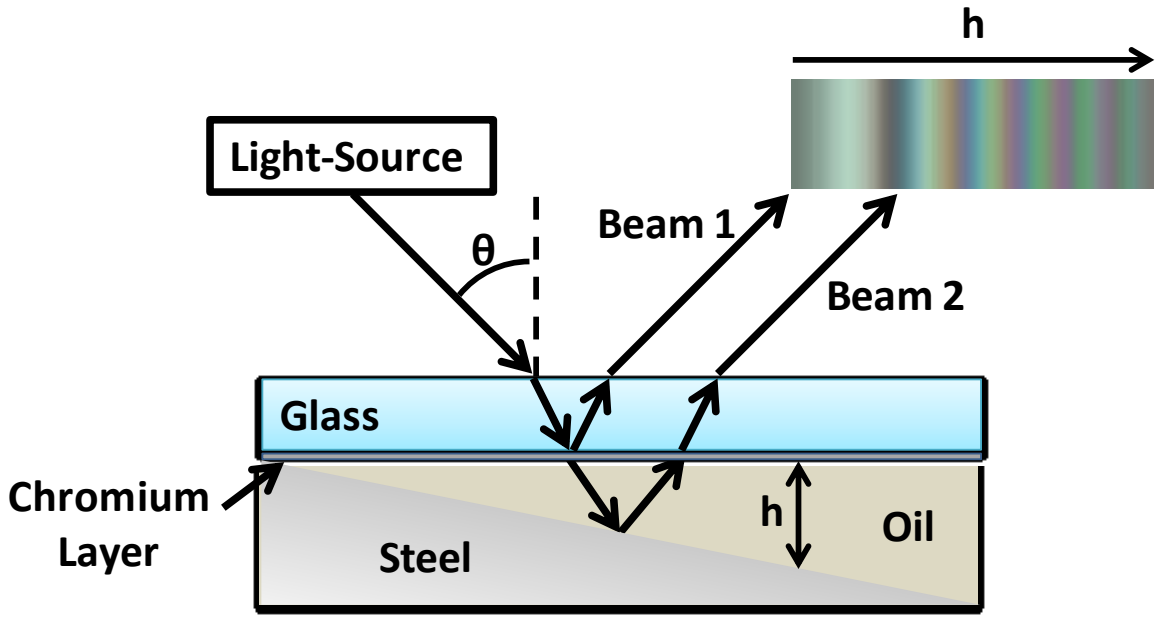


***Figure 3-1:** Schematic illustrating the interference phenomenon with a wedge*

For a given wavelength $\boldsymbol{\lambda}$ it can be shown that the variation of fringe intensity with film thickness is (see Hariharan [25]):

$$I = I_1 + I_2 + 2\sqrt{I_1 I_2}\cos\left(\frac{2\pi}{\lambda}.2nh_{oil} + 2\pi\varphi\right) \quad \textbf{(14)}$$

where $\boldsymbol{I_1}$ and $\boldsymbol{I_2}$ are the maximum intensities of the two beams and $\boldsymbol{\varphi}$ is a constant phase shift due to the chromium layer. The value of this constant is usually very small and depends on the thickness of the chromium layer; in the current work the disk supplier tuned the thickness so that $\boldsymbol{\varphi = 0}$. The term within the cosine is the difference of phase $\boldsymbol{\Delta\Phi}$, and the product of the distance $\boldsymbol{2h_{oil}}$ and the refractive index $\boldsymbol{n}$ is called the optical path difference.

It is evident that for a monotonically-increasing difference of path, the intensity will go through maxima and minima at regularly spaced value of $\boldsymbol{h}$. If $\boldsymbol{\lambda}$ is the wavelength, the maximum intensity, or *constructive interference*, will occur when:

$$\mathrm{h_{max}} = \frac{\mathrm{N} - \varphi}{2\mathrm{n}}\,\lambda \quad \textbf{(15)}$$

and the minimum intensity (*destructive interference*) when:

$$h_{min} = \frac{N - \varphi - \frac{1}{2}}{2n} \lambda \quad \textbf{(16)}$$

***N*** is called the order of interference and is a positive integer. Knowledge of its value is critical since, for example, an error of one order will generally result in an error of around 200 nm into the film thickness calculation, which is significant since the film thicknesses being studied are usually below 1 micron thick. It can be noted that the period of the fringes is $\frac{\lambda}{2n}$ and the distance between destructive and constructive interference (or half-period) is $\frac{\lambda}{4n}$.

In the case of a non-conforming contact such as a ball on flat, the distance between the two surfaces will vary over the plane of observation and so will the extent of optical interference and thus the fringe intensity. In particular, the points that have the same separation between the two surfaces will create fringes with the same intensity, generating contours connecting them. Such an image is often called interferogram. Figure 3-2 shows an interferogram of a static, loaded contact between a glass disk with a chromium coating and a steel ball. The contact has been illuminated by a near-monochromatic, red light source.

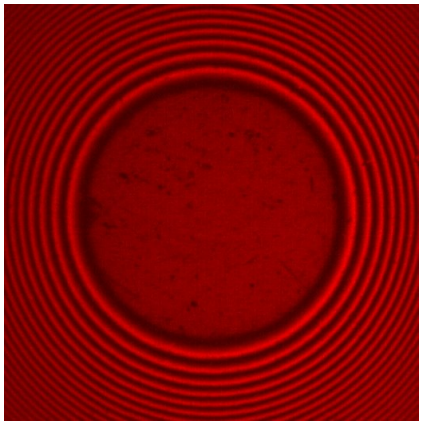

***<u>Figure 3-2:</u> Image of a static contact between a glass disk and a steel ball illuminated with red light (617 nm)***

A large circular area of relatively homogeneous intensity appears in the middle of the image. This is the contact zone where the difference of path is 0. Outside the contact zone, the gap between the two surfaces increases and because of the ball on flat geometry the contours are concentric circles, which are known as Newton's rings.

#### 3.1.1.4. Measuring Methods

##### (a) Manual Analysis

Once the appropriate set-up is found, several methods can be used to analyse interferograms. Historically in lubrication research, measurements were based on naked eye observation of the fringes and either counting them for monochromatic light or comparison with a table linking their colour to film thickness (see Cameron and Gohar [21] and Foord et al. [24]) for white light. If white light is used, it is theoretically possible to achieve maximum resolution, as for every possible gap there will be a wavelength constructively interfering. By carefully observing the resulting colour in the contact, it is possible to map the film thickness in the contact (see Figure 3-3).

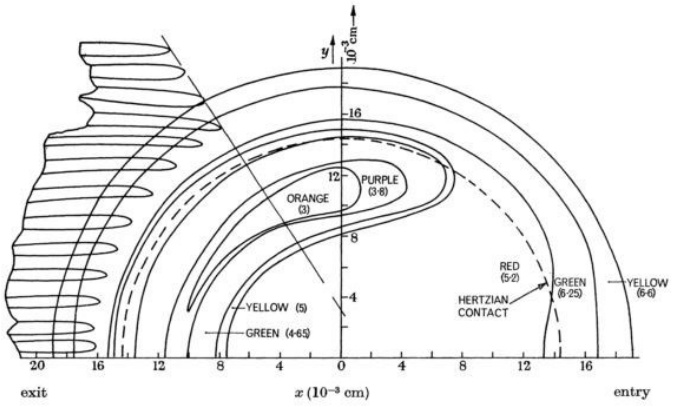


***Figure 3-3:** Example of film thickness map obtained by visual identification of the colours (from Cameron and Gohar [21])*

Regardless of how tedious this method can be, especially if "complex" cases such as rough surfaces are considered, the technique has other disadvantages. First, the visibility (or contrast) of the interference fringes produced by a broad light source vanishes quickly as the

gap increases, which limits the range of film thickness that can be measured. To be able to measure thicker films, a light source with a narrower spectrum produces interference fringes with a better visibility. Hence monochromatic light has been used by several authors to study lubricant film. In this case the images are analysed in terms of intensity and only the position of the constructive and destructive interferences are identified, so that the measurements are discrete. However, one disadvantage of using monochromatic light sources over white light lies in the fact that, the order of interference needs to be determined while, in theory, the "colour" of the fringes generated by a white light are sufficient to get the measure the film thickness. To improve the resolution of monochromatic interferometry, an evolution called duo-chromatic interferometry was developed by Wedeven [26] in 1970. This consists in using two monochromatic light sources instead of one. Practically, this dual illumination was achieved by using two different filters with a Xenon flash lamp which has a broad spectrum and emits in the entire visible range. This technique is still used by some authors (see, Kaneta, Sakai et al. [27]). In this case, a sequence of colours is generated by the superimposition of the two wavelengths which makes the identification of the order of interference much easier

These early techniques enabled the study of almost all type of lubricated contact problems including starvation, Wedeven et al. [28], and rough contacts, Cusano and Wedeven [29]. However they relied heavily on the diligence of the experimentalist and his or her capacity to identify and analyse the interference fringes. In the case of the white light experiments, since the colour perception varies from one person to the other, the use of a colour chart is far from absolute. Also a major limitation with these techniques is that they are limited to the

films that are thicker than a quarter wavelength, as they need either full constructive or destructive interference to occur.

To address this latter issue, Westlake and Cameron [30] proposed the use of a deposited, transparent silica layer on the top of the semi-reflective layer in order to offset the film thickness and obtain interference fringes at much thinner films. Even though Westlake and Cameron [31] successfully implemented it to study a squeezed film, this idea was not developed further for another 20 years, until Spikes and Guangteng [32] employed a sputtered wedge of silica on a disk to offset the film thickness.

### (b) Thin Film Interferometry

Probably the most important development that established interferometry as the main technique for film thickness measurements came from Johnston et al. [16] who invented the technique now called *ultra-thin film interferometry*. This combines a transparent disk with a spacer layer and a spectrometer to analyse the spectral content of an interferogram. This is an important step as it enables the first absolute and objective way of studying interference fringes in lubricated contacts.

As shown in Figure 3-4 the central element of the spectrometer is a diffraction grating that separates the incoming light into its component wavelengths. To do so, it spreads them along one dimension. If the entire image were fed to the spectrometer, the light coming from different X positions would get mixed in the frequency domain which would confuse the measurements. Consequently, a spectrometer cannot be used to analyse an entire image at the same time, it has to be split into thin lines. Hence, in this set-up a thin slit splits the image at the entrance of the spectrometer. In the case of smooth circular EHD contacts, the

transverse or longitudinal diameters are selected, so that the side lobe or rear constriction can be measured.

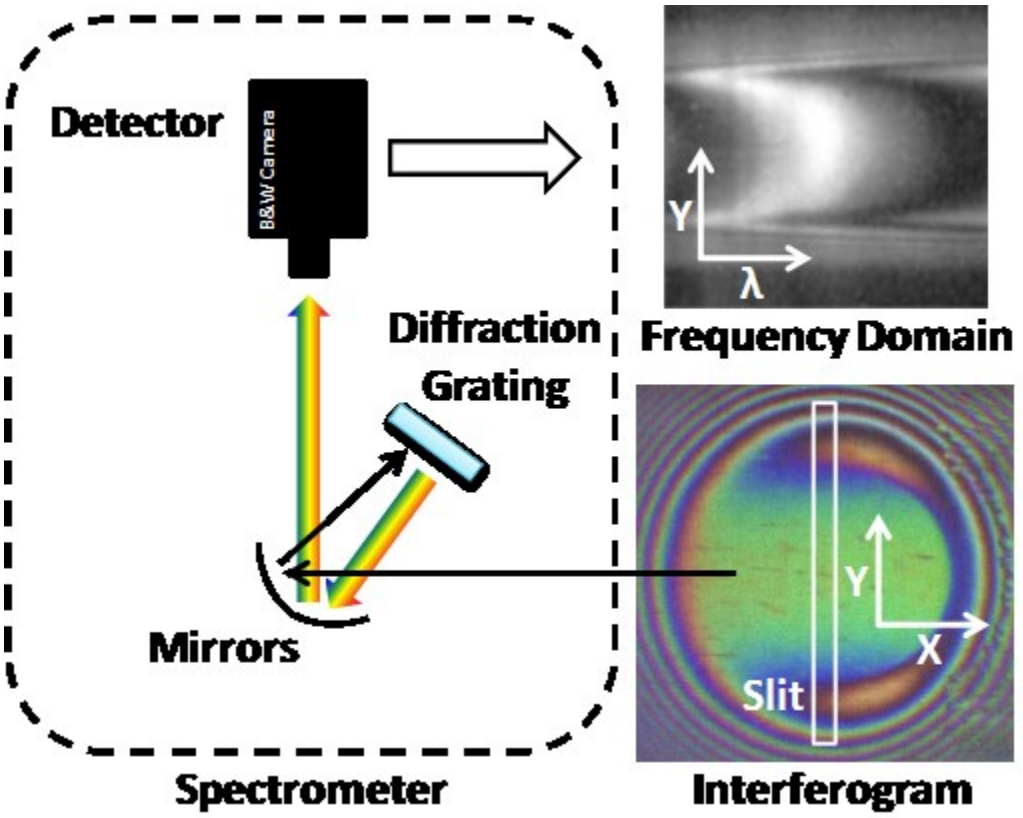


***Figure 3-4:** Schematic of a spectrometer used for the measure of film thickness in Tribology*

In the frequency domain image of Figure 3-4 a more intense zone appears which corresponds to the wavelength that maximally constructively interferes at this speed. As there is a spacer layer on the top of the lubricant, all the measurements will be offset by its thickness. To obtain this spacer layer thickness, the "film" is measured in static dry conditions at the beginning of a test. The refractive index of the spacer layer is different from that of the lubricant so the spacer layer thickness cannot just be subtracted from the absolute film thickness. In static dry conditions the difference of path is:

$$2n_{SL}h_{SL} = (\mathrm{N_{SL}} - \varphi)\lambda_{\mathrm{SL}} \quad \textbf{(17)}$$

where the subscript ***SL*** designates the values for the spacer layer.

In lubricated conditions:

$$2n_{SL}h_{SL} + 2n_{Oil}h_{Oil} = (\mathrm{N_{SL+Oil}} - \varphi)\lambda_{\mathrm{SL+Oil}} \quad \textbf{(18)}$$

This gives the modified equation for equation (15):

$$h_{Oil} = \frac{(\mathrm{N_{SL+Oil}} - \varphi)\lambda_{\mathrm{SL+Oil}} - (\mathrm{N_{SL}} - \varphi)\lambda_{\mathrm{SL}}}{2n_{Oil}} \quad \textbf{(19)}$$

An alternative technique to measure very thin films without a spacer layer was introduced by Luo et al. [18] and involved measuring carefully the intensity variations in the contact when using a monochromatic source. To do so they re-wrote equation (14) and introduced the concept of relative optical interference intensity (ROII):

$$\bar{I} = \frac{2I - I_{max} - I_{min}}{I_{max} - I_{min}} = cos\left(\frac{4\pi nh}{\lambda} + \Phi\right) \quad \textbf{(20)}$$

where ***I*** is the local intensity and $\boldsymbol{I_{max}}$ and $\boldsymbol{I_{min}}$ are the adjacent minimum and maximum in the interference order. Then the film thickness can be expressed by a simple analytical relationship:

$$h = \frac{\lambda}{4\pi \mathrm{n}}(\arccos(\bar{I}) - \Phi) \quad \textbf{(21)}$$

Using these techniques the accuracy of the film thickness is said to be as low as ±1 nm (Johnston et al. [16]) and enables the measurements of very thin boundary films (Guangteng and Spikes [33] and Smeeth et al. [34]). However due to the way the spectrometer works, only a slice of the contact can be measured at a time which is suitable for well-structured lubricant films. When more complex film structures are encountered, such as contacts with roughness features (Guangteng et al. [35]) or dimple formations (Kaneta, Nishikawa, et al. [36]), it is usually necessary to image and map the film thickness over the entire contact.

### (c) Imaging Techniques

The solution came with the generalization of colour charge-coupled device (CCD) cameras. Several colour spaces exist, the RGB (red green and blue) being the most natural as it corresponds to the cone cells of the human eyes. However, authors have used various colour spaces such as Lab (Hartl et al. [37]) or HSL (hue-saturation-lightness), (Gustafsson et al. [38]) to study interferograms. Gustafsson et al. [38] were the first to use digitalized images to obtain full maps of EHD contacts. He was later followed by other researchers (Cann et al. [17], Hartl [39], Molimard [40]).

The imaging techniques reported by different researchers do not differ in theory but in the various colour spaces employed and the way of obtaining the relationship between the pixel values and the film thickness, also known as calibration curves. The most common approach has been to relate the well-defined and varying gap between the ball and a flat with the pixel values measured from an interference image. Gustafsson et al. [38] brought a ball in contact with a glass disk but did not apply any load so that the gap was entirely defined by the undeformed geometry (sphere). Producing a contact without loading is very difficult to achieve, so instead Cann et al. [17] used a static loaded contact which they analysed with ultra-thin film interferometry to obtain the radially-varying gap, which they then related to the hue of the interference image. Hartl [39] used the Newton rings coming from a monochromatic interferogram to obtain the gap on a static contact while Molimard [40] obtained the gap using Hertz theory. The group from Imperial College later used *ultra-thin film interferometry* to measure the central film thickness versus speed on a very smooth ball and then took interference images over the same speed range to follow the evolution of the colour intensities in the central area (Choo, Olver, and Spikes [41]).

Marklund and Gustafsson [42] developed a trichromatic set-up using a light source having three well defined wavelengths to illuminate the contact. The results are interferograms with a very good fringe visibility compared to white light-illuminated interferograms as can be seen in Figure 3-5.

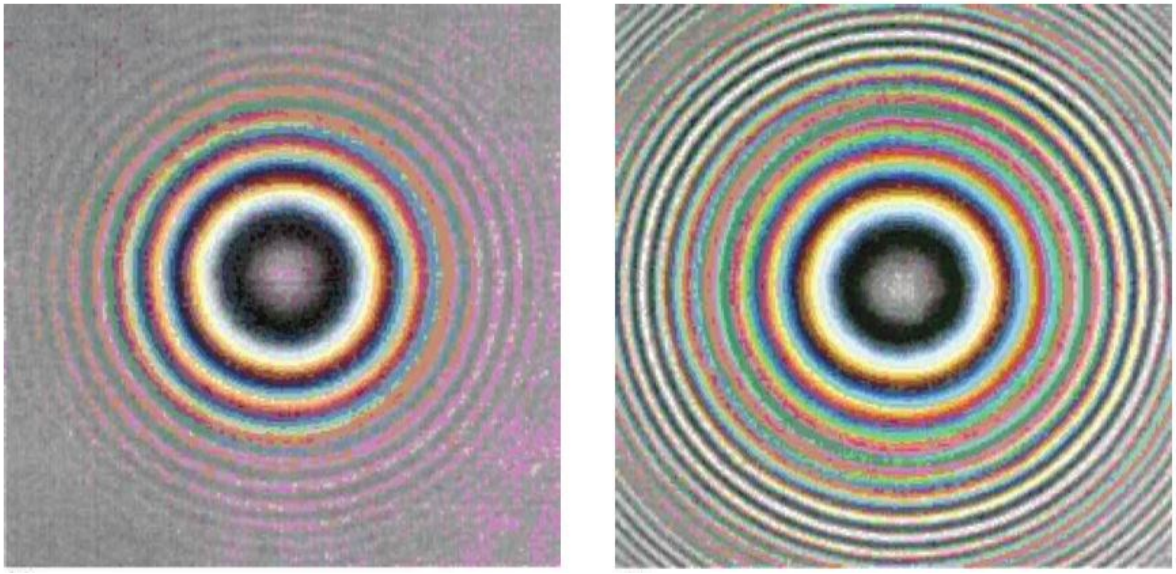

***(a)*** ***(b)***

***<u>Figure 3-5:</u> Ball in contact on a ball-on-disk set-up; (a) white light illumination and (b) trichromatic light source (from Marklund and Gustafsson [42])***

### *3.1.2. Experimental Studies of EHD Contact*

#### 3.1.2.1. Smooth Contact

Experimental measurements showed that at low speeds, the shape of the contact is approximately Hertzian, which means that the film is essentially flat in the central area. At higher speeds, Crook [15] found using a capacitance technique that a reduction of film thickness (or constriction) could be observed at the exit of the contact. Later Cameron and Gohar [21] studied a lubricated point contact via optical interferometry. They observed the now classical EHD film distribution with a flat central area and a horse-shoe shaped constriction at the exit (see Figure 3-6).

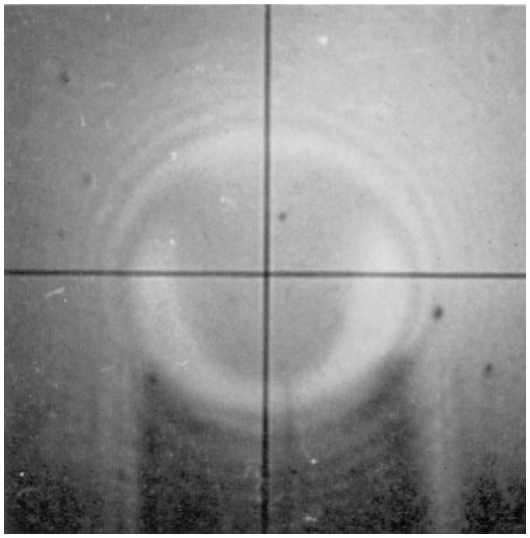

***Figure 3-6:*** ***Example of lubricated point contact showing the exit constriction (from Cameron and Gohar [21])***

This reduction in film thickness can be explained by the very sudden loss of viscosity of the lubricant when it goes from a high pressure region (the contact) to a low pressure one (the exit). In the inlet the pressure increases gradually because of converging region that enables the pressure to increase gradually, so no such effect is observed.

When the speed increases, more lubricant is provided to the contact and the film thickness increases accordingly (see Figure 3-7)

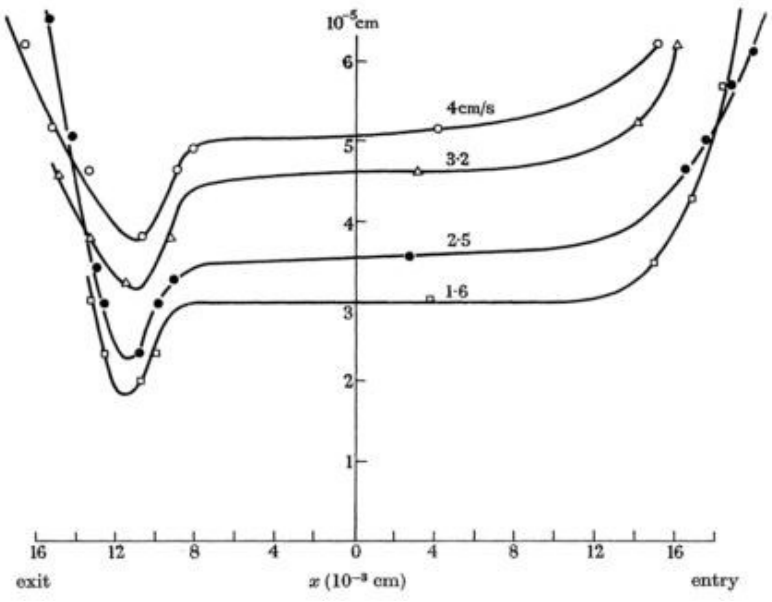


***Figure 3-7:*** ***Change in film thickness with speed for a smooth EHD point contact, the constriction is on the left of the image (from Cameron and Gohar [21])***

#### 3.1.2.2. Fabrication of Textures

All early research studied smooth surfaces and focussed on the overall shape of the EHD contact and the dependence of film thickness on speed, load and elastic modulus (see Cameron and Gohar [21] and Foord et al. [24]). However once these were reasonably well understood, interest turned to the behaviour of rough surfaces in EHD contacts. Most researchers have studied model surface roughness rather than real roughness. This is due both to the difficulty of studying real roughness and the fact that it is easier to decouple phenomena and find general rules using simple geometries with well-defined roughness features. The various textures studied can be divided into different categories according to their geometry or fabrication process.

The first reported studies on artificial roughness used mechanical processes to modify otherwise smooth contacting surfaces. Jackson and Cameron [43] used a lathe to generate cuts on a steel ball. They produced transverse and longitudinal unidimensional roughness. However, due to the manual nature of the manufacturing process the geometry of the roughness obtained was irregular, not having a well defined depth or wavelength. Wedeven and Cusano [44] produced roughness features by indenting surfaces with tools of varying shapes in order to obtain dents or grooves with less random geometries than scratches. By employing the same process several times, it was possible to model more complex asperities (Cusano and Wedeven [45]). More recently, the same principle has been used by Krupka and Hartl [46] to obtain arrays of dents on a steel ball.

A lot of work regarding textured surfaces has been done in the field of hydrodynamic bearings. Following the same idea of creating textures through a mechanical process,

Pettersson and Jacobson [47] developed embossing tools to produce textures on such bearings. Laser surface texturing (LST) is also very common and is even used in industrial applications. Various authors (Kligerman et al. [6], Etsion [48], Koszela et al. [49]) have studied how this technique can be used to improve the tribological properties of hydrodynamic bearings. The application of this technique to concentrated non-conformal contacts has not really been investigated, although Mourier, Mazuyer, Lubrecht, and Donnet [50] have studied the effect of a cavity produced with a femtosecond laser

The techniques described above are based on the modification of the existing surfaces; hence the surface features are made of the same material as the specimen itself and usually consist of depressions in the surface. Another approach to produce artificial roughness consists in adding some material on an existing smooth surface. For example, several authors have produced textures by sputtering chromium on smooth surfaces (Kaneta and Cameron [51], Guangteng et al. [35], Choo [52]). This has led to very interesting laboratory results as it enables the fabrication of well defined ridges or bumps; however it has limited practical application due to the fragility of the roughness features that usually rub off quite easily in sliding conditions.

#### 3.1.2.3. Influence of the Roughness Geometry in EHD Film Thickness

Jackson and Cameron [43] studied the influence of grooves on a roughened steel ball. They produced a lubricated contact between the ball and a glass disk, with the ball remaining static to give a pure sliding contact. By rotating the ball through 90° it was possible to study both the parallel (along the sliding direction) and the transverse (at 90° to the sliding direction cases. In both cases they observed a reduction of the minimum film thickness compared to

the smooth case. The mean film thickness was the same as with smooth surfaces in the transverse case but reduced in the parallel case. They also found that the transverse roughness gave a higher minimum film thickness than the parallel case, which was also found in later studies.

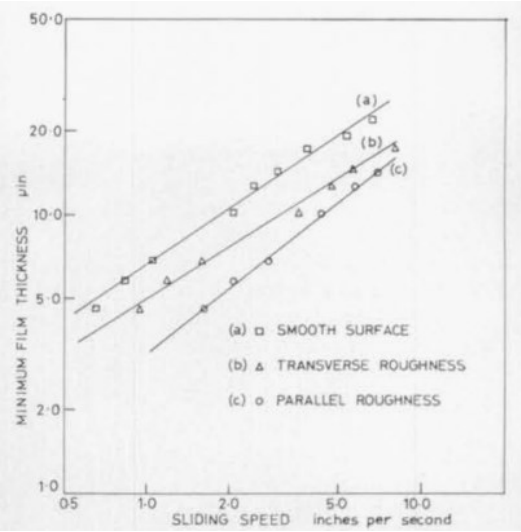


***Figure 3-8:** Variation of the film thickness depending on the orientation of the roughness (from Jackson and Cameron [43])*

Wedeven and Cusano [44] studied well-defined textures produced with a wedge-shaped tool to form furrows parallel and transverse to the rolling direction. They examined both rolling and rolling-sliding conditions. They noted that the lubricant tended to accumulate in the valley and, in the case of transverse grooves, when sliding was added the oil flowed out of the groove and generated a “tail”. In pure rolling, they measured thinner film compared to the smooth case for both orientations.

For transverse roughness they observed a perturbation in the film thickness formed as a ridge passed through the inlet. This travelled across the contact at the entrainment speed. This is consistent with results of later studies on transverse roughness (Kaneta, Nishikawa, et al. [36], Guangteng et al. [35], Choo, Olver, and Spikes [53]). It represents an important feature of individual roughness features that pass through the contact, that they give rise to two

different processes. One is that, unless fully flattened, the roughness feature itself passes through the contact at the speed of the surface to which it is attached. The second is that the roughness feature creates a perturbation of film thickness as it passes through the contact inlet due to it changing the mean radius of curvature in the inlet. This perturbation (a region of increasing and the decreasing film thickness) then passes through the contact at the mean speed of the two surfaces. It can thus stay with, move ahead of or fall behind the roughness feature, depending on whether the surfaces have the same speed or which moves faster. Another feature that was observed in all these studies is that as the transverse asperities travel through the contact, the lubricant entrapped between each valley starts to leak towards the side of the contact. Choo, Olver, and Spikes [53] successfully modelled the thickness of the micro-EHD films by using film thickness regression equations (Hamrock and Dowson [54]) on the tips of the asperities.

Parallel (or longitudinal) ridges have been studied less often than transverse case ones (Kaneta, Sakai, et al. [27], Choo, Olver, Spikes, et al. [55], Krupka, Sperka, et al. [56]). Contrary to the transverse ridges or furrows, no perturbation was observed and the measured film thicknesses were substantially reduced compared to transverse roughness. This is understandable as longitudinal asperities are invariant in the rolling-sliding direction through the contact, meaning that no transient effect is to be expected in the inlet. No side leakage has been reported, suggesting that longitudinal asperities facilitate the flow in the rolling-sliding direction but prevent it in the transverse direction.

A number of studies have investigated the influence on the film thickness of single features such as dents (Wedeven and Cusano [44], Krupka and Hartl [46]), bumps (Choo et al. [57], Kaneta and Cameron [51]) or laser textured cavities (Mourier et al. [50]). In the case of bumps

Choo, Glovnea, et al. [57] observed micro-EHD behaviour, with micro horse-shoe shapes (see Figure 3-9) at the peak of the asperities in pure rolling. When sliding was added a perturbation was convected away before the film recovered the micro horse-shoe shape. It was shown that the film thickness at the bumps was predictable by using regression equations (Hamrock and Dowson [54]) considering their radius of curvature as parameter in regression film thickness equations. An interesting observation was made that when the disk was moving slower than the ball (on which the asperities were deposited), the micro-horse shoe shape was oriented in the opposite direction than the macro horse-shoe shape; this is probably due to the orientation of the relative flow.

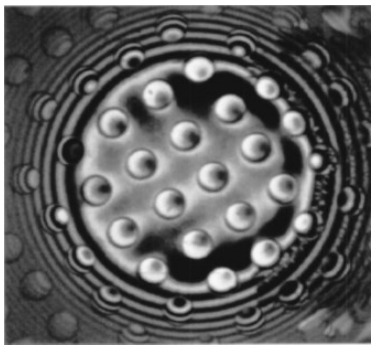

***Figure 3-9:** View of micro-EHD phenomenon at the top of circular bumps (from Choo, Glovnea, et al. [57])*

Several authors have showed that dents can have a positive impact on the overall film thickness. Depending on their depth, the array of dents tested by Krupka and Hartl [46] generated perturbations downstream of the leading edge of each micro-dent similar to what is observed with transverse ridges. These perturbations were shown to increase the local film thickness. This beneficial effect was observed only at a certain value of the dent depth and seemed to increase with the slide roll ratio.

Mourier, Mazuyer, Lubrecht, and Donnet [50] studied a circular cavity (see Figure 3-10) produced using a femtosecond laser.

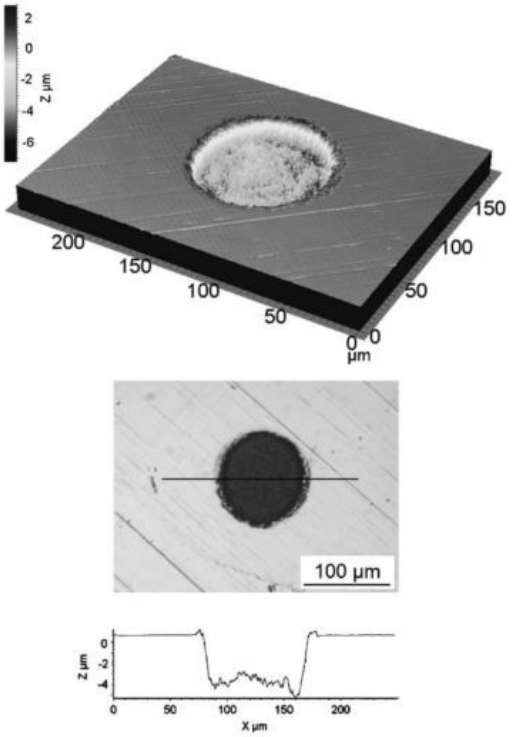


***Figure 3-10:** Micro cavity generated with a laser pulse (from Mourier et al. [50])*

The film thickness was measured on ball-on-disk apparatus. One advantage of their fabrication technique is that it enables a very accurate definition of texture geometry. As shown in Mourier et al. [52], the depth of the cavity can be controlled by the pulse energy and the number of laser pulses. In their study they investigated rolling-sliding conditions (SRR=-0.5) of a single cavity passing through an EHD contact for two depths, 400 nm and 700 nm. They showed that the deepest cavity made the film collapse while the shallowest created a transient increase of the lubricant film. In parallel they ran a numerical simulation which enabled them to give a physical interpretation of the perturbation phenomenon. The numerical results showed an increase of pressure at the leading edge of the cavity. Their explanation is then:

- A slight decrease of the local film thickness is observed as the cavity enters the contact, because the oil is pushed inside the cavity.
- The high pressure in the cavity increases the viscosity by 3 orders of magnitude.

- The “solidified” oil is extracted from the cavity by the shear stress.
- Leaving the cavity, the oil locally deforms the surfaces elastically.
- After the oil has left the cavity, they observed a reduction of the pressure in the pit.
- The oil perturbation continues is now entrained by the lubricant flow so it travels faster than the cavity itself (the ball is moving slower than the disk).

As shown on Figure 3-11 they calculated that the pressure peak increases with the depth of the cavity. At the same time they also calculated that the pressure in the cavity decreased after the extraction of the oil.

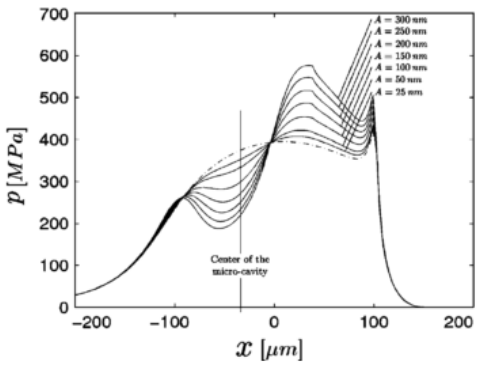


***Figure 3-11:** Influence of the cavities geometry on the pressure in an EHD contact (from Mourier et al. [50])*

When the depth of the cavity was increased, the pressure decreased to a certain point where the piezo-viscous effect was no longer preponderant and the flow was dominated by pressure (Poiseuille flow), hence the lubricant was driven back into the cavity. This interpretation seems to be consistent with what has been described in other papers regarding dents (Krupka and Hartl [46]).

## 3.2. Friction

Knowing the shear stresses and thus the friction in EHD contacts is of great importance as it determines the power loss. Most studies do not look directly at the shear stress which is difficult to measure but at the friction, *i.e.* the force generated by the integrated shear stress over the entire contact area. Very often the friction is normalized by the normal load to give the friction coefficient.

### *3.2.1. Measurement Techniques*

The friction can be measured experimentally either by direct measurement of the friction through load cells (all the studies using the PCS MTM *e.g.* Lafountain et al. [59], De Vicente et al. [60]) or by indirect techniques such as the measurement of the power loss or infrared temperature mapping (Reddyhoff, Spikes et al. [61]). The latter consists in establishing a temperature map inside the contact to deduce the frictional dissipation and the corresponding friction force. This assumes the Peclet number is low so that the heat convection in the fluid is negligible. One advantage of this technique over the measurement of the friction force is that it gives a distribution of the traction over the contact and not an average value, which is of great interest in the study of rough surfaces (see Yagi et al. [62])). It also provides validation for phenomena such as compression heating (see Reddyhoff, Spikes et al. [63]).

### *3.2.2. EHD Friction*

Stribeck carried-out the first systematic study of the evolution of the friction coefficient with speed in a journal bearing. In recognition of his work this representation is now known as the Stribeck curve. Nowadays for journal bearings the speed is usually replaced by the Sommerfeld number which includes the speed, the viscosity and the load applied but for EHD

contact friction is still normally shown as friction coefficient versus speed or the produce of (speed*viscosity).

Stribeck curves are very useful to understand and identify the different lubrication regimes as they show the transition between them very clearly.

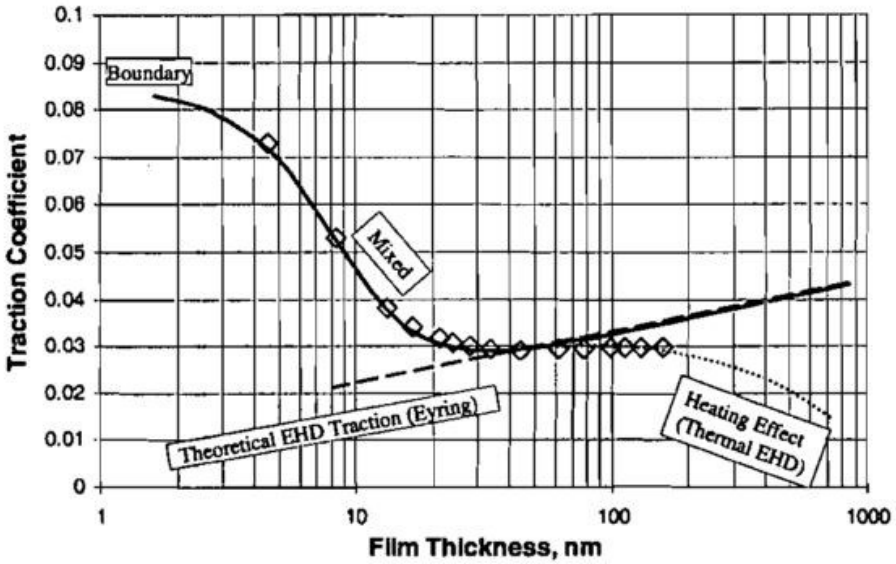


***Figure 3-12:** Example of Stribeck curve (from Lafountain et al. [59])*

An example of Stribeck curve is shown on Figure 3-12. To explain its shape a simple assumption can be made that the friction is split between a boundary part coming from direct solid-to-solid contact and a fluid part coming from the resistance of the lubricant film to shearing. The boundary friction is typically modelled as proportional to the load borne by the asperities while the fluid friction depends on various parameters such as the sliding speed or the viscosity. In the boundary regime the solid-to-solid contact is predominant so that the friction is equal to the boundary friction. When the film starts building-up, the mixed-lubrication regime is entered. The portion of the load that is borne by the lubricant becomes significant and since the boundary friction is almost always higher than the fluid friction, at this speed the friction decreases. At some point the lubricant separates the surfaces

completely; this is when the full EHD regime is reached. In principle as soon as the surfaces are separated the friction should start rising. However, two effects will generally affect the transition speed. One is a reduction of the viscosity due to shear thinning of the fluid at high shear rates. The other comes from the fact that in the conditions traditionally observed in EHD contact (high shear rate and shear stress), the lubricant often heats up which will decrease its viscosity and the friction generated. As shown in Spikes and Jie [64], researchers still disagree on the respective importance of these two phenomenon.

### *3.2.3. Influence of the Roughness*

Relatively few studies have investigated systematically the influence of surface roughness on the friction in EHD contacts and, surprisingly, these almost never correlate the friction measurements to actual film thickness distribution measurements.

Some authors have studied random roughness and have investigated the influence of the lambda ratio. Bair and Winer [65] measured the traction of a set of lubricant at one SRR in a contact between a rough steel ball and a sapphire disk and they used Hamrock and Dowson's equations to calculate the film thickness. By varying the fluid and test temperature they were able to achieve a relatively large range of lambda ratios which enabled them to identify three regimes of lubrication:

- For **$\lambda > 20$**, the load is born by a much larger area than the Hertzian area, this leads to a reduction of pressure, hence the viscosity moves back toward the viscous regime and the traction decreases
- For **$1\text{-}1.5 > \lambda > 15\text{-}20$**, the traction is determined by a limiting shear stress
- For **$\lambda < 1$**, the contact enters the mixed regime where the asperities increasingly bear some load

Evans and Johnson [66] used smooth film thickness measurement to calculate the lambda ratio and carry-out similar analysis. They obtained somewhat similar results with slightly different boundaries:

- For **$\lambda > 5$**, the influence of roughness on the traction is negligible
- For **$\lambda < 1.5$**, the traction is determined by the high pressures at individual asperities where a micro-EHD film forms. They suggest using an elastic-plastic rheological model to calculate the friction.
- For **$1.5 > \lambda > 5$**, if the nominal pressure is high an elastic-plastic model can also be used to model the friction but if the pressure are lower some asperities might not reach the elastic-plastic regime. In this case, to be able to estimate the friction, the actual pressure distribution has to be known.

Nanbu, Chiba, et al. [67] studied random and directional roughness and they observed an increase of the friction that they correlated to some roughness parameters. Interestingly, they try to estimate the average film thickness with a capacitance method. With these results they concluded that the increase of shear stress in the rough cases should be attributed to an increase in viscosity due to high pressures rather than an increase in shear rate.

All these previous studies support the hypothesis of Jefferis and Johnson [68], that in the rough case friction is dominated by the operating conditions at the top of asperities, where a micro-EHD film forms and the pressure is localized. The combination of high pressures and thinner film will have the effect of increasing both the viscosity and the shear-rate and so the friction.

Concerning the comparative effect of parameters other than the RMS roughness, Nanbu, Yasuda, et al. [69] studied the influence of grooves with various orientations in order to optimise a CVT (continuously variable transmission). They observed that among the different textures tested (super-finish, transverse and longitudinal grooves), the most efficient for their application was parallel grooves oriented in the rolling/sliding direction. These results can be compared with experimental studies of film thickness previously cited (Jackson and Cameron [43], Choo, Olver, Spikes, et al. [55]) that showed a clear reduction of the lubricant film thickness at the asperities with longitudinal roughness compared to other textures.

Britton et al. [70] studied the effect of the roughness on the friction in a gear pair. They compared the friction in a normal gear where the roughness is oriented transverse to the rolling-sliding direction and compared it to a gear where the surface had been super-finished. They reported a reduction of friction of 20% in the smooth case compared to the rough one. This suggests that in any case the roughness has a detrimental effect on the friction.

## 3.3. Pressure

### *3.3.1. Measurement Techniques*

Measurement of pressure in an EHD contact has proved to be much more difficult than measuring the friction or the film thickness. Several techniques have been developed but none has really emerged as suitable for routine use. An early attempt applied to dry line contacts (Klemz [71]) was based on photoelasticity but this approach has never been used since. Direct measurements of the pressure can be achieved by Raman spectroscopy (Jubault et al. [72], Himmel et al. [73] ) or by using thin film sensors (Höhn et al. [74]), however these techniques have poor spatial resolution. A novel technique was used by Cann and Spikes [75]) who used a sapphire disks with a silica layer sandwiched between two reflective chromium

layers as can be seen in Figure 3-13. When light is shone into the contact, interference fringes can be observed. If the lower chromium layer is loaded, the spacer layer is compressed which can be measured on the interferogram. By using an appropriate calibration, the pressure can be deduced from this deformation.

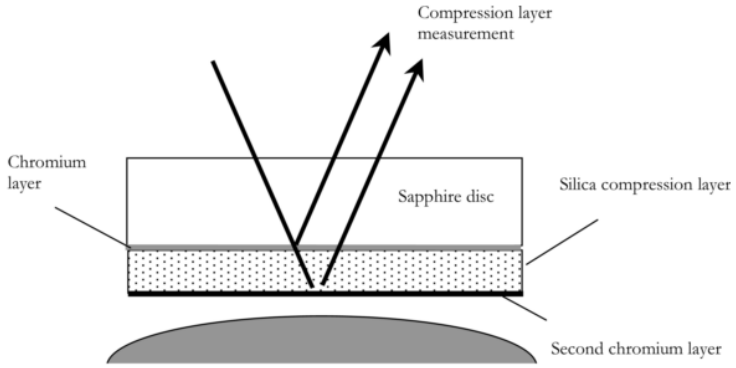


***Figure 3-13:** Special disk for pressure measurements (from Cann and Spikes [75])*

Another approach proposed by several authors (Kannel et al. [76], Safa et al. [77]) consists in sputtering micro-scale pressure-sensitive transducers (manganin coating) and measuring the variation in resistance. As shown by Safa et al. [77], this technique can even resolve the pressure spike.

In other studies semi-experimental techniques or "inverse method" are used. The film thickness is first measured on a real contact using optical interferometry. From this the displacement field can be estimated and using a model the pressure field can be estimated (Molimard et al. [78]). This approach will be further described in the next chapter.

### *3.3.2. Findings*

The difficulty of measuring the pressure experimentally means that theoretical predictions (see Dowson et al. [79]) took some time before being confirmed. According to these, to a first approximation the pressure in a smooth EHD contact can be estimated by the Hertz pressure distribution. This is particularly valid at low speeds and high applied loads, but as the speed

increases the pressure builds up in the inlet region and decreases to the rear of the horse-shoe region of the contact. As shown on Figure 3-14 an interesting feature is that at the exit and sides of the contact, a pressure spike can be observed. When measured in parallel with the film thickness it appears that this peak coincides with the beginning of the constriction.

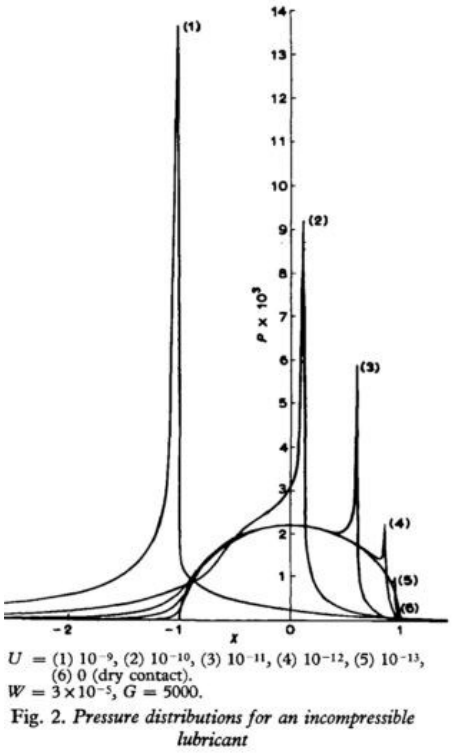


$U$ = (1) $10^{-9}$, (2) $10^{-10}$, (3) $10^{-11}$, (4) $10^{-12}$, (5) $10^{-13}$, (6) 0 (dry contact).
$W = 3 \times 10^{-5}$, $G = 5000$.

Fig. 2. *Pressure distributions for an incompressible lubricant*

***Figure 3-14:*** ***Various pressure profiles in EHD conditions (from Dowson et al. [79])***

Various studies have confirmed these features experimentally using methods described in the previous section (with Raman spectroscopy, Jubault et al. [72], transducers, Safa et al. [77]).

In the rough surface case, experimental studies are still scarce. Using an inverse method, Olver et al. [80] looked at the effect of a sputtered transverse ridge on the pressure. They observed that in static condition the asperity conformed closely the opposite surface which led to a maximal overpressure at the asperity. As the film developed they observed the recovery of the asperity which was linked to a reduction of this overpressure. They interpret this result as an effect of “cushioning” from the asperity.

Recently, Krupka, Vrbka, et al. [81] investigated the effect of dents produced on the pressure by an inverse method. The dents were produced with a Rockwell hardness cone and a lip was observed to form at the edges of the dent, which had to be polished off. In general they observed that in sliding contact, the pressure was increased where the film perturbation propagated (at either the trailing or the leading edge depending on the direction of sliding) and was reduced in the dent. In the case with the deepest dents, the pressure in the dent was found to collapse completely. However this is probably due to the fact that the authors had to fit the undeformed shape because they were not able to measure the very thick films present.

## 3.4. Conclusion of the Chapter

In this Chapter the regime of lubrication known as Elastohydrodynamic lubrication was described. The complexity of the EHD regime arises from the very harsh operating conditions observed in the contact which affect the lubricant film thickness, the friction and the pressure distribution. The historical development of various experimental techniques used to measure these physical quantities in the context of Tribology is explained. In particular the importance of the techniques based on Optical Interferometry to measure lubricant film thickness is thoroughly investigated in relation with other techniques. This enables to justify why these techniques were used in the current experimental work.

Fundamental results on film thickness, friction and pressure in the case of smooth EHD contacts are listed. A few results on rough contact are also presented for different geometries of roughness. Main findings include the observation of the micro-EHD phenomenon, *i.e.* the development of a pressurized film at the top of roughness asperities, the increase of friction

in the rough case compared to the smooth case equivalent and the observation of high pressure ripples when asperities cross the contact area.

The lack of knowledge and the absence of a general theory of rough EHD contact suggest that further experimental work remains to be carried out.

# Chapter 4 - Review of Theoretical Studies

This chapter reviews the main theoretical studies on EHD contacts. The increase in computer power and the development of techniques with high resolution have made numerical modelling a very important tool in the study of EHD contacts. Simulation is used in two ways. Firstly, it can be used in conjunction with experiments to help interpret observations. However, most of the time numerical modelling is used in isolation as it enables the easy study of situations that are difficult to reproduce experimentally. Thus a plethora of authors have studied the behaviour of roughness in EHD, but many of their findings are yet to be confirmed by experimentation. This concerns, for example, the compression of asperities in the contact area as well as physical parameters that are very difficult to measure experimentally, such as the pressure or the temperature.

Numerical solution of the EHD problem requires the simultaneous solution of three equations; (i) one relating fluid film pressure to elastic deformation and thus the geometry of the contact (contact mechanics); (ii) one relating film geometry, applied load and speed and lubricant viscosity to film pressure (flow equation) and (iii) one relating lubricant viscosity to pressure (fluid rheology). Each of these is described below. A fourth equation relating lubricant density to pressure is also required for very high pressure contacts but it not required in the current study.

## 4.1. Solving EHD Contacts

### *4.1.1. Contact Mechanics*

In EHD conditions the pressure in the contact is high enough to significantly deform the surfaces. The Boussinesq relationship links the deformation in a half space to a normal point force (see equation (1)). However, integrating the problem over the entire contact area is impossible in most cases. Therefore, authors usually discretize the domain of interest, for example in rectangular patches. Love [82] calculated the deformation in a half-space caused by a uniform pressure distribution over a rectangular area. Figure 4-1 show the effect of a single element of uniform pressure on a half space. The representation is in 2D but the behaviour is cylindrically symmetric.

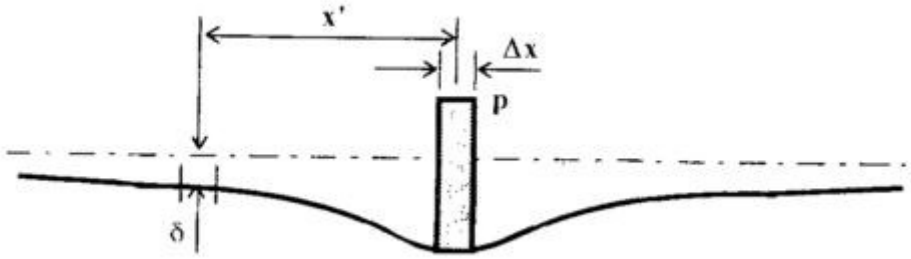


***Figure 4-1:** Deformation due to a single uniform pressure element (from Sayles [83])*

For any given point an influence coefficient $\boldsymbol{C = \frac{\delta}{p}}$ can be calculated. This links the displacement at the point and the pressure applied on a rectangular area and depends on the material properties and the distance between the point where the displacement is calculated and the central point of application of the pressure. The formula to calculate this coefficient can be found in Johnson [2]. A set of influence coefficients can be calculated for every point in the area of study, so that a matrix of influence coefficients can be obtained. This gives the relationship between an element of pressure and the displacement at a point located at any possible distance from it in the studied problem. If a distribution of pressure is considered, it

can be shown that the total displacement is simply the sum of the displacements due to every individual pressure element. Hence if ***W*** is the displacement field, ***P*** the pressure distribution and ***K*** the influence coefficient matrix, the relationship becomes:

$$W = conv(K, P) \tag{22}$$

where *conv* is the convolution operation. Iterative methods are usually used to solve a contact mechanics problem, so that equation (22) may have to be solved many times which can be computationally expensive, especially if the surfaces are rough. For example an incremental vertical displacement can be given until contact occurs then the pressure is found by using equation (22) (see Cole and Sayles [84]). The process is repeated until a predefined condition are satisfied, such as a given load or displacement. A direction calculation is not very fast ($O(n^2)$) so various alternative strategies have been implemented in order to reduce the calculation time. One method is based on the property of Fourier transforms that turns a convolution in the time domain into a simple multiplication in the frequency domain (Ju and Farris [85], Nogi and Kato [86], Kadiric et al. [87]).

$$\widehat{W} = IFFT\left(\widehat{K}.\widehat{P}\right) \tag{23}$$

where the accent designates the Fourier transform of the fields and ***IFFT*** is the inverse of the Fast Fourier transform. However this technique tacitly supposes that the problem is periodic, so that the pressure calculated is not due to one single contact but to an infinite number of contacts periodically spaced. This was discussed by the original authors (Ju and Farris [85]) who found that by extending the domain of calculation to five times the width of the region of interest, the error in this region was minimal.

Another very common method is the Multi Level Multi-Integration technique (MLMI) that consists in successively solving the problem on various grid sizes in order to accelerate the convergence (see Lubrecht and Ioannides [88]).

The benefits of both techniques were discussed in Polonsky and Keer [89]. For a given grid size, the MLMI technique requires more operations ($O(N\ log(N)^2)$) than the FFT-based one ($O(N\ log(N))$) but since the FFT-based technique needs an extended domain to be accurate, the authors argue that the MLMI technique is more efficient. However considering the computational power of modern desktops and also the easy implementation of FFT calculations in softwares such as Matlab, the use of FFT-based technique is arguably more practicable.

Even though the deformation of the contacting surfaces is usually considered as elastic, some authors have considered elasto-plastic models, which enables to study the effect of debris for example (Kang et al. [90]).

### *4.1.2. Equation of Flow*

The flow in a lubricated contact can be described by the Navier-Stokes equations but these are difficult to solve. Hence, most authors preferred to use the Reynolds equation (Reynolds [91]) that is a simplification of Navier-Stokes. The Reynolds equation links the pressure in the lubricant and the film thickness with the speeds and geometry of the contacting surfaces.

Even though the Reynolds equation is a simplification, for a long time it was still be computationally-expensive to solve, especially in EHD problems where the deformation has to be calculated at the same time. This led authors (Lubrecht et al. [92], Lubrecht et al. [93]) to use MLMI techniques to solve the Reynolds equations.

Nowadays, with the increase in computer power, the direct resolution of Navier-Stokes equation have become more attractive (Almqvist and Larsson [94]). This is a very powerful tool as it enables the very accurate modelling of all the field gradients and thermal phenomenon (Hartinger et al. [95]).

### *4.1.3. Fluid Rheology*

Two aspects of fluid rheology have to be considered in solving the EHD problem, pressure-viscosity and shear thinning.

In EHD contacts an appropriate model of the lubricant's pressure-viscosity behaviour is essential and one commonly-used relationship is the *Barus equation* (equation (8)). The increase in viscosity with pressure plays a critical role in the contact inlet where it results in a significant increase in viscosity and thus enhanced lubricant entrainment. It is also important in the central region of the contact since, when sliding is present it produces a very large increase in shear stress and thus results in shear thinning.

The lubricant shear thinning is particularly important when modelling is used to calculate EHD friction.

Several models have been proposed to describe this shear thinning. In particular, Hirst and Moore [96] and Johnson and Tevaarwerk [97] developed a rheological equation based on the Eyring *sinh* law for shear-thinning. Later, some observations (Bair and W.O. Winer [98]) suggested that a certain critical limiting shear stress the lubricant starts behaving like a plastic solid so that the fluid cannot transmit more shear stress than this limit. This led to a refinement of the Eyring's model to take this into account (Evans and Johnson [99]). An

alternative to the Eyring's model, namely the Carreau-Yasuda model, is favoured by other authors (in particular Bair [100]).

## 4.2. Theoretical Solution of EHD Problems

### *4.2.1. Smooth Case*

The first theoretical solution to an EHD problem was produced in the early 1940s by Grubin [13]. He applied the Hertz theory to describe the surfaces deformation and the *Barus equation* (equation (8)) to model the rise in viscosity as the pressure increases. This way he provided a solution for the central film thickness of a smooth line contact. Grubin's solution was semi-analytical but all subsequent solutions have been based on computer-based numerical modelling which enable solution of both the central and minimum film thickness in smooth EHD contact, for both line and elliptical contacts (see Hamrock and Dowson [54] and Chittenden et al. [101]). Using this approach, these authors ran numerical solutions for various geometries and conditions in order to derive regression equations to fit the film thickness results. This enabled subsequent estimation of EHD film thickness without recourse to further numerical solution. These authors always express film thickness in terms of dimensionless parameters, a speed parameter $\overline{U}$, a material parameter $\overline{G}$ and a load parameter $\overline{W}$. Examples of regression equations are shown below:

- Dowson and Hamrock for the central film thickness in a circular contact:

$$\frac{h_c}{R} = 2.69\,\overline{U}^{0.67}\,\overline{G}^{0.53}\,\overline{W}^{-0.067}\,(1 - 0.61\,e^{-0.75}) \quad \textbf{(24)}$$

- Chittenden for the central film thickness in a circular contact:

$$\frac{h_c}{R} = 3.00\,\overline{U}^{0.68}\,\overline{G}^{0.49}\,\overline{W}^{-0.096}\,(1 - 0.61\,e^{-0.75}) \quad \textbf{(25)}$$

The form of these equations does not vary much; the only difference is coming from the coefficients. Also it can be seen the material and especially the speed parameters are preponderant, the load having almost no influence. These equations give good estimation of the film thickness; in particular the coefficient of the speed is always very close to 0.67 in experimentally measured film thickness curves.

These equations are still very used today as they provide a very convenient way to estimate the lubricant film thickness. It has also been shown that they can model the film thickness quite accurately even in more complex cases, such as textured surfaces (Guangteng et al. [35], Choo, Olver, and Spikes [53], Choo, Glovnea, et al. [57]).

Concerning friction, several predictive models have been proposed (see Olver and Spikes [102] and Jacod et al. [103]), leading to a better understanding of the characteristics parameters that influence the friction in the contact.

### *4.2.2. Rough Case*

The first question that arises when modelling rough surfaces is how to represent the roughness. Two families of approach have been implemented over the years. The oldest one, the stochastic approach, does not consider individual asperities or their geometry but considers a statistical distribution of height and wavelength. Greenwood and Williamson [104] developed a theory of dry rough contact between a smooth and a rough surface. They also show that the roughness of real engineering surfaces is very well modelled by Gaussian distributions. Greenwood and Tripp [105] later found that when two rough surfaces were considered, it was possible to find an equivalent model where only one surface is rough. Tzeng and Saibel [106] first introduced a solution of the Reynold's equation with rough surfaces in the hydrodynamic case by considering the film thickness as the sum of a nominally smooth

part and a rough part. Their solution was only for transverse roughness but was soon extended by Christensen [107] who proposed a solution with longitudinal roughness. He looked, in particular, at one-dimensional roughness (transverse and longitudinal). His work later influenced Johnson et al. [108], who applied his method in combination with the Grubin approach to calculate the film thickness in the case of longitudinal and transverse asperities. The equation they found suggested that longitudinal roughness reduces the film thickness while the transverse roughness increases it. Later Chow and Cheng [109] used the same approach to solve to study the effect of roughness at the inlet of an EHD contact and they found the same trend for transverse and longitudinal roughness as Johnson et al. [108]. Until then the study were limited to one-dimensional roughness, which can have interesting practical applications (see the roughness in gears or bearings), but are not entirely satisfying from a theoretical point of view. Patir and Cheng [110] introduced a method to solve the Reynold's equation for any random distribution of roughness. Their technique consists in defining an average Reynold's equation in terms of average pressure and some flow factors that depend on the roughness. They show that the flow factors are independent of the precise geometry of the roughness and depend only on the statistics of the roughness distribution. Hence, once the Reynold's equation has been solved for one particular distribution of asperities, the flow factors can be calculated and reused on any other statistically-identical distribution of roughness.

Over the last 20 years, with the rise in computer power and the development of numerical techniques such as the MLMI (Lubrecht et al. [111], Lubrecht and Venner [112]), it has become possible to solve Reynold's equation directly even in the case of complex surface geometry. Thus, nowadays most authors use a deterministic approach. In most cases the simulated

textures are analogues of those mentioned in the experimental section (bumps, cavities, ridges). These simulations are used either to validate a theoretical model or to support the physical interpretation of experimental results.

One of the main interests of numerical simulation is to study physical phenomena that are difficult to measure experimentally such as the pressure distribution or the temperature.

For example, the deformation of the surface roughness as it goes through the contact has been extensively studied in point and line contacts for harmonic roughness (see Lubrecht and Venner [112], Hooke and Venner [113] and Wang et al. [114]). The main achievement of this series of studies was to determine a master curve function describing the reduction in height of the asperities in terms of a single parameter which depends on the wavelength and the operating conditions.

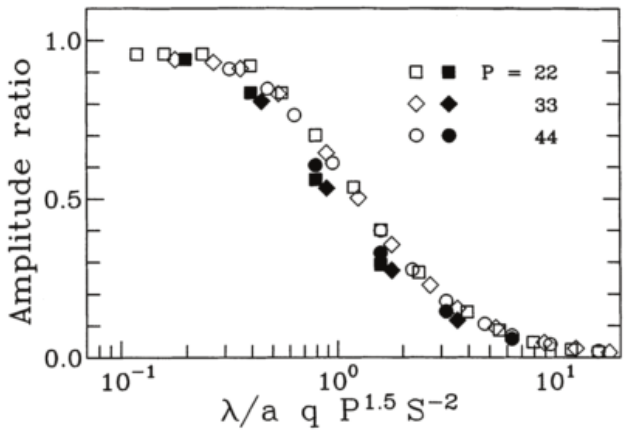


***Figure 4-2:** Amplitude reduction in point contact (white) and line contact (black) at different operating conditions (from Hooke and Venner [113])*

Concerning friction, Jacod et al. [115] have created a numerical model to investigate the influence of longitudinal roughness on the friction in an EHD contact. In the paper they first

studied a single sinusoid and calculated the relative friction variation for a range of roughness geometry parameter and lubricant properties. The results were fitted to a formula depending on those parameters. Then they ran a second set of calculations for a profile with two sinusoids. They found out that the previous formula was still valid if they considered as input an equivalent wave whose amplitude and wavelength is related to those of the two waves. In the last section of their article, they considered real longitudinal roughness (see Figure 4-3). Using Fourier transforms, they decomposed the surfaces geometries into sums of harmonic functions and, using the equivalence valid for a sum of two waves, they calculated the change in friction due to the roughness.

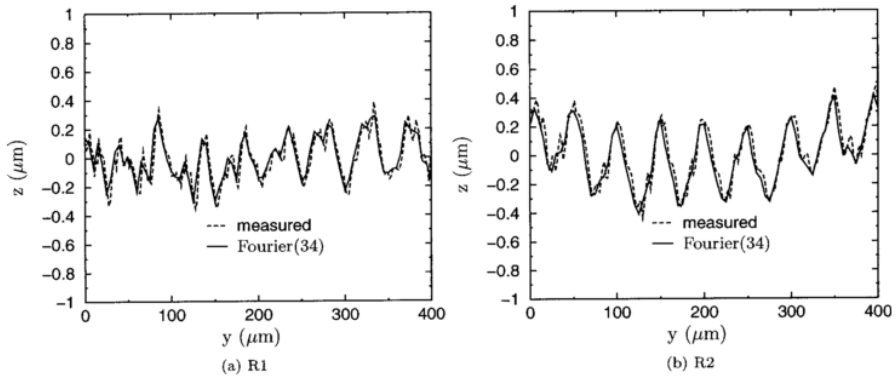


***Figure 4-3:** Two real roughness measurements and Fourier reconstruction (from Jacod et al. [115])*

## 4.3. Conclusion of the Chapter

This Chapter summarizes the theoretical studies of the EHD problem. The specificity of this problem lies in the fact that it requires solving both a fluid mechanics and a contact mechanics problem at the same time. In addition, the rheology of the lubricant and the variation of its property with pressure are also very important parameters that need to be taken into account given the very severe conditions typically observed in the EHD regime. The various numerical resolution techniques (MLMI, FFT) and models of flow behaviour (Reynolds, Navier-Stokes) are quickly described along with their respective advantage.

The main findings are then examined for both the smooth and the rough cases. In the smooth case, the practical importance of regression equations such as the Dowson and Hamrock equations is emphasized as they give a very quick and accurate estimation of the lubrication film thickness.

The different approach to modelling the roughness and solving the rough EHD problem are investigated. An important contribution of numerical modelling to research on the EHD problem is that it gives direct access to physical quantities that are often difficult to measure experimentally such as the pressure distribution or the deformation of asperities.

The current study aimed at developing experimental techniques that will help confirm or contradict some of the predictions made by these models and that are yet to be validated by experiments.

# Chapter 5 - Experimental Methods and Specimens

This chapter describes the equipment and the experimental method used in this study. The ball-on-disk rig on which the experiments were carried out is introduced along with other devices that were used to characterize some of the lubricants properties. The existing equipment was found to have several limitations; therefore the important developments that had to be made to the experimental set-up are explained. The specimen tested, the experimental protocol and the test condition are then described. Following that, a novel experimental procedure that enables the accurate measurements of film thickness in rough EHD contact is introduced. Finally, the inverse solution model used to obtain the pressure distribution is presented.

## 5.1. Experimental Test Rig

### *5.1.1. Ball-on-disk Set-up*

The main experimental apparatus used in the current research is a PCS Instruments EHD rig (see Figure 5-1).

***Figure 5-1:** Picture of PCS Instruments EHD rig (source: http://www.pcs-instruments.com/)*

As shown in Figure 5-2 a concentrated non-conformal contact is produced by loading a ball (19.05 mm diameter) against the flat surface of a disk. Various materials can be used for the contacting surfaces. If optical techniques are used the disk has to be made of a transparent material and in this project glass was used. In the case of optical interferometry the ball has to be sufficiently reflective, a metallic surface being ideal and in this study a steel ball was used.

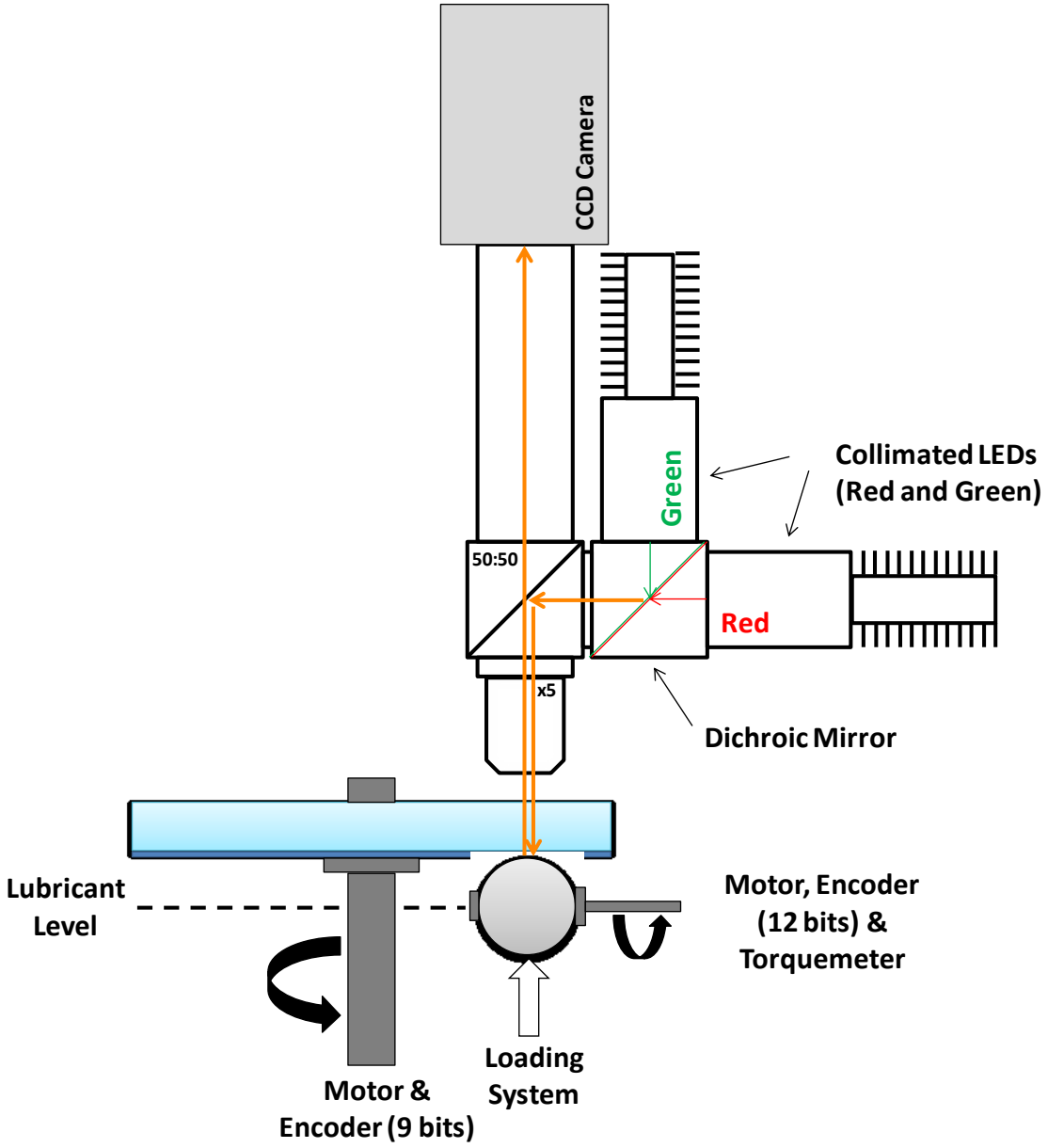


***Figure 5-2:*** *Schematic of the test rig*

Both ball and disk are attached to separate motors and their motions can thus be controlled independently so that it is possible to achieve pure rolling or rolling/sliding conditions with any slide-to-roll ratio between 200% and -200% and an entrainment speed spanning 0.005 mm/s to 4.8 m/s. The ball is located in a bath of lubricant whose temperature is monitored and controlled with a precision of +/- 0.5C between 20°C (room temperature) and 150°C. A load cell enables control of the load with an accuracy of ±1 N from 2 N to 50 N.

In standard tests a contact is produced between a smooth steel ball and a glass disk. A load of 20 N will generates a maximum Hertzian pressure of 0.530 GPa and a contact width of 269 μm.

### *5.1.2. Optical Techniques for Film Thickness Measurements*

The techniques employed to measure film thickness are based on optical interferometry. As explained in Spikes and Cann [116] the lower surface of the transparent glass disk is first coated with a 20 nm thick semi-reflective chromium layer that optimize the fringe visibility and on top of this a silica spacer layer to enables very thin film measurements. During the tests, light is shone at the contact and is split in two parts by the chromium layer. Half of the beam is reflected back from the chromium layer while the other half travels through the spacer layer and the lubricant film before being reflected back by the surface of the ball. The difference in path length between the two parts of the incoming beam produces a difference of phase between them. When they recombine interference fringes will be generated.

The two different techniques that have been used to analyse the interferograms in this study have already been described in Chapter 3. Ultra thin film interferometry was used to obtain very accurate measurements of the central film thickness *versus* speed with a very smooth specimen. This uses a spectrometer to obtain the spectral content of one line in the

interferogram; the film thickness can be calculated very reliably from this. An imaging technique based on SLIM was used to study rough surfaces and required the image to be captured by a CCD camera.

### 5.1.3. Friction Measurement

When sliding is applied to the contact a tangential force appears and generates a torque on the ball shaft. By measuring this torque with a torque meter attached to the ball shaft, the tangential force can be calculated as the lever arm is the radius of the ball (see Figure 5-3).

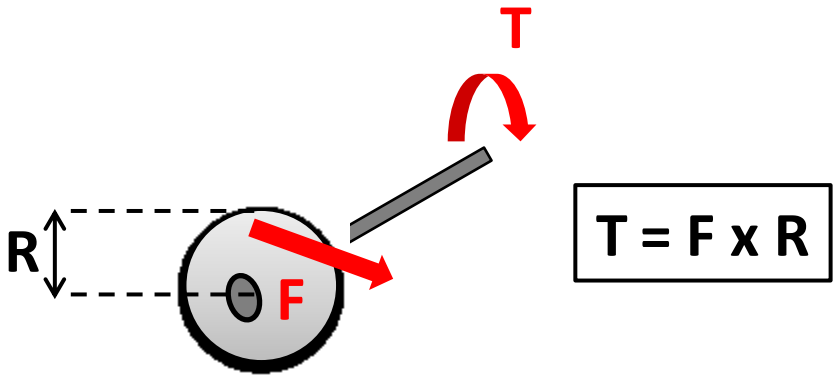


***Figure 5-3:** Schematic of the tangential force measurement*

The torque meter works by measuring the elastic deformation of strain gauges. Most commonly, a strain gauge is made of a thin metallic wire whose electrical resistance varies when it is deformed. As shown in Figure 5-4, to measure the variation of resistance the strain gauge is put in a Wheatstone bridge.

An excitation voltage (usually $V_{ex}$ = 5 or 10 V) is applied to the circuit and generates an output voltage $V_0$. When the strain gauge is deformed the variation of resistance will modify $V_0$ so that the variation $\Delta V_0$ is proportional to the elastic deformation and hence to the force applied. In practice the proportionality constant is found by applying a known torque and measure the variation in voltage.

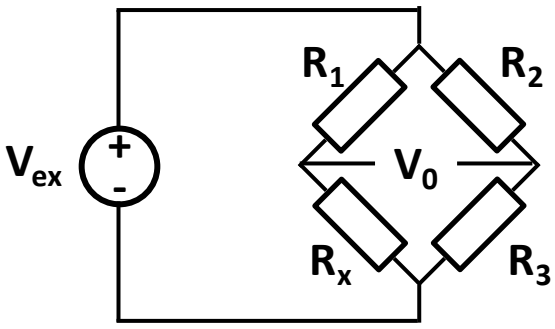


***Figure 5-4:** Schematic of a Wheatstone bridge explaining the principle of resistance variation measurement, $R_x$ represents the resistance of the strain gage*

## 5.2. Other Experimental Devices

### *5.2.1. Surface Characterization*

A white light interferometer (Wyko) was used to measure the roughness of the samples and the geometry of the surface textures. In this instrument a light beam is split internally, half is shone at the sample the other half at a reference mirror. When the beam is reflected by the sample, it recombines with the beam coming from the mirror and an interference image is produced. During a measurement, a nanopositioner translates the mirror, so that the optical path varies from a known amount. The interference fringes will vary accordingly and by measuring the phase shift between the different points of the image, the software is able to reconstruct the topography.

### *5.2.2. Lubricant Characterization*

In order to measure the film thickness using optical Interferometry the variation with temperature of the lubricant's refractive index is required. This was measured using a refractometer ABBE 60. This device comprises a sodium lamp that is shone through the oil sample and a prism of known refractive index. The refractive angle at the interface between the two gives the value of the refractive index of the oil.

The viscosity of the lubricant was measured with a Stabinger rotational viscometer: a cylinder is rotated at a known speed in the oil sample; then the dynamic viscosity is derived from the torque due to the sample's resistance. This instrument also measures the density of the fluid, and hence the kinematic viscosity.

## 5.3. Development of Experimental Method

### *5.3.1. Image Acquisition*

The standard interferometry technique implemented on the ball-on-disk rig is designed to measure EHD film thickness in smooth contacts. To be able to study roughened ball surfaces, several modifications had to be made to the standard set-up by the author of this thesis. These are described below.

#### 5.3.1.1. High Speed Camera

Normal colour cameras digitalize an image into three images. To do so the sensor is covered by a mask such as a Bayer filter that looks like a checkerboard with three different colours. Thanks to this filter, each pixel is sensitive to only part of the visible spectrum (red, green or blue). Figure 5-5 shows a Bayer filter, it comprises 25% of red, 25% of blue pixels and 50% of green pixels; hence the sensor will be more sensitive to green light.

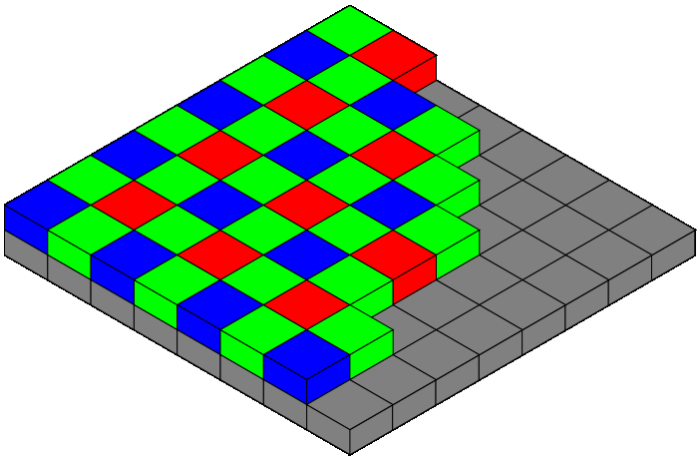

***Figure 5-5:** Example of Bayer filter used in a CCD camera*

It is evident that the three raw image data streams coming from this sensor are sparse as only one colour channel is really known for each pixel. A “demosaicing” algorithm has to be used to reconstruct the full colour image after it has been captured. This works by interpolating the unknown values from the sparse grid values. That often leads to image distortions such as aliasing if the resolution of the sensor is not high enough. The quality of the data is also affected as, in the best case, the colour resolution of the image is a third of the sensor’s resolution, the rest coming from interpolation. To avoid this, a 3CCD camera with three separate sensors can be used. Instead of using a filter mask to split the light, the light goes through a trichroic prism that splits it into its red, green and blue components. The three images are then captured by three separate CCDs.

In the smooth case, a long exposure time can be used without risk of blurring the image and corrupting the measurement as the film thickness is reasonably constant over time for any given point on the contact. When rough surfaces are considered, it is necessary to use a camera with a fast shutter speed in order to avoid excessive blurring as the roughness passes through the field of view.

The initial set-up used a JAI CV-M90 camera that has a maximum shutter speed of 100 µs which has previously been used to study roughness features in EHD contact up to ball speeds of about 0.2 m/s (see Choo [52]). However to study higher speed conditions it was necessary to be able to measure film thickness at higher speeds.

The Hitachi HV-F202GV camera used in this study is a 3 CCD camera with a maximum shutter speed of 10 µs. As the magnification of the lens was x5, each pixel covered an area of 1 µm x 1 µm on the ball. This set-up enabled the capture of sharp images up to a speed of 2.2 m/s. In practice it was found that above this speed the roughness became too blurred to be

analysed in detail. In this study, 800 x 800 pixel resolution interferograms were captured covering the entire contact zone and part of the surrounding region.

#### 5.3.1.2. Triggering

To monitor the lubricant film build-up at precisely the same location on the ball as the speed was increased, and thus study the same roughness features at different entrainment speeds, the camera was triggered off a fixed ball position for the duration of a test. To do this a 12 bit encoder was used (4096 positions). This encoder was attached to the ball shaft so that one encoder bit corresponded to a circumferential resolution around the ball of 15 μm for a ball of diameter 19.05 mm.

For accurate calculation of the lubricant film thickness the spacer layer thickness must be known. This is not perfectly constant around the disk and normally a trigger on the disc shaft is used to enable interference images to always be captured at the same disc circumferential position. However in this study the camera had to be triggered from the ball position rather than from the disk position. To avoid the spacer layer thickness varying from one image to another, the disk spacer layer thickness was mapped using a smooth ball and taking interference images all around the disk. As seen on Figure 5-6 the circumferential variation of the coating thickness is about ±1 nm.

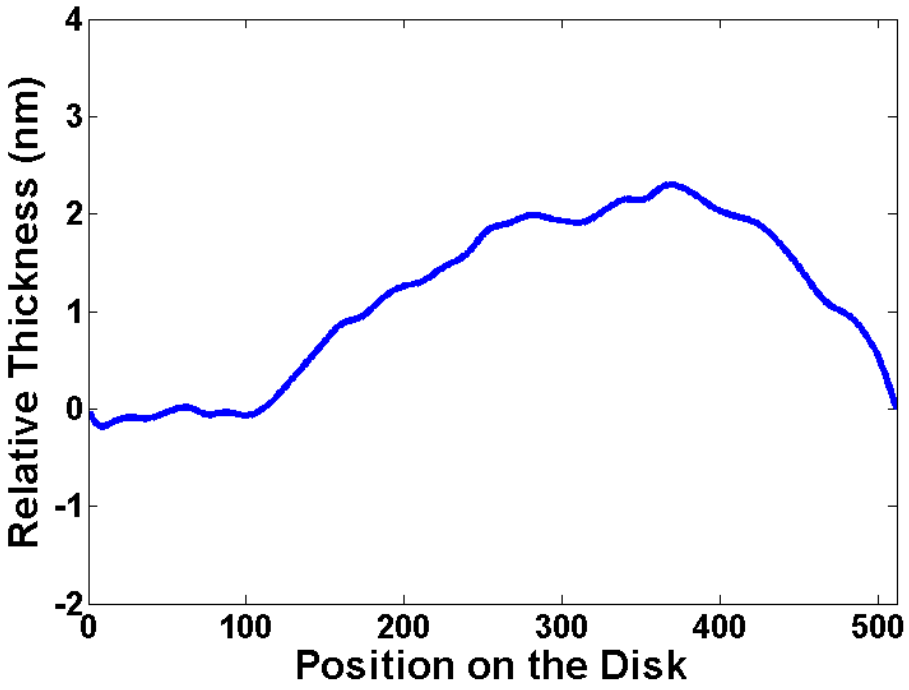


***Figure 5-6:** Example of spacer layer profile around the disk*

To eliminate the effect of this variation, a region of the disk where the variation in spacer layer thickness is minimal is chosen (such as between 0 and 100 on Figure 5-6). Then the triggering system was set so that the camera was triggered only when the selected roughness position on the ball was in contact with a portion of the disc lying in this specified range of disc track. This 'double triggering' also ensured that the image stayed focused since it minimised the effect of disk runout.

Implementing this triggering strategy required the outputs of both encoders to be known in real time so that the triggering signal could be generated at the right moment. This was implemented by using a Labview card NI PCI 7830R. A specificity of this card is that it has a user-programmable FPGA chip, which means that it acts like programmable hardware. This is very important in this application as the trigger signal needed to be generated instantaneously when the right positions of the ball and the disk were attained. Otherwise

the image would be captured in a different position of the ball. With a normal DAQ card, the triggering signal would be software generated and the reaction time greatly increased.

Another difficulty originated from the fact the encoders used were of two types. The disk encoder was a parallel encoder that has one wire for every bit of information plus a ground wire (see Figure 5-7a). Each bit was connected to a digital entry on the DAQ so that the disk position was known directly.

The ball encoder was a serial encoder which means that the bits of information are transmitted one at a time (see Figure 5-7b). This transmission is synchronised by a clock signal that was generated by the FPGA card.

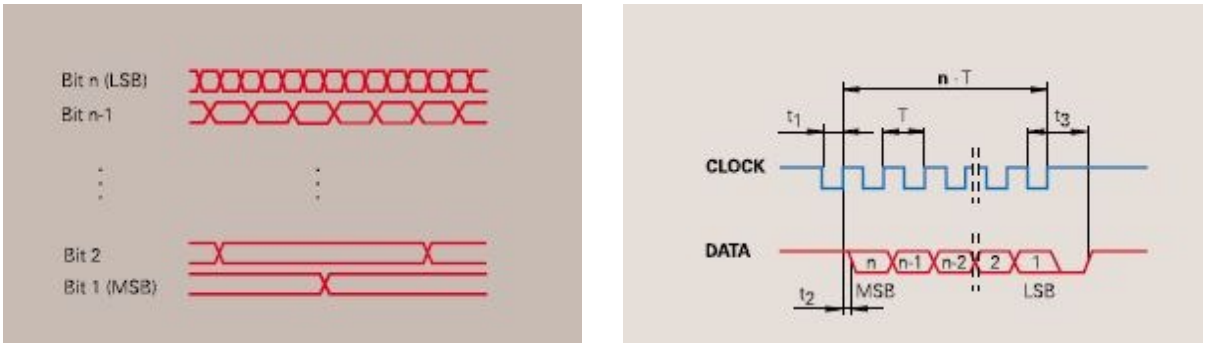


*(a)* *(b)*

***Figure 5-7:** Difference in the data transmission between (a) a parallel encoder and (b) a serial encoder, taken from Heidenhain rotary encoder catalogue*

This type of encoder has the advantage of needing only four wires (two for the data, two for the clock signal); however the transmission is not instantaneous as with a parallel encoder because the encoder requires the clock frequency to be below some upper limit in order to work. The card used in this work can generate pulses up to a frequency of 40 MHz which was much more than the maximum frequency taken by the encoder so that the maximum transmission rate was limited by the encoder. During this transmission time the ball continues

to rotate and at the highest speeds the shift in position had to be taken into account by changing the trigger position by a few positions.

To validate the triggering set-up, a smooth ball that had been laser textured with one 500 µm square was mounted on the EHD rig. The position of the square was chosen as the triggering position and images were taken over a large range of speeds. As seen on Figure 5-8 it is clear that the square, indicated by the dashed line, barely moves with respect to the triggering position and is not blurred, showing that both the triggering system and the fast image acquisition are working as expected.

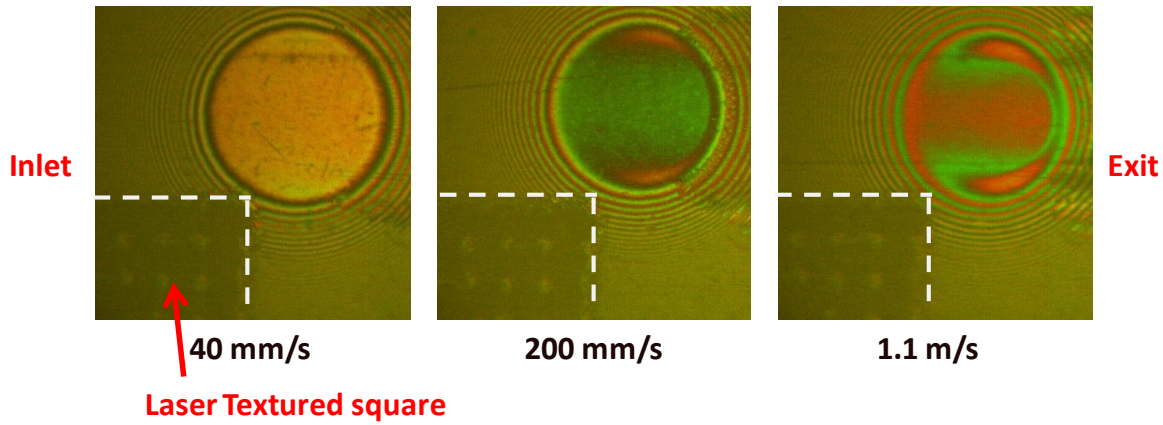


***Figure 5-8:** Images of a square textured surface passing through the field of view at different speeds*

A single Labview program was created in order to handle both the triggering signal generation and the image acquisition.

### *5.3.2. Optical System*

#### 5.3.2.1. Choice of the Light Source

Real light sources do not emit one single wavelength but a range of wavelengths. These sources lie between two extremes:

- narrow spectrum, with bandwidth of a few nanometres or less around a nominal wavelength: Lasers, some LEDs

- broadband, spanning the whole visible range of *ca* 300 nm: halogen, incandescent lamps

The bandwidth of the light source employed in an interferometry set-up will have important consequences on the corresponding fringes. In particular the broader the light source the lower will be the visibility of the fringes, *i.e.* the contrast of the fringes will vanish faster with increasing film thickness. The explanation for this is that the different wavelengths that are produced by the lamp will not interfere constructively or destructively at the same values of ***h***. To illustrate this, consider an "ideal" broadband with a spectrum defined as a Gaussian distribution around a nominal wavelength of 530 nm, with a standard deviation of 60 nm. To calculate the resulting intensity of the fringes, equation (14) was summed over all wavelengths of the visible range (from 400 nm to 700 nm).

$$I = \sum_{\lambda} S(\lambda).\left(1 + \cos\left(\frac{2\pi}{\lambda}.2nh\right)\right) \quad \textbf{(26)}$$

The refractive index was assumed to be ***n = 1.47*** and ***h*** to range from 0 to 1000 nm. ***S(λ)*** is the contribution of the wavelength ***λ*** to the light source. The same calculation is done for an ideal monochromatic light source with the same nominal wavelength. The results are shown on Figure 5-9 along with the light spectrum. The curves have been normalized between 0 and 1.

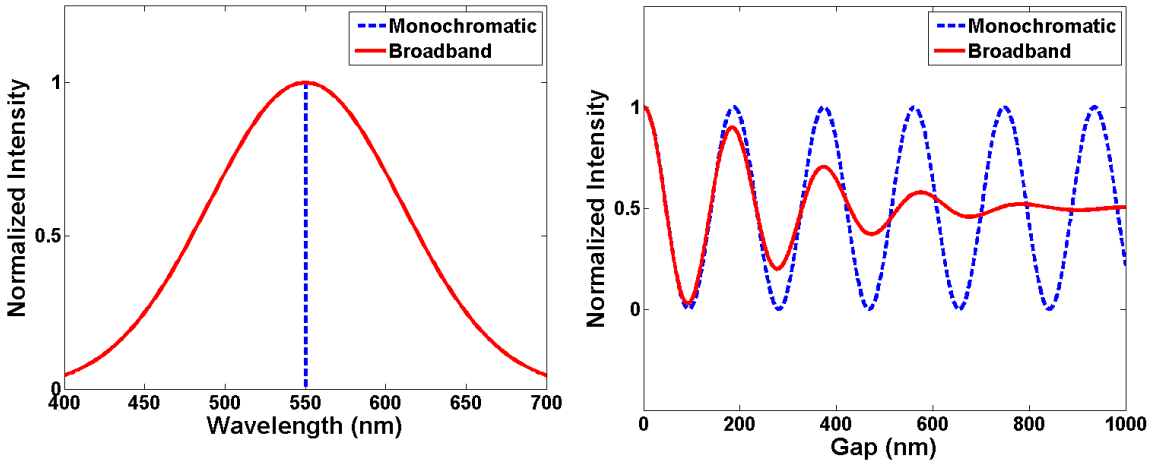


***Figure 5-9:*** ***(a) Ideal spectra of a monochromatic and a broadband light sources (b) Evolution with the gap of the calculated fringes intensity***

It can be seen that for the broad distribution wavelength source, the intensity of the fringes decreases very rapidly while the intensity of the monochromatic 530 nm source is constant. Also, the pseudo-period of the fringes is very close to the period of the monochromatic light fringes. In practice, this dampening of the fringes limits the thickness of the films that can be measured using interferometry. To quantify this limit, a useful concept is the *coherence length*. This represents the physical length at which the intensity of the fringes has been reduced by 50 %. For a Gaussian distribution:

$$L = \frac{2\ln(2)}{\pi n} . \frac{\bar{\lambda}^2}{\Delta\lambda} \qquad (27)$$

where $\bar{\boldsymbol{\lambda}}$ is the average wavelength of the light source, here 550 nm, and $\boldsymbol{\Delta\lambda}$ is the full wavelength width of greater than or equal to the half maximum, *i.e.* the width of the part of the spectrum that is above 50 % of the maximum value, thus about 140 nm. The coherence length is 650 nm, which corresponds to a film thickness limit of 325 nm (half the physical length of the path). Hence to be able to be able to measure thicker films, it is necessary to use a more coherent light source with a narrower spectrum.

Whether it is a normal CCD or 3CCD, every camera has a particular spectral response, which will make it more or less sensitive to different wavelengths and will influence the choice of the light source. The spectrum of the camera used in this study is shown in Figure 5-10.

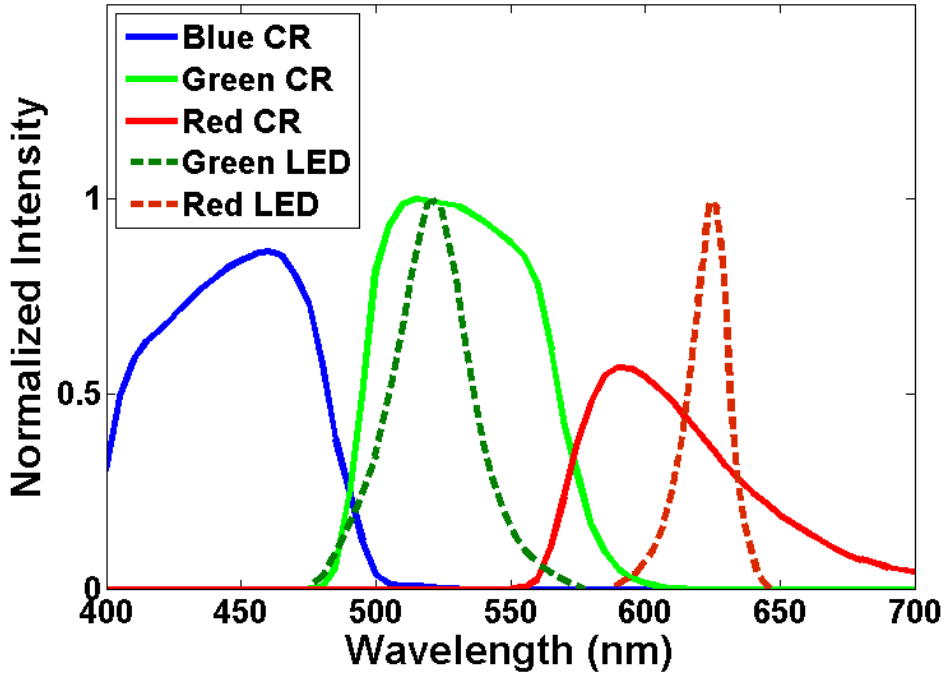


***Figure 5-10:** Camera response (CR) of a Hitachi HV-F202 GV camera along with the spectra of the LED used*

The intensity of the fringes captured by a camera will be modulated by this camera response. Suppose interferences are formed using a broadband white light; each channel of the camera will be sensitive to part of the spectrum. If $I_i$ is the intensity of the fringes captured in one channel (red, green or blue) and $R_i$ is the camera response for this channel, the variation with increasing gap will be:

$$I_i = \sum_{\lambda} R_i(\lambda) S_i(\lambda) . \left(1 + \cos\left(\frac{2\pi}{\lambda} . 2nh\right)\right) \quad \textbf{(28)}$$

Figure 5-11 illustrates how the fringes will evolve with film thickness.

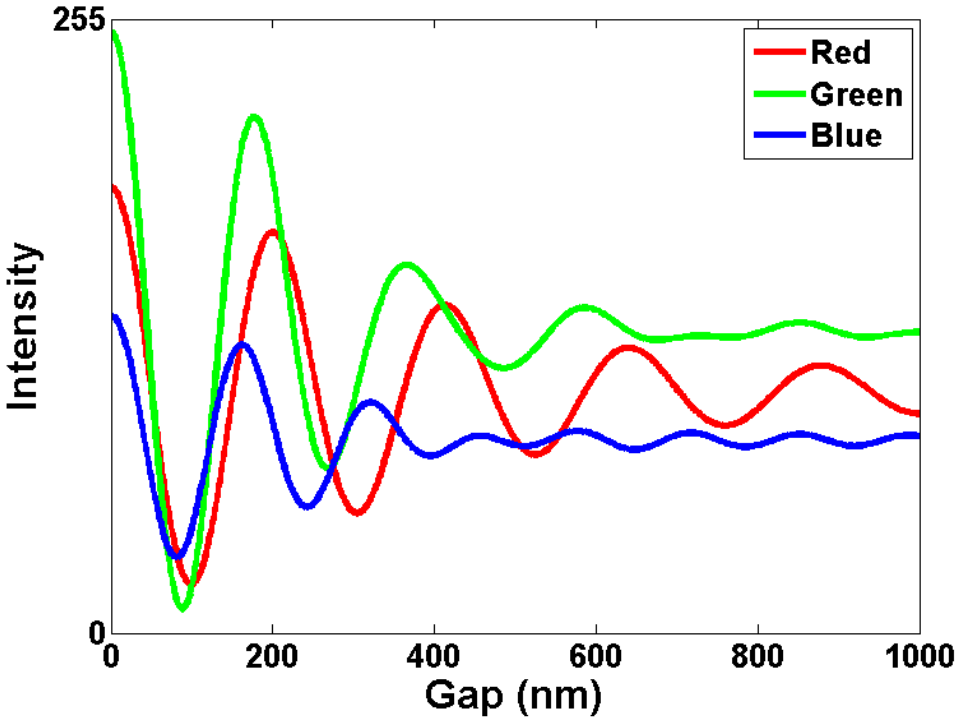


***Figure 5-11:*** ***Example of the evolution of intensity of the fringes with increasing gap***

The intensities of the fringes evolve in a similar way to that shown in Figure 5-9. However the three curves have different pseudo-periods that correspond to the average wavelength of the spectrum modulated by the response of their respective filters. They have different mean values and amplitudes because neither the spectrum nor the camera response is flat.

What Figure 5-11 suggests is that capturing interferograms with a colour camera is equivalent to acquiring three monochromatic interferograms at the same time. Hence, in order to obtain the best fringe visibility, the ideal light source is a sum of three monochromatic light sources that emit in only one channel of the camera. As can be seen in Figure 5-10 there is significant overlap between the channels, for example between 550 nm and 600 nm incoming light will stimulate both the green and the red channel and this will affect the quality of the fringes.

#### 5.3.2.2. Duo-chromatic System

A schematic of the solution used in this study can be seen in Figure 5-12. It consists in a composite light source made with a green LED (530 ± 15 nm) and a red LED (617 ± 8 nm).

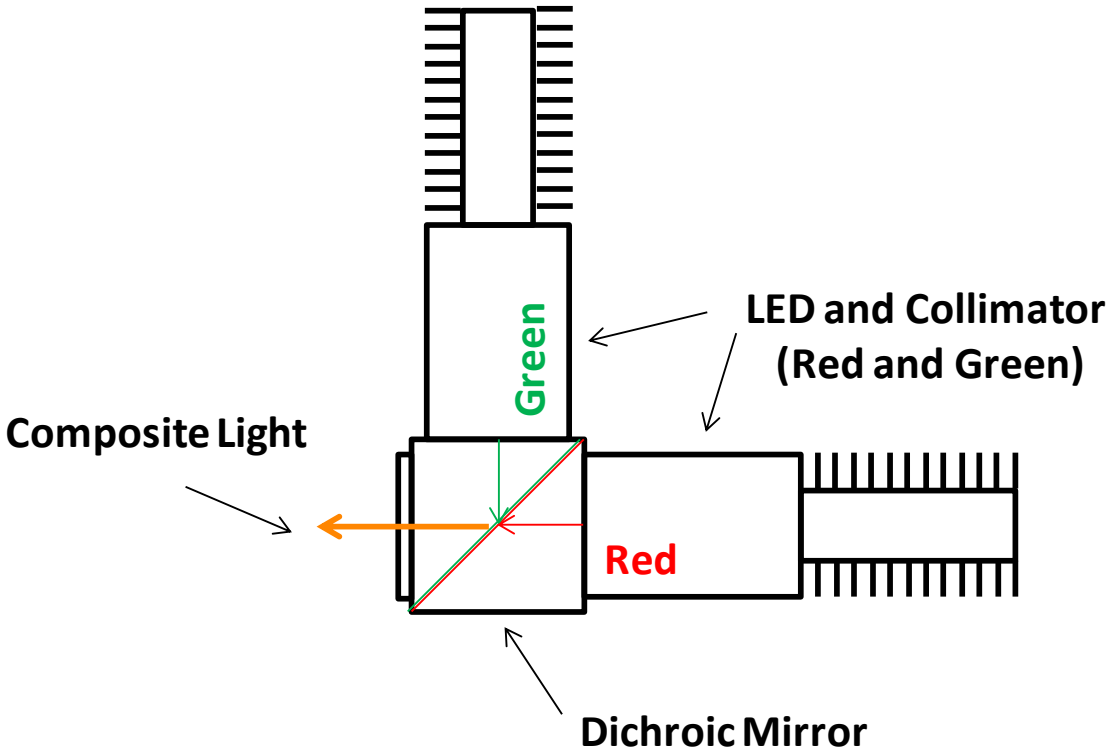


***Figure 5-12:** Schematic of the composite light source set-up*

LEDs were chosen because of their illuminating power and their good coherence that ensures good fringe visibility. Their spectra are plotted along with the camera response in Figure 5-10; they show that the overlap between channels is minimal. The effect of replacing the original halogen light source by a system with two LEDs can be seen on Figure 5-13. As the gap increases outside of the contact, it is evident that the fringes produced with the halogen light dim much more rapidly than the ones produced by the LEDs, which shows that the duo-chromatic enables the measurement of much thicker films.

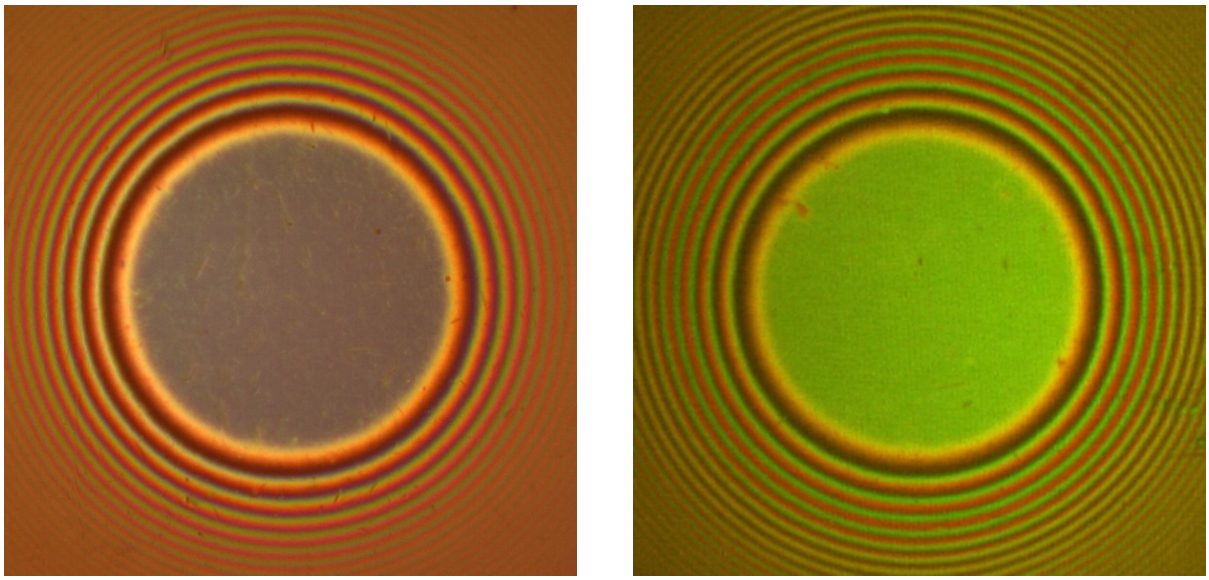

***(a)*** ***(b)***

***Figure 5-13:*** ***Static dry contacts in the smooth case showing the interference fringes produced by (a) halogen light and (b) composite light source***

Due to their high divergence, the LED light sources were collimated prior to being recombined with a dichroic mirror. This allowed the loss of illumination due to the divergence to be reduced. The resulting light source enables measurement of lubricant films that are over a micron thick. Such a duo-chromatic system has been employed in the past, for example by Wedeven [26] and Kaneta and Cameron [51], but involved filtering a white lamp rather than using LEDs.

The ideal light source would have comprised three LEDs. The reason why a duo-chromatic system was preferred over a tri-chromatic system is that the latter would have required a difference optical set-up that would have inevitably increased the distance between the LEDs and the contact. The intensity of the images would have been affected, which was critical as the exposure time needed to be very fast. The duo-chromatic set-up was much easier to implement and provided enough light to the contact.

### 5.3.3. Friction Measurement

As supplied with the test rig, the friction measurement system was an automatic one with a specific control and processing program. Two drawbacks of this program were (i) that it did not allow friction to be measured at fixed SRR while increasing the entrainment speed and thus the film thickness and (ii) that it averaged the friction over several rotations of the ball making it impossible to study the influence of localised roughness on friction.

To overcome these limitations, the output voltage of the torque meter was diverted and amplified and then measured in real time with the same Labview card used to capture the interferograms. That way, the film thickness and transient friction measurements could be made at the same time with one single program.

One precaution had to be taken at the beginning of the test when measuring friction. When the ball is loaded against the disk, the ball shaft bends slightly and the various elements of the drive train (seals and bearing) provide some resistance which offsets the friction measurements. To measure this offset, the output of the torque meter was measured in pure rolling with a smooth ball for the range of ball speeds studied and used to correct the measurements made in rolling/sliding.

It was important to confirm that the offset did not evolve with time and as seen on Figure 5-14 no such time evolution was observed. It can be seen that at high speed the measurements are repeatable while at lower speeds they are more scattered. This is due to the speed control of the EHD rig that is not able to apply exactly pure rolling at low speeds, thus at these speeds there will always be some amount of sliding (positive or negative). In order to estimate the offset at these speeds, a best fit was found in the form of a logarithmic

parabola. It should be noted that the friction measurements presented in this study all use this fit.

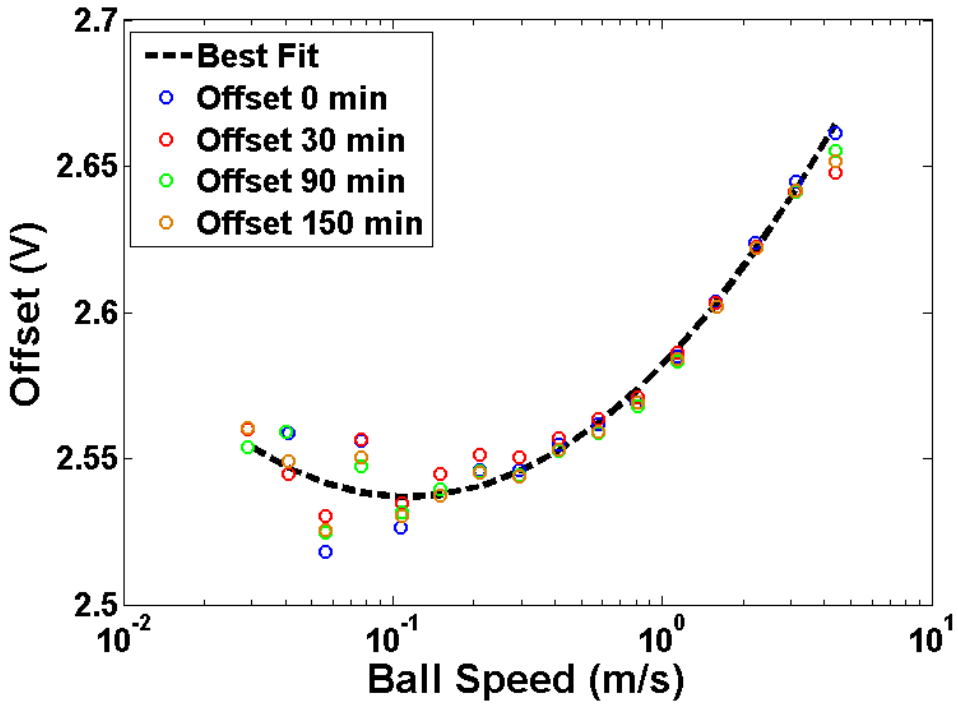


***Figure 5-14:*** *Offset of the torque meter vs. Ball Speed after different time of continuous running at 40°C*

## 5.4. Test Specimens

The ball specimens were all drilled AISI 52100 steel balls with a diameter of 19.05 mm (3/4”). Balls with three different roughness structures were tested in this study. The textures were produced by careful machining the ball on a lathe to achieve periodic circumferential ridge-valley texture (parallel to the rolling/sliding direction). By varying parameters such as the feed rate and the radius of the cutting tool it was possible to obtain surfaces with different dominant wavelength and peak-to-valley heights. The topographies of the three selected roughnesses used for most of this study are shown in Figure 5-15.

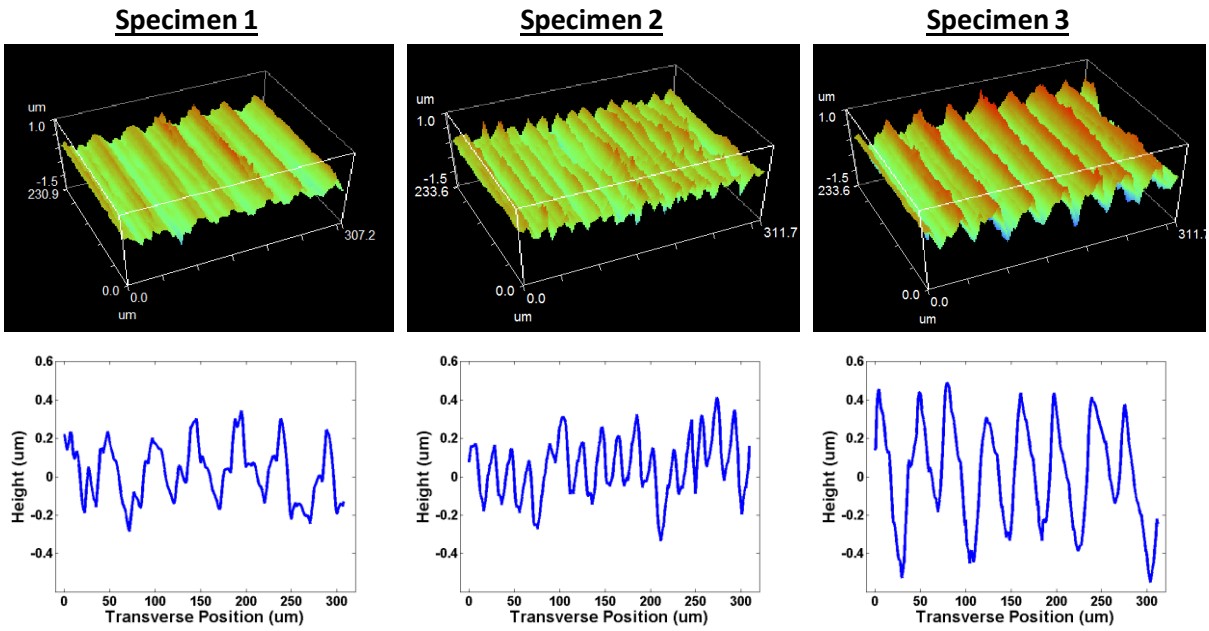


***Figure 5-15:*** ***Surface profiles of the three selected specimens as measured with a white light interferometer***

Using a dedicated jig with angular positioning, it was possible to precisely locate the roughness and then capture the film thickness in this position. The measured roughness properties of the three selected rough specimens are listed in Table 2.

***Table 2:*** ***Roughness parameters of the different specimens extracted via FFT***

| | Average Peak-to-valley height (µm): H | Dominant Wavelength (µm) (FFT analysis) | RMS (µm) |
|---|---|---|---|
| Specimen 1 | 0.52 | 45 | 0.15 |
| Specimen 2 | 0.49 | 19 | 0.15 |
| Specimen 3 | 0.97 | 39 | 0.27 |

## 5.5. Experimental Protocol

Before use, disk, ball specimens, ball shaft, ball carriage and lubricant pot were consecutively soaked in toluene and isopropanol. They were then dried with a heat-gun in order to eliminate any trace of solvent.

The pot was filled with the test lubricant and left for 30 min in order to allow the set temperature (disk + ball specimen + lubricant) to stabilize. A particular ball position was

chosen from which all the measurements of film thickness were subsequently taken. The position of the disk was also logged to enable the partial triggering.

## 5.6. Test Conditions

The specimens were tested in the ball-on-disk rig at the conditions listed in Table 3.

***Table 3:** Experimental conditions*

| Temperature | Load | Speed Range | SRR |
|---|---|---|---|
| 40.0 ± 0.5°C | 20 N | 0.02 to 2 m/s | Film thickness: 0% and 50%<br>Friction: 50% and 100% (additionally, a few tests at lower SRRs) |

The SRR was defined as:

$$SRR = \frac{U_{Disk} - U_{Ball}}{U_e}$$

where $U_e$ is the entrainment speed equal to the average of $U_{Disk}$ and $U_{Ball}$.

In all the tests, a load of 20 N was applied, giving a nominal Hertz pressure of 0.527 GPa and a contact diameter of 269 µm based on smooth surface calculation. In the case of rough surfaces and this film conditions, the load is mostly born by the asperities so the local pressure is expected to be higher. In this work, the case of positive slide-to-roll ratio (SRR) was investigated, i.e. the disk moves faster than the ball.

Two lubricants with very different viscosities were tested. The lower viscosity one was Shell Turbo 68, a Group II base oil with anti-oxidant additives. The second lubricant was a Group I base oil. The properties of the lubricants were measured and are listed in Table 4. The test temperature was 40°C in all cases.

***Table 4*: Oil properties**

| | Viscosity at 40°C (cP) | Viscosity at 100°C (cP) | Refractive index at 40°C |
|---|---|---|---|
| Shell Turbo 68 | 57.7 | 7.1 | 1.469 |
| Group I | 233.7 | 24.3 | 1.47 |

These lubricants and the test temperature were chosen to enable a full span of the lubrication regimes over the chosen entrainment speed. As seen on Figure 5-16 for every entrainment speed, the film thickness generated by the more viscous lubricant was twice that of the less viscous one. In both case, the SRR did not have any effect on the measured film thickness.

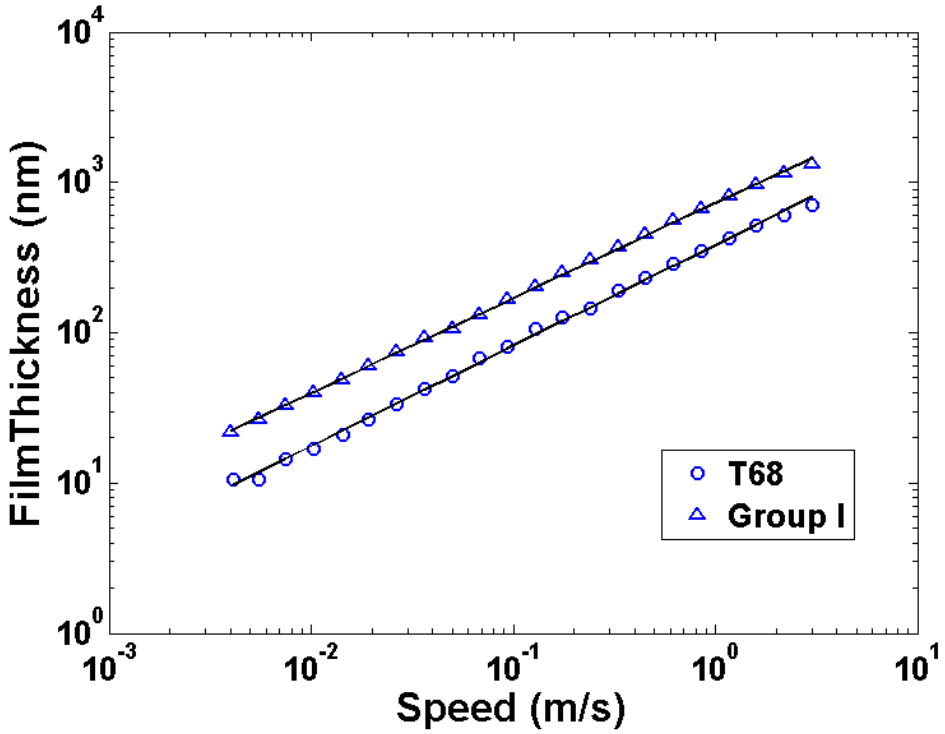


***Figure 5-16*: Film thickness vs. entrainment speed for the two test lubricants with smooth specimens at 40C**

In principle the two curves should overlap when plotted against $\eta U$ with $\eta$ the dynamic viscosity of the lubricant and $U$ the entrainment speed. This means that if, to give a certain film thickness, speed $U_1$ is needed for the group 1 oil and $U_2$ for the T68 then $\eta_{T68} U_2 = \eta_{Group\ I} U_1$. Since $\eta_{Group\ I} / \eta_{T68} = 4$ this means that $U_1 / U_2$ should be 4. However this supposes the lubricant film thickness is determined only by dynamic viscosity. In practice it was found that

$U_1 \approx 2.8\, U_2$ was more appropriate. Hence, T68 requires a much higher entrainment speed than the Group I oil to build-up a given film thickness. This is probably because its pressure viscosity coefficient is lower, as is normal for a Group II as compared to a Group 1 oil.

## 5.7. Novel Procedure for Optical Measurements

### *5.7.1. Limitation of the Standard Imaging Techniques*

When using optical interference techniques to map film thickness, two issues had to be addressed.

First, a correspondence between the lubricant film thickness and the colour intensity had to be determined. This is the "calibration curve" already discussed in section 3.1.1.4(c).

The second issue that had to be addressed is that, due to experimental error and the quasi-periodic nature of the calibration curve, it is possible for a given set of colour intensities to give several solutions for the film thickness. In practice, previous researchers have either focused on film thickness values that fall in the first period of the calibration curve (i.e. below 250 nm), or a range of film thickness has been defined and the best match is chosen within it.

All the imaging techniques give the correct intensity variation trend of the interference fringes against film thickness but they also assume that the surfaces studied are as reflective as smooth surfaces. However, when rough surfaces are considered, it is observed that reflected light is diffused, as opposed to the specular reflection of smooth surfaces. Hence for a given film thickness the corresponding intensity of the interference fringes will be lower for rough than for smooth surfaces.

To enable the measurement of both very thick films and from rough surfaces, a novel procedure for film thickness measurements was developed. This involves two steps.

### 5.7.2. Optical Properties of the System: Interference Fringes Period and Initial Phase Shift

Similar to Molimard [27], a smooth ball is loaded against the disk in the presence of lubricant and the intensities of the circular red and green fringes are scanned radially as shown in Figure 5-17.

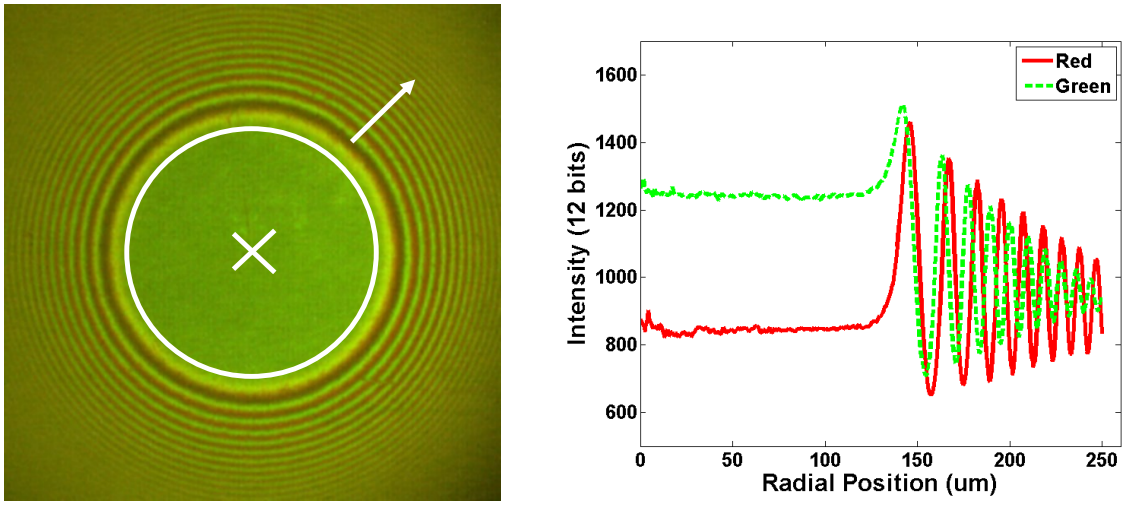


*(a)* *(b)*

***Figure 5-17:*** *(a) Interferogram showing a static ball-on-disk contact in presence of lubricant, (b) Intensity of the fringes*

Using Hertz theory, the gap outside of the contact is calculated and related to the intensity of the fringes. This is shown in Figure 5-18 .

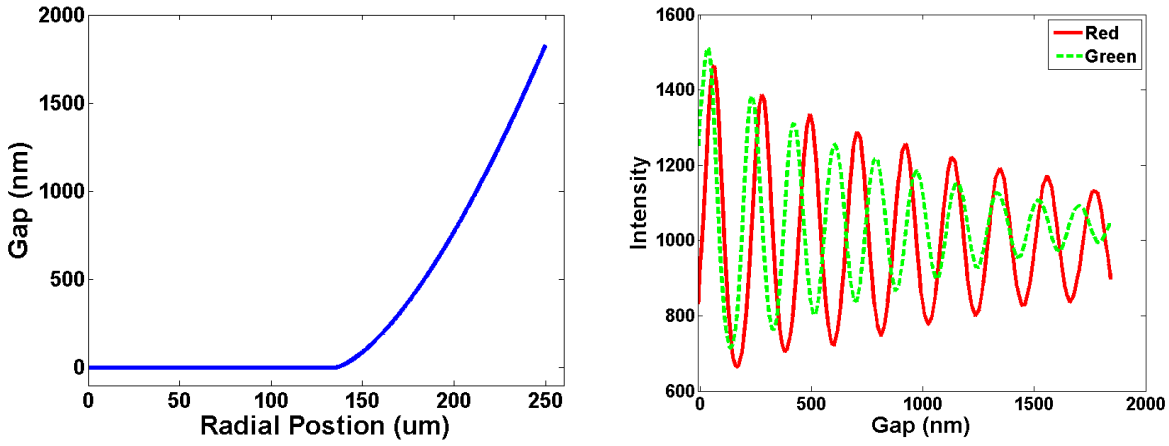


*(a)* *(b)*

***Figure 5-18****: (a) Gap calculated using Hertz theory, (b) Intensity of the fringes versus gap, the amplitude of the waviness decreases with increasing gap*

As evident in Figure 5-18, due to factors such as the loss of coherence of the light and the curvature of the ball, the amplitude of the fringes decreases with the increasing gap. To eliminate this effect the relative optical interference intensity (ROII) can be used. Equation (20) is reproduced below:

$$\bar{I} = \frac{2I - I_{max} - I_{min}}{I_{max} - I_{min}} = cos\left(\frac{4\pi nh}{\lambda} + \Phi\right) \quad \textbf{(20)}$$

The effect of this transformation can be seen in Figure 5-19 for the red fringes; the curve shown is a normalization of the original curve by the adjacent minimum and maximum intensities and has a very similar form to a cosine function. The period of this curve is equal to the period of interference that would be produced by monochromatic light whose wavelength is equal to the average wavelength of the light source modulated by the camera's spectral response. The initial phase shift corresponds to the contribution of the spacer layer thickness and the phase shift due to the chromium layer.

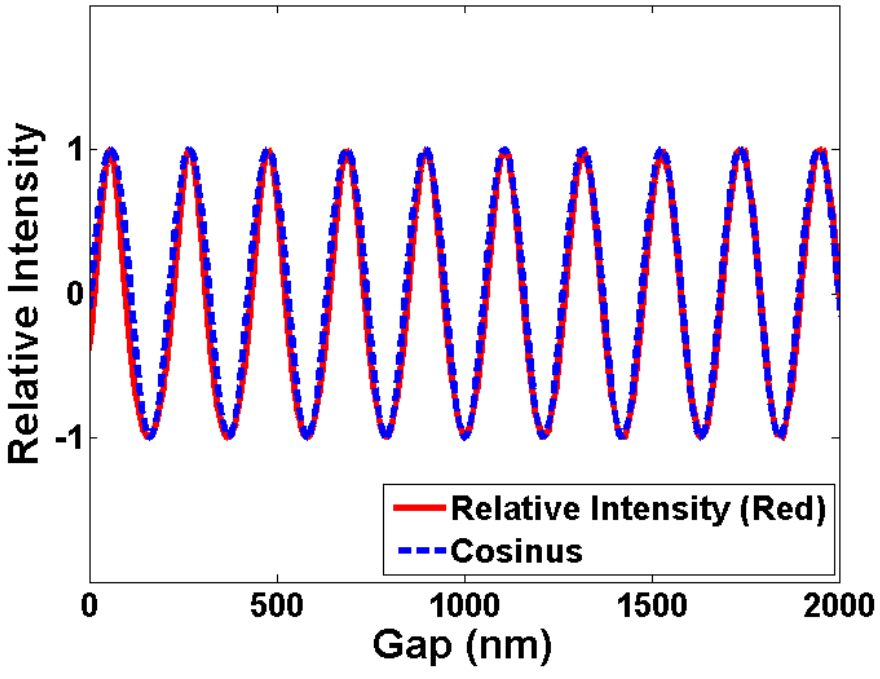


***Figure 5-19**: Comparison between relative Intensity of the fringes around a static contact and a pure cosine*

From Figure 5-19, it is apparent that the normalised intensity curve can be modelled by a cosine. Consequently, provided that the order of interference is known, the film thickness ***h*** can be calculated using:

- If the intensity is decreasing on the period:

$$h = h_{peak} + \frac{\lambda}{4\pi n}\arccos(\bar{I}) \quad \textbf{(29)}$$

- If the intensity is increasing on the period:

$$h = h_{trough} - \frac{\lambda}{4\pi n}\arccos(\bar{I}) \quad \textbf{(30)}$$

The red and green channels can be used independently to calculate the film thickness and were found to give almost identical results. In this study, the film thickness is taken as the average of the film calculated using the two channels to reduce experimental noise.

### *5.7.3. Image Analysis*

For any particular point within the contact, the adjacent minimum and maximum intensities that need to be considered to calculate the ROII are not easily accessible. For example, when the surface is rough, the order of interference is not always known because of large variations in film thickness within the contact. Another parameter that may modify the amplitude of the fringes is the local orientation of the surface, which is affected by the presence of asperities. Hence a rough surface that is illuminated perpendicularly tends to diffuse the incident light, which reduces the amplitude of the interference.

To obtain the local values of the minimum and maximum intensities that need to be used to calculate ROII, a series of images is taken at different speeds, and the change in intensity of

both colours is followed at each point. Assuming that the speed increase step is small enough that no order is missed, and that the film thickness monotonically increases with speed, it becomes possible to calculate the ROII everywhere. The high resolution of the ball shaft encoder and the fast shutter speed help to ensure that all images are taken near the same spot on the ball as illustrated in Figure 5-8. However, despite these precautions, the contact tends to move by a few pixels from one image to another. To correct for this, a correlation algorithm is used to realign the images before analysis.

This algorithm is very easy to implement. It consists in calculating the circular cross-correlation of each consecutive image. In this work the green channel was used to calculate the cross-correlation because the camera is more sensitive to the green. The small speed steps used ensure that the film thickness does not change much between each consecutive image, so that the images are similar enough to be realigned. The circular cross-correlation ***CC*** of two images (***Im₁*** and ***Im₂***) of the same size can be obtained very quickly *via* their **FFT**:

$$CC = IFFT\left(\widehat{Im_1}.\widehat{Im_2}^{*}\right) \quad \textbf{(31)}$$

where **IFFT** is the inverse Fast Fourier Transform and ***** designates the complex conjugate. The cross correlation is a matrix of the same size as the images; the coordinates of the maximum give the shift in pixel between the images.

By applying this algorithm to each image consecutively, the images are all aligned with each other. Then they are stacked and the evolution of the red and green intensities against speed is observed at every point independently. The ROII is then calculated for each point of the contact at every speed following the method described previously. Figure 5-20a and Figure 5-20b respectively show an example of recorded red and green intensities and the calculated ROII.

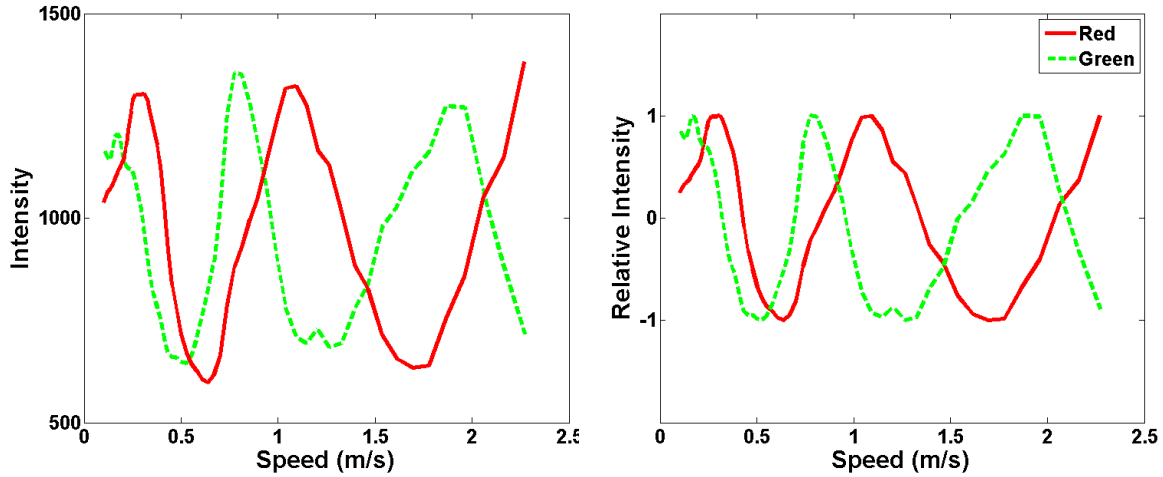


***Figure 5-20:*** *(a) Variation in the intensity of the red and the green with speed for a particular point in a rough contact, (b) Calculated ROII*

Using these data and equations (29) and (30), it becomes possible to calculate quite reliably the film thickness for each speed everywhere in the contact. Equally, at each speed considered, a map of film thickness can be obtained. An example of calculated film thickness at a selected point and a complete film thickness map are shown in Figure 5-21a and Figure 5-21b respectively.

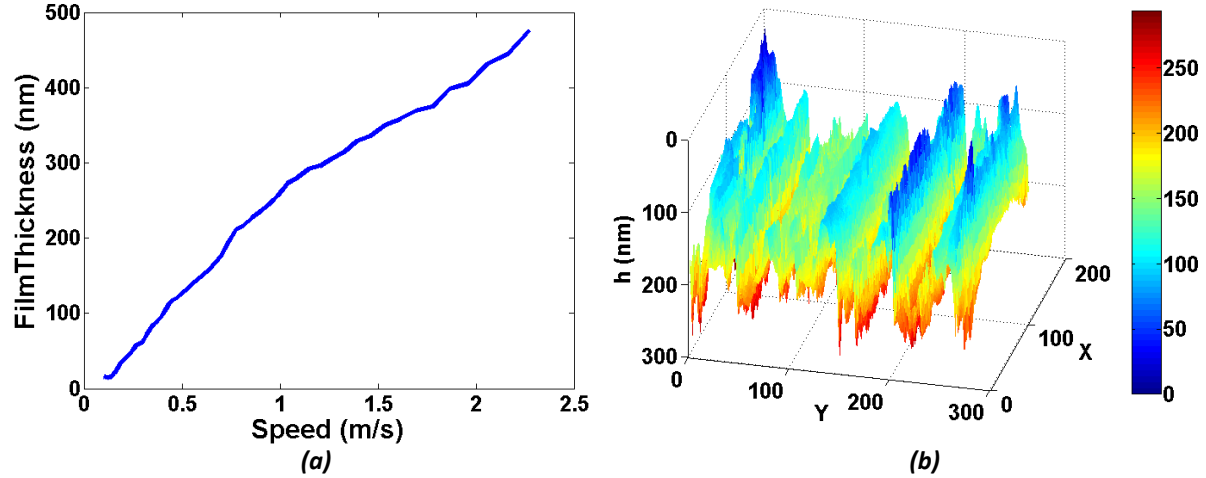


***Figure 5-21:*** *(a) Film thickness against entrainment speed at one point in the contact, (b) Example map of film thickness of a lubricated rough contact at a particular speed*

Unlike in smooth contacts, in rough contacts there is no one single value of minimum or central film thickness. In order to be able to extract representative values of film thickness

from the obtained maps, a rectangular area equivalent to the flat central area of the smooth contact is selected inside the contact, avoiding the constriction. Maps are generated for a range of entrainment speeds, and then the following values are calculated:

- Minimum film thickness: average of the lowest 1% of points. This value is taken to represent the film thickness at the tops of the asperities.
- Maximum film thickness: average of the highest 1% of points. This value is taken to represent the film thickness in the valleys between the asperities.
- Average film thickness.
- RMS roughness of the separation, this is calculated as the standard deviation of the film distribution.
- Solid-to solid contact: percentage of the contact area that is “in contact”, determined as the points where the film thickness is measured to be 0 nm.

## 5.8. Inverse Solution Method

Molimard et al. [78] and Krupka, Vrbka, et al. [81] have shown that when accurate film thickness maps are available it is possible to use these as inputs to estimate the pressure distribution. Assuming the material properties are known, the only real difficulty is to measure the undeformed geometry in the same spot where it will be tested on the ball-on-disk rig. To do so, prior to measurement an indent was produced on the ball using a diamond cone (Rockwell C indenter). The out-of-contact geometry was then measured using a white light interferometer (WLI). Figure 5-22 shows an interference image of a static rough contact and a corresponding surface topography map observed under the WLI. It can be seen that the images show the exact same spot on the ball.

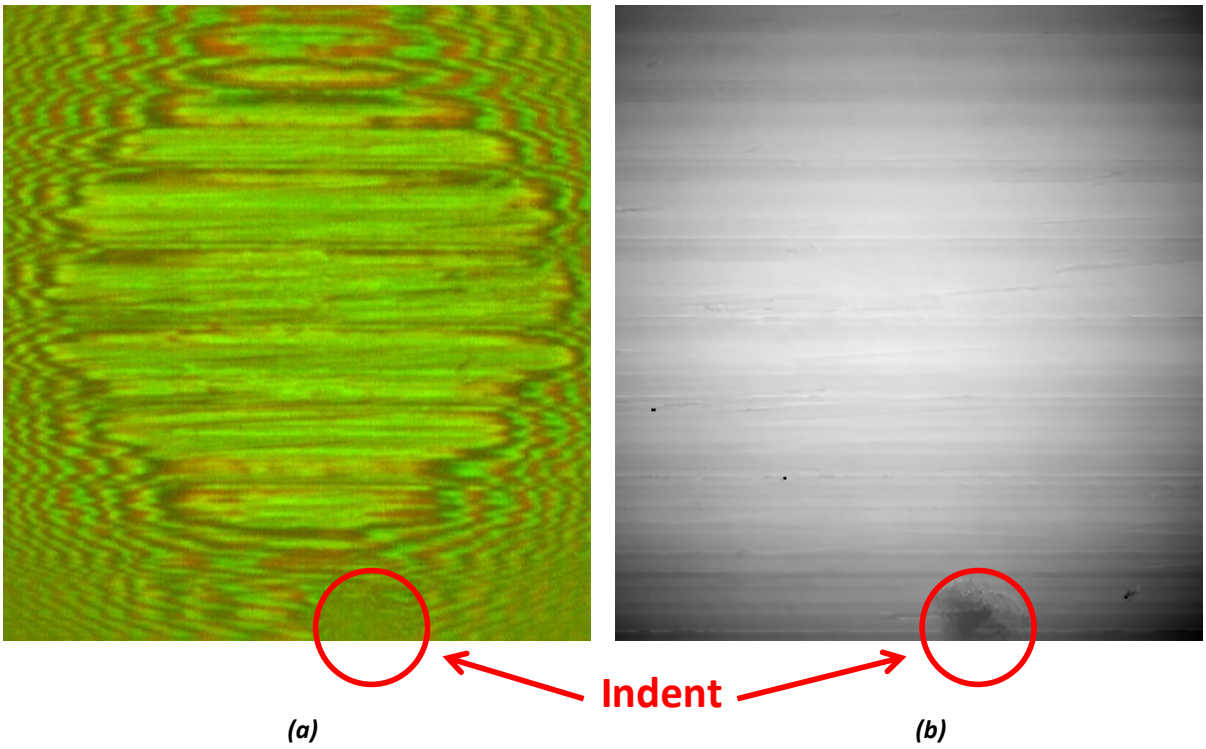


***Figure 5-22:** (a) Static Contact as seen on the ball-on-disk set-up showing an indent, (b) same location observed under WLI*

As the resolution and the magnification of the two images did not originally match, the topography taken with the WLI was interpolated and cropped in order to be fully comparable to the maps taken on the ball-on-disk rig.

To estimate the pressure distribution, the elastic displacement of the surfaces is needed. This can be calculated by taking the difference between the loaded and the unloaded surface topographies and adding a penetration value, the approach of centres of the two bodies. The latter is an unknown constant and to obtain it, the displacement was approximated as Hertzian outside of the contact area, the constant was then found by determining the difference between the two solutions at the edge of the contact. Figure 5-23 shows the transverse profile of the displacement field before and after this operation. One disadvantage of this method is that it assumes that the pressure outside of the contact is zero. This is valid for static and low speed contacts, but is not the case for lubricated contacts at high speeds where the inlet pressure can become significant. To evaluate the inlet pressure it is possible

to extrapolate the film profile around the contact and this was explored, but was found not to significantly affect the calculated pressure distribution within the contact area. Thus it was not implemented in analysing the results in this thesis.

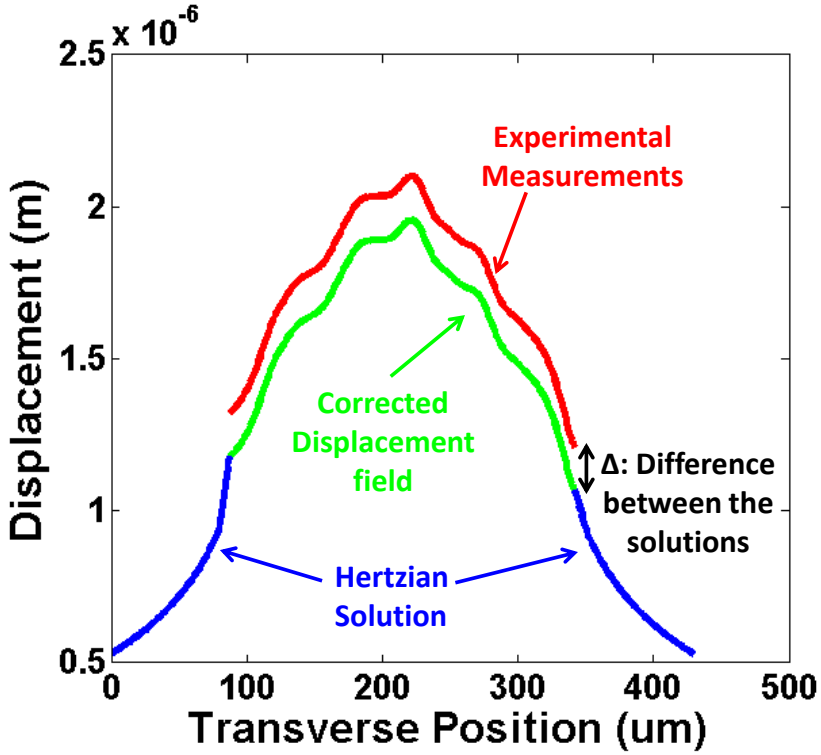


***Figure 5-23**: Illustration of the procedure to calculate the displacement field*

The influence coefficient technique was then used to link this displacement field to the pressure distribution as explained in Chapter 4 of this thesis.

As well as the predominant longitudinal ridge texture, the ball surfaces also had much finer roughness features, predominantly along the rolling direction, with wavelength ca 1-5 um and amplitude 10-20 nm. Since the focus of this study was the impact of the ridges on pressure, the displacement was smoothed prior to being used as input to calculate the pressure distribution. To do so, the macro-curvature was first extracted using a discrete cosine transform (DCT), and then the result was smoothed with a simple averaging filter that uses a

square window as kernel. It was observed that the smoothing led to a slight reduction of the ridge amplitude and to compensate for this the profile was multiplied by a constant. Finally the macro-curvature was added back to the profile.

# Chapter 6 - Film Thickness Measurements

In this chapter, the effect on film thickness of roughness ridges oriented along the rolling-sliding direction is investigated. The roughness of the three specimens tested is characterized by the RMS of surface heights and a dominant wavelength. Optical interferometry and a ball-on-disk set-up were employed to measure the oil film thickness. Using the procedure described in the previous chapter, film thickness maps were obtained for various experimental conditions. In particular the effect of increasing speed on the film thickness along with the in-contact RMS and the real area of contact were observed. The film maps show that the lift-off speed increases when roughness is introduced compared to smooth surfaces, while the average film thickness remains very close to the smooth case. The general horse-shoe film shape that becomes visible at higher speeds is discussed. Using an inverse solution approach based on measured in-contact roughness, the pressure distribution is estimated in a rough lubricated contact and its evolution with speed is explained. The findings provide important insights into the transition from boundary, through mixed, to full EHD lubrication.

## 6.1. Results

### *6.1.1. Film Distribution*

At the beginning of the test a suitable position was found on the rough ball. Then the entrainment speed was slowly increased and images triggered at this location. The evolution with speed of the interferograms of lubricated contact in the case of a smooth and a rough specimen can be observed in Figure 6-1 and Figure 6-2 respectively. The images were taken

in pure rolling conditions. It is evident that as the entrainment speed increases the colour changes, indicating lubricant film build up. In the rough specimen case, the changes in colour occur faster in the valleys between the asperities, showing that the film build-up primarily occurs in these regions while the tops of the asperities remain in contact.

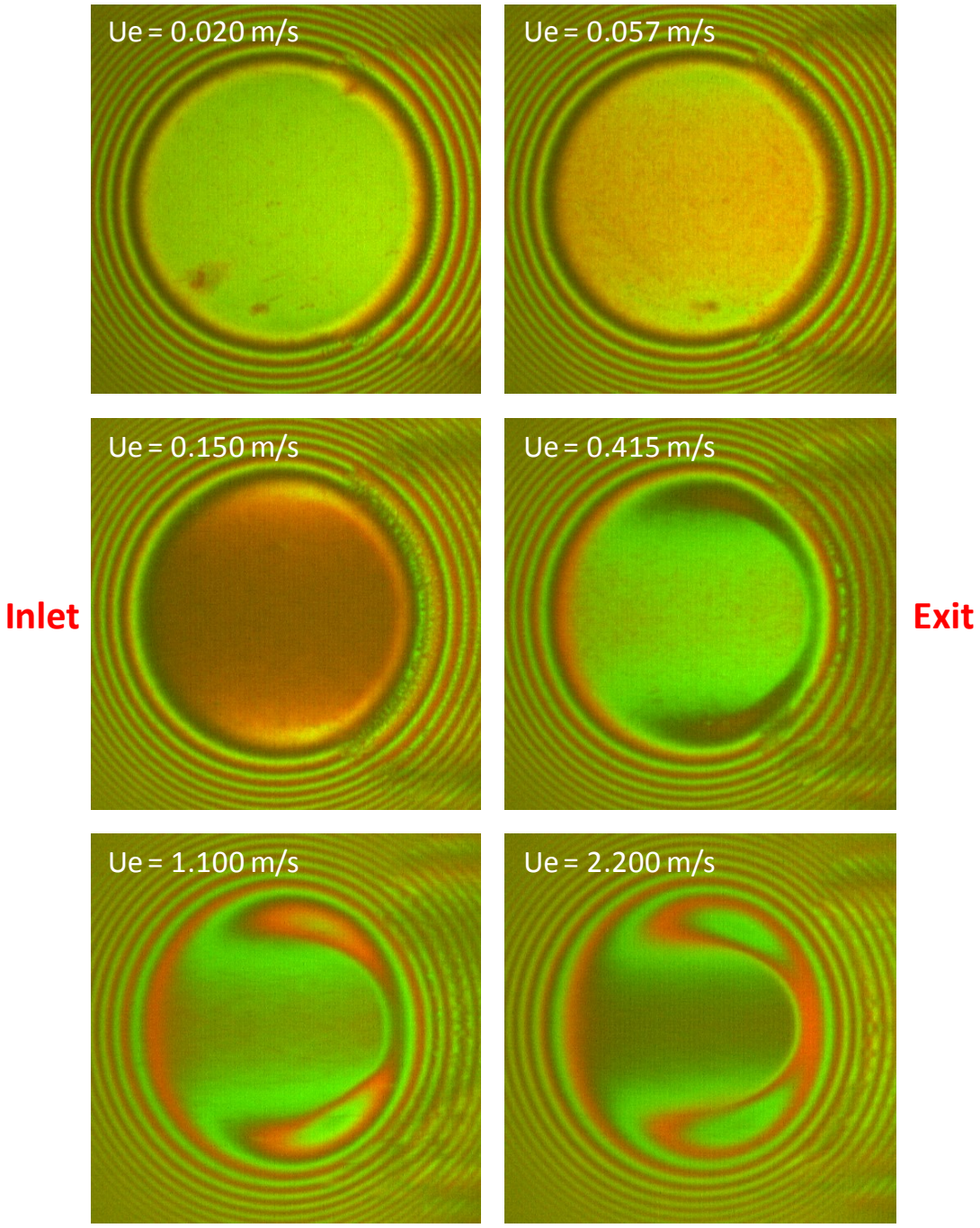


***Figure 6-1:*** ***Interferograms of a smooth specimen at a range of entrainment speeds in pure rolling conditions***

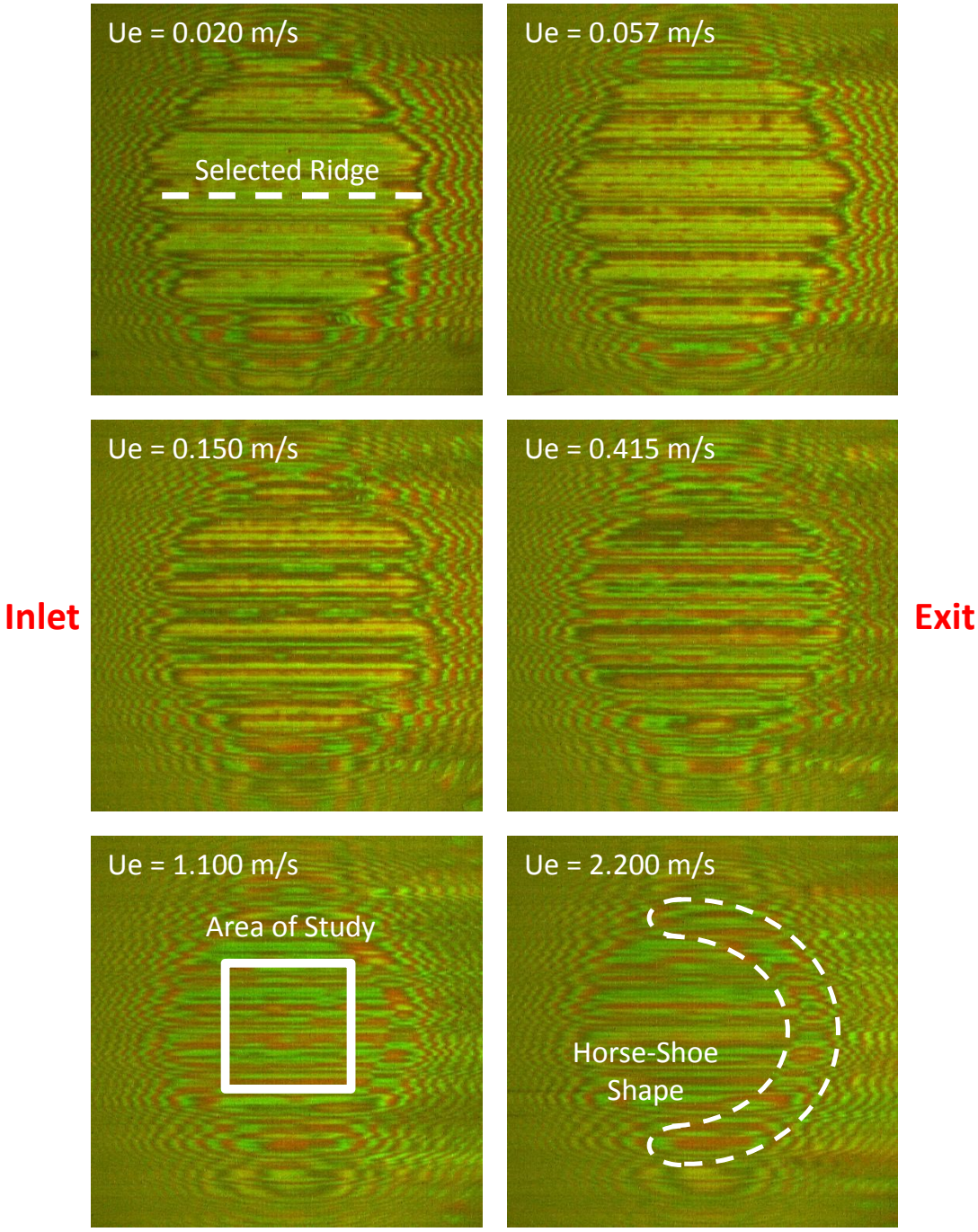


***Figure 6-2 :** Interferograms of rough specimen 1 at a range of entrainment speeds in pure rolling conditions*

The smooth surface shows the classical development of a horseshoe-shaped constriction in the rear and sides of the contact, with minimum film thickness in the side lobes.

In the case of rough specimen, the real contact area is much smaller than in the smooth case. However, as seen in Figure 6-3, in the conditions tested in this study, the contact zone (the

envelope of the contacting points) is of very similar size in both cases. This suggests that the dimensions of the contact are controlled by the macro-curvature, *i.e.* the steel ball curvature.

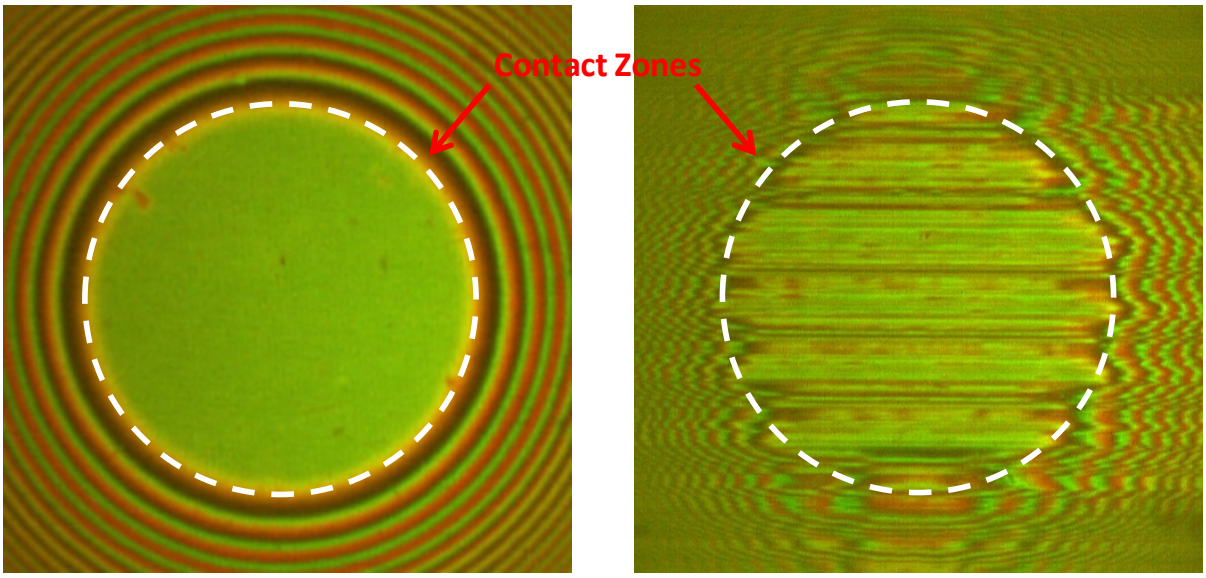


***(a)*** ***(b)***

***<u>Figure 6-3:</u> (a) Smooth and (b) Rough contacts showing their respective contact zones***

An interesting feature was observed at higher speed, when a horse-shoe shape could be distinguished in the rough specimen. This became more and more visible as the speed increased as seen on Figure 6-2.

Figure 6-4a shows the transverse profile of film thickness for a selected set of speeds for specimen 1. At low speeds the surface features are very compressed, leading to an almost conformal contact. As the speed increases, the lubricant film thickness increases and the asperities start to recover. For comparison the film profile for a smooth case at 1.1 m/s is plotted on the chart as a dashed line. This shows that the film shape in smooth and rough cases follow the same general trend. The profile in the rough case varies around a centreline that is well represented by the smooth profile. In the centre of the contact area, the asperities are more squashed than at the edge. This is similar to what happens in the smooth case, where the deformation is larger in the centre.

At the top of the ridges a micro-EHD phenomenon becomes visible. A ridge was selected from the interferograms in Figure 6-2, as indicated in the figure and the evolution of the average film thickness profile along the top of this ridge is shown on Figure 6-4b. In this figure the contact inlet is to the left and the exit to the right.

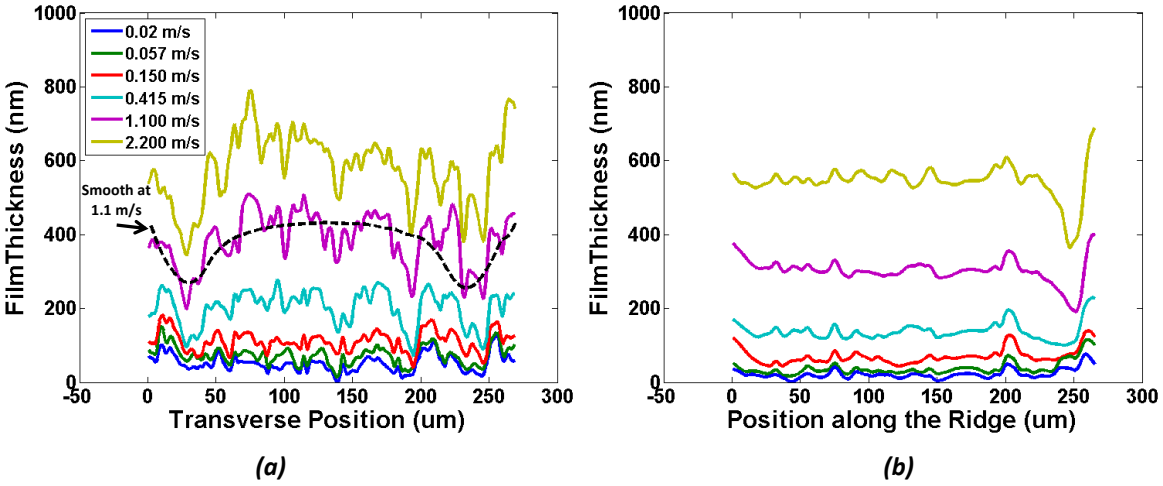


***Figure 6-4:*** ***(a) Film thickness profile in the transverse direction for rough specimen 1, (b) Film thickness profile along the selected ridge at different speeds for specimen 1,***

### *6.1.2. Average Film Thickness Measurements*

As shown in Figure 6-1, a square area was selected on each interferogram and the mean values described in section 5.7.3 were calculated. The area of analysis was chosen to avoid the constriction region so that the measurements could be compared to the central film thickness region measured on a smooth specimen. The specimens were tested under both pure rolling and rolling-sliding conditions at a SRR = 50% over a range of entrainment speeds varying from 0.02 m/s to 2.2 m/s. Figure 6-5 shows the minimum, the maximum and the average film thickness over the selected area in the case of T68 lubricant and the rough specimen 1. The central film thickness measured with a smooth specimen under the same conditions is also plotted for comparison. It is evident that there is very little difference between the nominally pure rolling and 50% sliding cases.

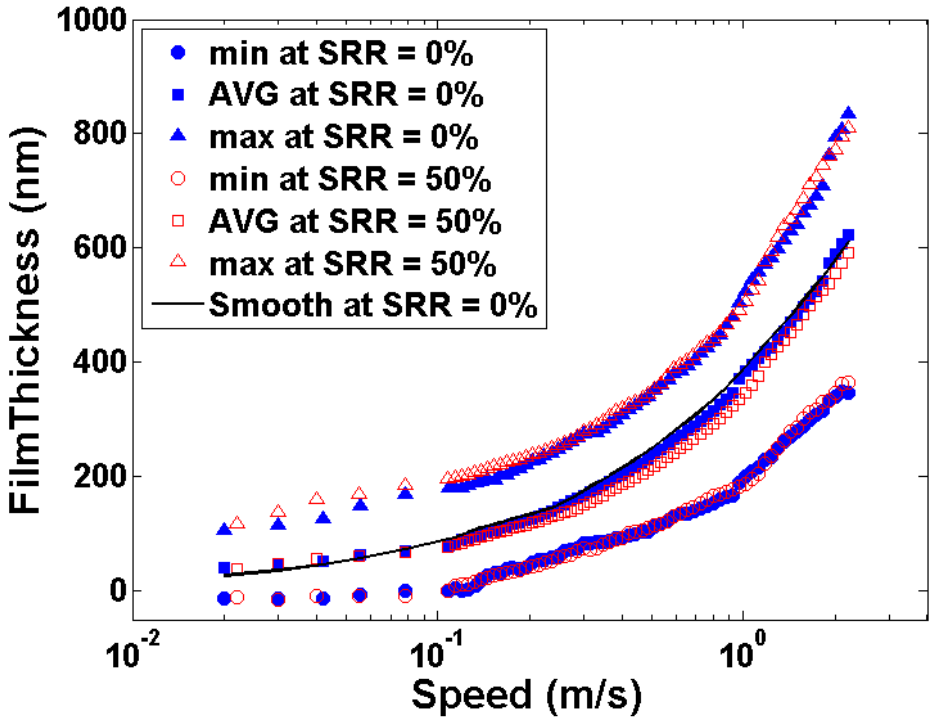


***Figure 6-5:** Film Thickness vs. Entrainment Speed for rough specimen 1 in pure rolling and rolling-sliding conditions*

The minimum and maximum film thickness measured with T68 in pure rolling for the three different rough specimens are shown in Figure 6-6; the average film thickness is not shown because it was very similar for all the roughnesses and is well represented by the smooth surface curve. The three rough specimens all show similar trends:

- The minimum film thickness remains zero up to a critical speed, the "lift-off" speed.
- The average film thickness is very similar to the central film thickness measured on a smooth specimen in the same conditions.

However, it can be seen on Figure 6-6 that, over the range of conditions tested, the surface separation (minimum film thickness) increases at a lower rate for the roughest specimen (specimen 3, RMS = 0.27 µm) compared to the smoother specimens (1 and 2, RMS = 0.15 µm). The wavelength of the roughness seems to have marginal impact as the minimum and

maximum film thicknesses measured with rough specimens 1 and 2, which have a 40 µm and 20 µm wavelength respectively but same RMS, being almost equal.

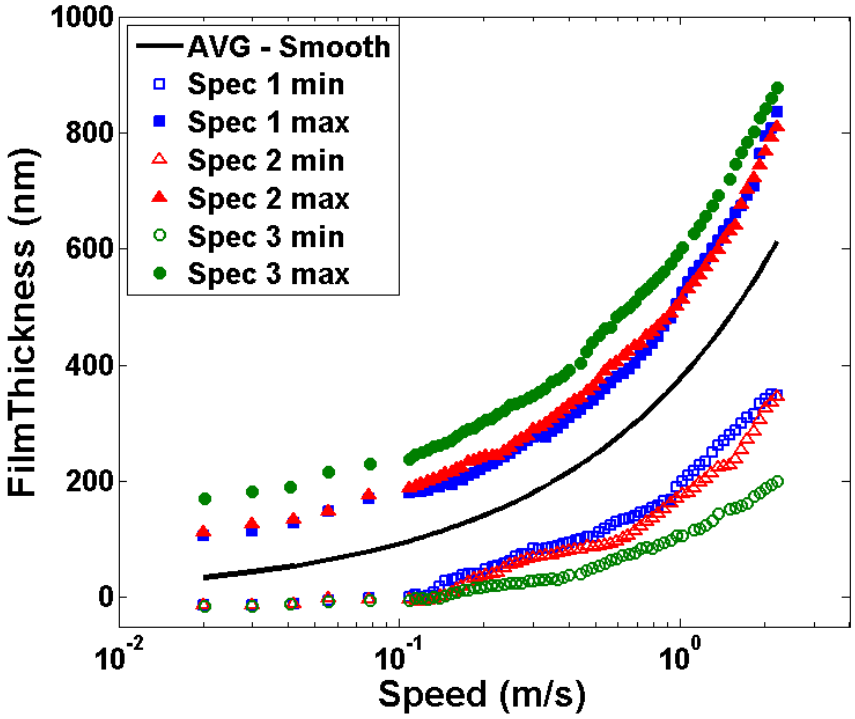


***Figure 6-6:** Comparison of the minimum and maximum film thickness for the different specimens with T68*

The same tests were carried out with the Group I oil. The results are shown on Figure 6-7 and, as expected from a more viscous oil, the film thickness is thicker. Interestingly the same trends are observed in the effect of speed on the roughness parameters.

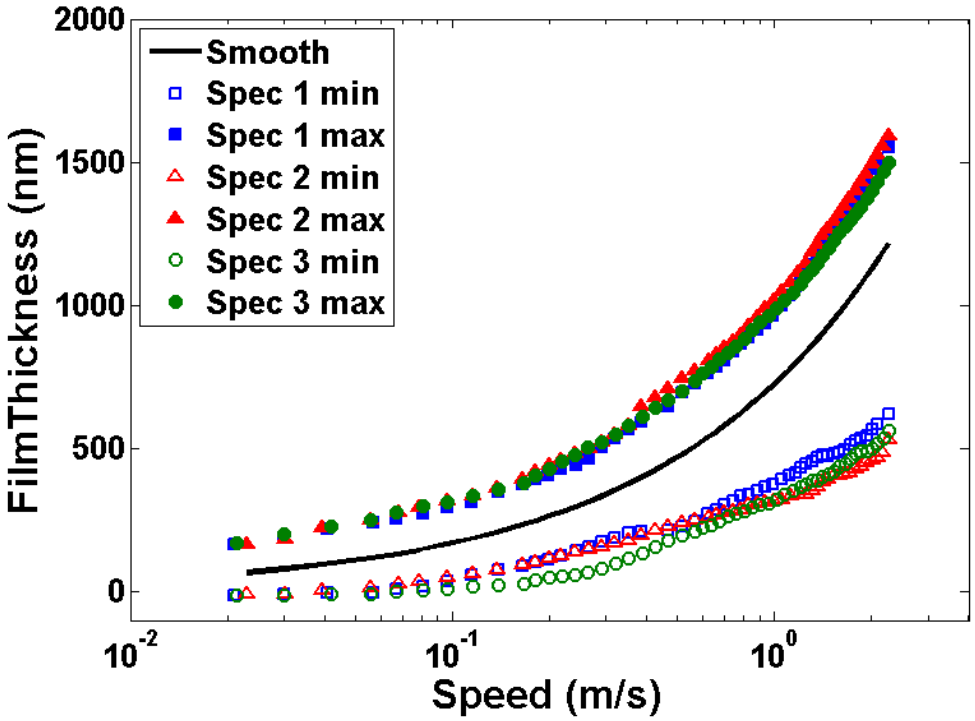


***Figure 6-7:** Comparison of the minimum and maximum film thickness for the different specimens with the Group I oil*

As shown in section 5.6, the smooth central film thickness curves overlap when the speed of the test of the Group I oil are multiplied by **2.8**. Using this factor, it can be seen on Figure 6-8 that the measurements taken with the two oils are very consistent.

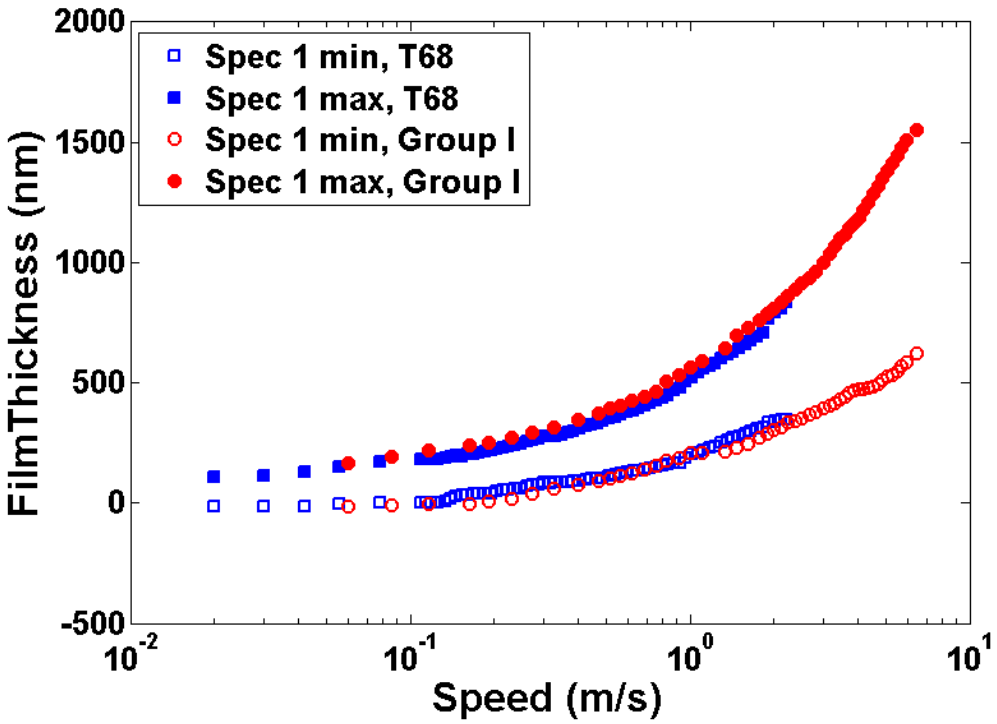


***Figure 6-8:*** ***Comparison of the measurements taken with the two oils with specimen 1, the speed for the Group I oil is multiplied by 2.8***

Using the film thickness maps in the selected area, the RMS of the separation was calculated. The practical significance of this RMS value is discussed later in this paper. Figure 6-9 shows, for the case of T68, how the ratio between this in-contact RMS and the undeformed RMS measured outside of the contact is affected by an increase in the entrainment speed. While it is greatly reduced at low speed compared to the unloaded out of the contact RMS, lubricant film build-up enables the roughness to partially recover at higher speeds. The RMS of the two specimens with the same undeformed RMS recovers at approximately the same rate, while the roughest specimen recovers more slowly.

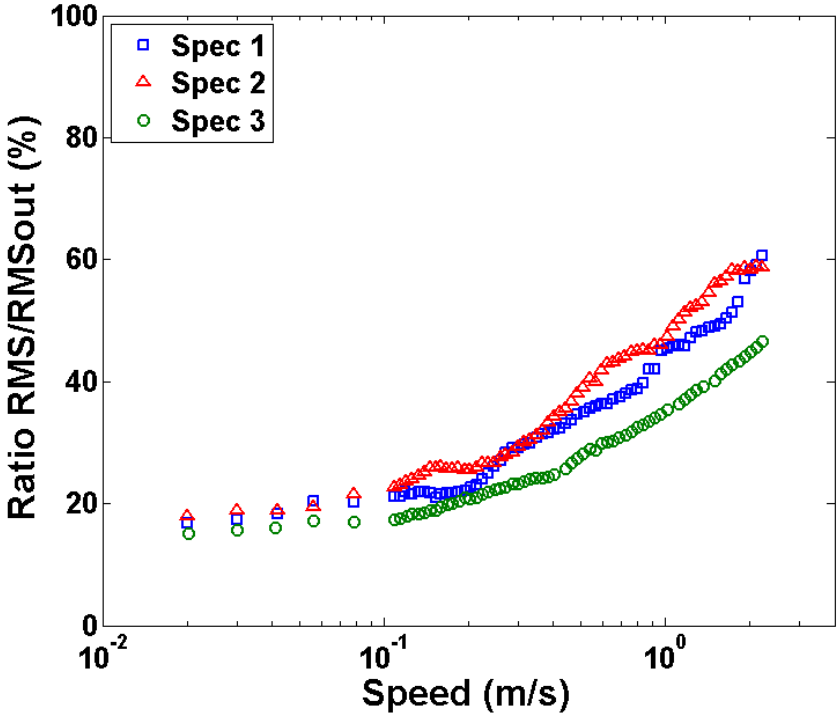


***Figure 6-9:** Variation with entrainment speed of the ratio between the RMS inside the contact and the unloaded RMS*

Lift-off occurs when there is no more solid-to-solid contact. To characterize the speed at which this occurs, it is appropriate to look at the real contact area (solid-to-solid) rather than the minimum film thickness. This is defined as the number of points where the film is zero (or appears negative due to local spacer layer compression). Figure 6-10 shows the evolution with speed of the fractional real area of contact over the area analysed. For each rough surface, the real area of contact falls to zero at a quite well-defined entrainment speed.

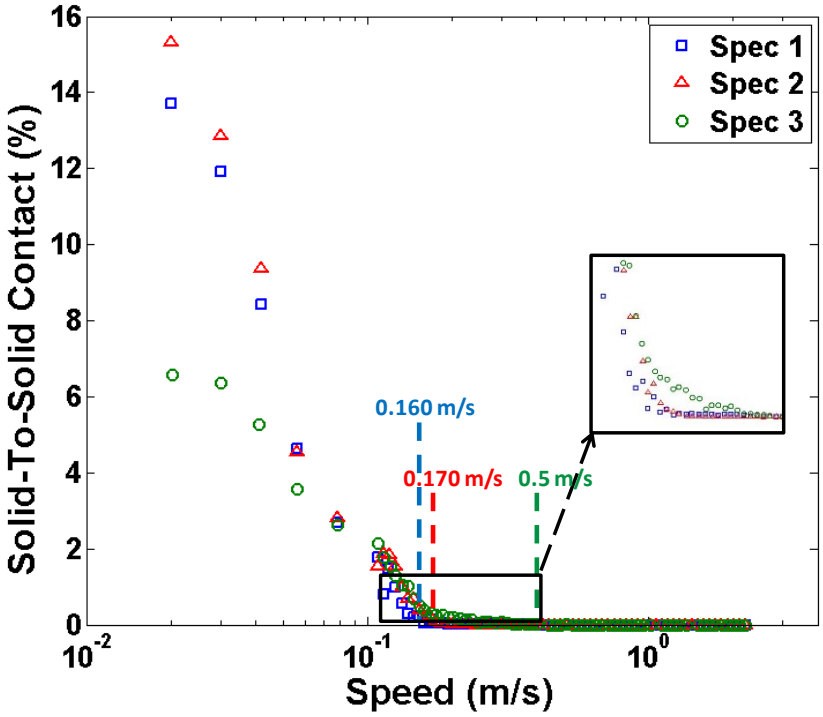


***Figure 6-10**: Evolution of the solid-solid contact with entrainment speed. The respective lift-off speeds are indicated for each specimen, a zoom of the 0 to 1% is also provided*

At low speeds, the rough specimen with the smallest wavelength (specimen 2) has the largest solid-to-solid area of contact. Specimen 1, with the same roughness but a higher wavelength has a slightly smaller area of contact, while the roughest specimen has an even smaller area of contact. As the entrainment speed increases the surfaces start to separate and the solid to solid contact diminishes.

However this diminution evolves at a different rate depending on the specimen considered. As with the film thickness measurements, the two rough specimens with the same RMS show lift-off occurring at about the same speed, between 0.150 and 0.20 m/s, while the roughest specimen lifts off more slowly and there is still solid-to-solid up to 0.50 m/s.

## 6.2. Discussion

It has been shown that the lubricant viscosity does not affect the results qualitatively. For the clarity of the presentation, the following discussion will focus on the results obtained with T68.

### *6.2.1. Film Shape*

As was observed in previous work (Jackson and Cameron [43], Choo, Olver, Spikes, et al. [55]), at low lambda-ratio the roughness dramatically affects the film distribution. For example, at 0.150 m/s, the constriction is well defined in the smooth case but not distinguishable for rough specimen 1. At this low speed, the asperities are apparently very squashed and the conformity of the surfaces (seen on Figure 6-4a) implies that they bear a large part of the load. As the speed increases, the lubricant film increases in the valleys, the roughness starts to recover and the real area of contact is reduced.

At higher speeds (over 0.5 m/s), contrary to what had been observed in other studies (Choo, Olver, Spikes, et al. [55]), a horse-shoe shape becomes visible. This difference from previous work can be explained by the higher speeds reached and the higher viscosity of the lubricant employed in the current study, which leads to much thicker nominal film. It is clear from the interferograms of Figure 6-2 and Figure 6-4b that as the film becomes thicker a constriction appears at the exit of the contact. While micro-EHD features are particularly visible at the top of the ridges, a macro horse-shoe shape can also be seen over the contact as a whole. In Figure 6-4a the transverse film profiles are shown for rough specimen 1 along with the profile of a smooth ball at 1.1 m/s. As the speed increases the asperities partially recover, however the macro-curvature of the surface (*i.e.* when the roughness is ignored) follows closely that of the equivalent smooth case: the ridges in the central area are more compressed (more

flattened) and a film reduction occurs at both edges of the contact (horse-shoe). The rough contact behaves as if the roughness has been added to the smooth case deformation. Thus the deformation seems to be far more influenced by the macro-geometry (i.e. the curvature of the ball) than the roughness.

The rough specimens were also tested in rolling-sliding conditions with a positive SRR equal to 50%. Over the range of conditions tested, the measured film thicknesses were the same, within experimental error, as the ones measured in pure rolling conditions, suggesting that this level of sliding does not have any impact on the film distribution. This is important since it suggests that pure rolling behaviour is representative of that likely to be present in most rolling-bearing contacts where SRRs are generally finite but low. It is also has implications on damage accumulation mechanisms in rough rolling-sliding contacts, such as micro-pitting, as it suggests that any increased asperity interaction at higher sliding speeds is not due to film thickness reduction.

### *6.2.2. Influence of the Roughness Parameters on Film Build-up*

For all of the rough specimens, the minimum film thickness in the central region was significantly thinner than the central film thickness measured with a smooth specimen, as can be seen in Figure 6-6. This can be explained by the gradient of pressure between the ridges and the valleys: at low speed the higher pressure at the ridges forces the lubricant laterally into the valleys, where the pressure is lower. For rough specimens the lift-off (*i.e.* when the surfaces fully separate) occurred at much higher speed than for smooth surfaces. It can be seen on Figure 6-10 that for specimens 1 and 2, it starts at around 0.170 m /s, at which speed the film thickness in the central region is already above 100 nm for the smooth ball. Rough specimens 1 and 2 differ only in the wavelength of their roughness; they have the same RMS

roughness and peak-to-valley height. Figure 6-6 shows that the maximum and minimum film thickness for the two specimens are very similar at all speeds. Specimen 3, which has greater RMS and peak-to-valley height, behaves differently in that the maximum film thickness is higher since valleys are deeper, and the surface separation increases more slowly with increasing entrainment speed. As the real contact area shows in Figure 6-10, some residual contact remains up to a speed of 0.5 m/s. A very interesting result was that average film thickness in the central area was found to be reasonably close to the average film thickness, independent on the roughness considered.

All of the above suggests that the film build-up is only affected by the RMS of the surface and not significantly by the wavelength of the roughness for the range of roughness structures studied here.

### *6.2.3. Roughness Recovery*

Recovery of the roughness can be estimated by the RMS of the separation. It should be noted that the observed RMS is the composite roughness of the contacting surfaces. As the glass disk has much lower elastic modulus than the steel, it can be assumed that the observed reduction in roughness is almost entirely due to the smooth glass surface being deformed as the ridges elastically indent it, rather than the steel asperities flattening. Roughness recovery is then due to the indentations in the glass being reduced as the rough steel surface lifts away from it due to the build-up of film pressure.

At low speeds, the effective roughness is reduced to below 20% of the undeformed roughness. As the speed increases, the roughness partially recovers which shows that a growing part of the load is borne by the lubricant film.

The lift-off speed is the speed at which the load stops being supported in part by solid-to-solid contact and becomes wholly supported by hydrodynamic lift from the lubricant film. Since the contact is in the EHD regime, the surfaces are still elastically deformed when this occurs.

To understand the link between the recovery of the roughness and the lift-off speed, the "real lambda" ratio calculated as the ratio between the average film thickness in the area of analysis and the in-contact RMS, is shown Figure 6-11.

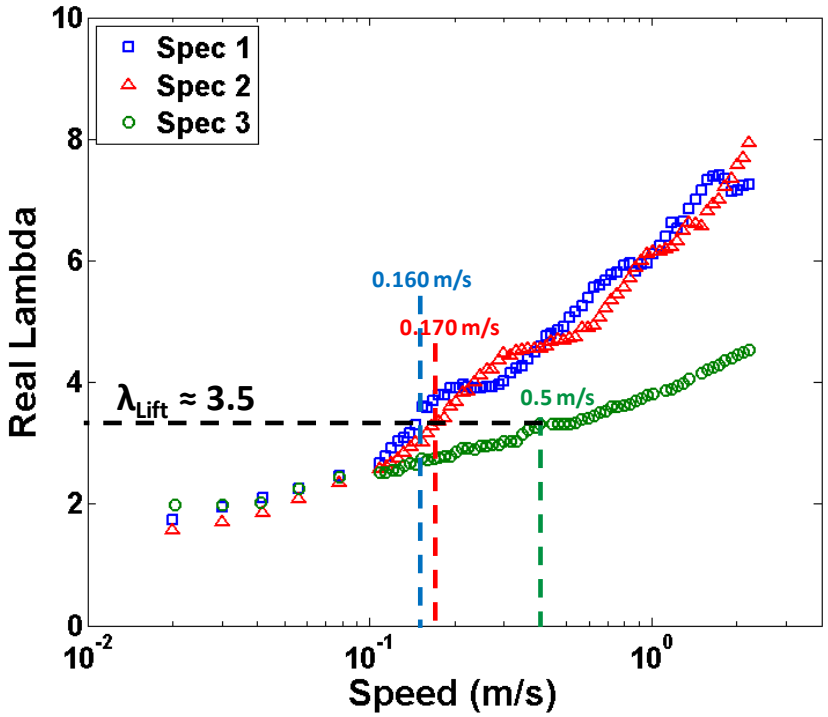


***Figure 6-11:** Evolution with speed of the real Lambda-ratio*

It can be seen that full surface separation occurs at a real lambda ratio $\boldsymbol{\lambda_{Lift} \approx 3.5}$ for all three rough surfaces.

The fact that the surface separation occurs at a given value of the lambda ratio suggests that the transition between the mixed-lubrication and the full film regimes is mostly dominated by a balance between the roughness recovery and the lubricant film-build-up in the contact.

### 6.2.4. Calculated Pressure Distribution

The film thickness maps of specimen 1 were used to estimate the pressure distribution variation with speeds. Figure 6-12a shows a calculated pressure map in the static contact and illustrates the high pressures regions along the ridges. Figure 6-12b compares a pressure profile transverse to the ridge direction in static conditions with the Hertz pressure for a smooth contact at the same load. Also shown in this figure is the corresponding normalised out-of contact roughness profile, (the actual amplitude of the asperities is about 0.5 µm). As expected, peaks of pressure can be observed at the asperity ridges.

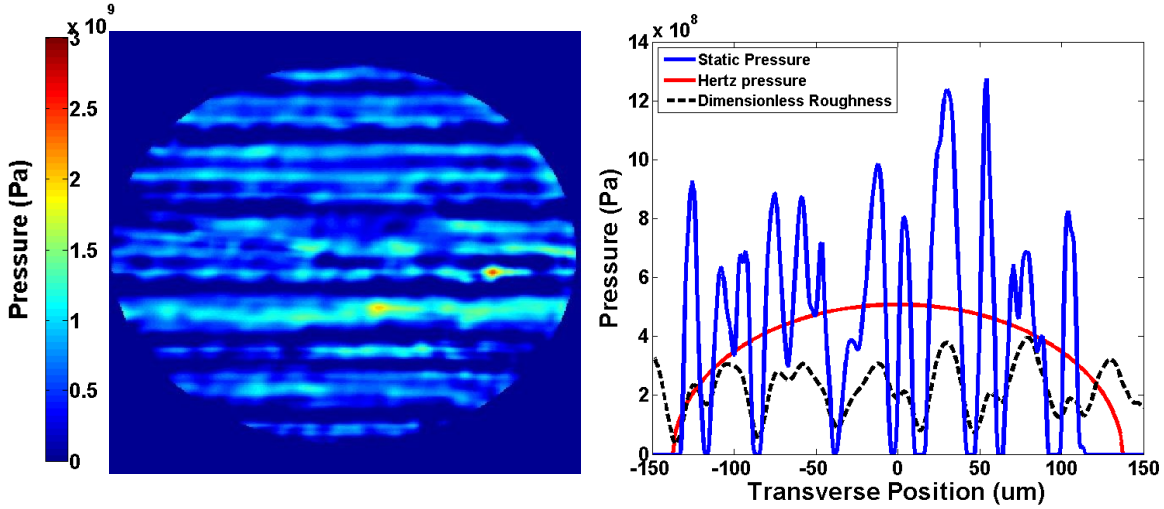


*(a)* *(b)*

***Figure 6-12:** (a) Pressure distribution over the contact (b) Comparison of the contact pressure in static conditions with the Hertz pressure, the roughness profile is also shown*

On average, the pressure distribution seems to follow the Hertz distribution with local variations due to the presence of roughness. The highest pressure is observed in the centre of the contact and the pressure drops in the outer parts. Figure 6-13b shows how the pressure evolves when the entrainment speed increases and the pressure builds-up.

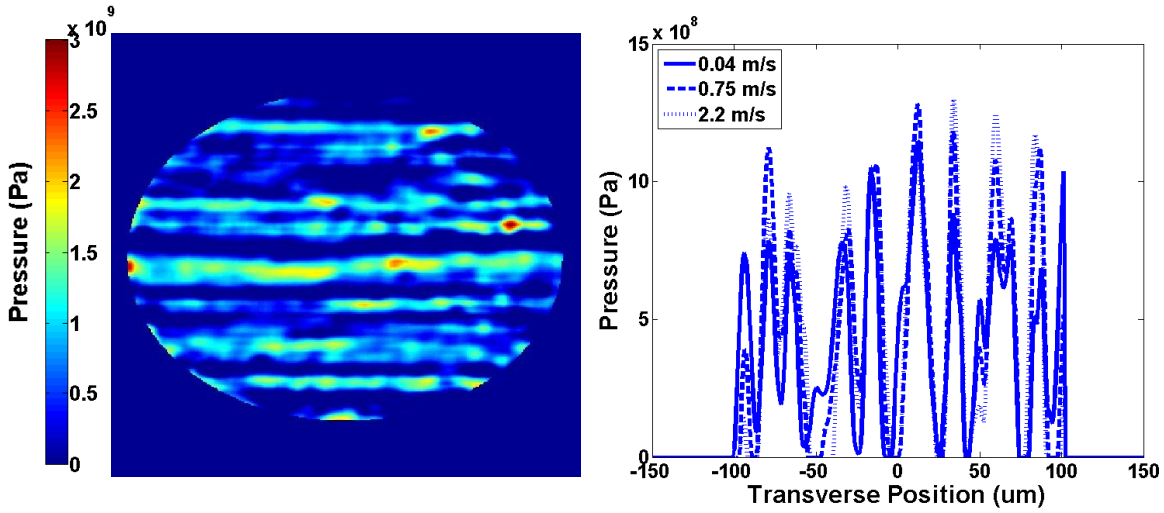


*(a)* *(b)*

***Figure 6-13:*** ***(a) Pressure distribution at 2.2 m/s, (b) Evolution with speed of the pressure profile***

As the speed increase, the surfaces separate and they become less conformal. In the central area, this has the effect of redistributing the load support toward the top of the asperities that see the pressure rise, while it remains low and even diminishes in the valleys. At the outer edges the pressure evolves in the opposite direction creating a low pressure "horse-shoe" that can be seen on Figure 6-13a similar to the one observe in a smooth contact. No pressure peak, known as the Petrusevich peak, could be seen at the exit but this may be due to the smoothing of the surfaces before they were used for the pressure calculations.

To explain the evolution of pressures at the peaks and the valleys an analogy with a smooth contact can be drawn. A smooth specimen was tested using the same lubricant and under the same operating conditions. Similarly to the rough specimen the film maps were used to obtain the pressure distribution at different speeds. On Figure 6-14 the pressure distribution in the transverse direction is shown at three different speeds.

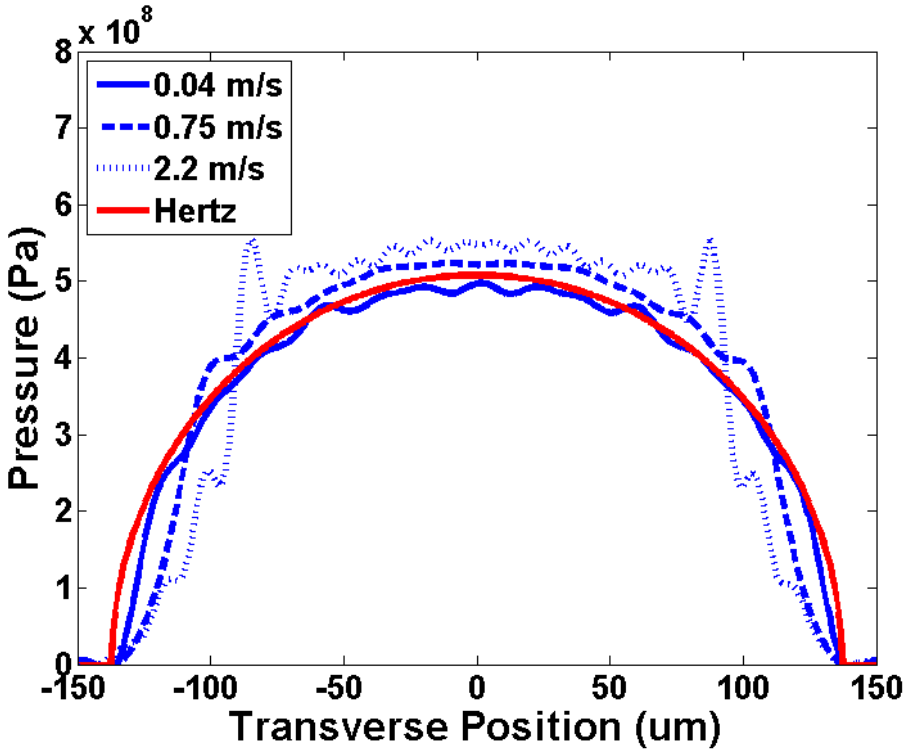


***Figure 6-14:*** ***Evolution with speed of the transverse pressure profile in the smooth case***

As expected, at low speeds the pressure profile is almost Hertzian. As the speed increases, the pressure at the edges decreases, this is due to the formation of the constriction. Interestingly, the pressure in the centre of the contact increases with speeds, as if the loss of load support in the horse-shoe is compensated by an increase of load support in the central area. The reduction of bearing capacity at the sides and exit are accompanied by an increase of the pressure in the inlet. However as mentioned previously, this does not affect the pressure distribution in the contact area. This pressure increase compared to the static case can be seen in other studies (see Molimard et al. [78] and Höhn et al. [74]) although it has not previously been formally identified.

For the rough case, if each ridge is considered as an individual micro-EHD contact, the same phenomenon would imply that as the speed increases, the pressure drops at the edges (*i.e.* the valleys) and increases in the centre of the contact area (*i.e.* the peaks), which is what is observed. The general horse-shoe shape also seems to influence the pressure distribution as

the pressure drop in the valleys located in the outer parts is much more dramatic than for the valleys located in the centre.

### *6.2.5. Difference between Longitudinal and Localised Roughness*

The results shown in this section appear to contradict a number of previous studies that focused on localised roughness such as dents or transverse roughness. First, in these studies sliding was found to have an influence on the film thickness distribution, while such effects were not observed in the current study. For the case of transverse ridges, various authors (Choo et al.[3], Kaneta et al. [1]) have reported that, in the presence of sliding, a perturbation in the oil film was apparent when the ridges entered the contact. Analogous observations were made on dents (see Mourier et al. [50], Krupka and Hartl [117]) or bumps (Choo et al. [14]). Secondly, it has been found in this study that the roughness recovery was primarily influenced by the RMS roughness rather than the wavelength of the texture. Again, this seems to contradict previous theoretical work (Venner and Morales-Espejel [118]) that predicts the contrary.

When considering the influence of roughness on EHD film thickness it is very important to realise that the primary impact of localised roughness features such as dents or transverse ridges occurs in the contact inlet region, where a roughness feature has the effect of momentarily changing the combined radius of the surfaces and thus the rate at which the film gap converges. This causes a transient change in the quantity of lubricant being entrained and thus produces a momentary variation in film thickness. This “blip” or more formally “perturbation” in the film thickness then passes through the contact at the mean speed of the surfaces.

However for longitudinal roughness, where the surface features are elongated precisely along the entrainment direction this does not occur. The ridges and valleys both have almost the same radius along the rolling/sliding direction as does the overall surface, so the system is essentially a steady-state one. In this case, uniquely, the main impact of the roughness occurs within the contact itself and results from the responses of the fluid to the local conditions generated by the varying pressure field therein; for example to the very high pressure along the ridges and to the difference in pressure between the fluid at the ridges and in the valleys. These differences in studied contacts may at least in part explain apparent discrepancies between results shown here and those found by previous studies.

This fundamental difference between longitudinal and all other forms of roughness explains why the results shown are quite different from what has been found by many previous authors.

## 6.3. Conclusion of the Chapter

In this chapter, film thickness results obtained on rough specimens with two different oils are presented. The steel balls had real machined surfaces roughnesses characterized by ridges oriented parallel to the entrainment direction. Film thickness measurements have been conducted under pure rolling and rolling-sliding conditions over a wide speed range such that it is possible to observe the progression from mixed / boundary to full film EHD. Film thickness maps from the central region of the rough contact have been obtained and the film distribution compared to the classic, smooth case equivalent.

The results show:

- Minimum film thickness, observed at the top of the ridges, is much smaller than film thickness in smooth contact.
- The transition from mixed to full film lubrication occurs at higher speeds than for a smooth surface.
- An average film thickness in rough contacts is very similar to the smooth case.

A very large reduction of the effective composite roughness at low entrainment speed is followed by a recovery when the lubricant film starts to build-up.

The three specimens tested were selected to assess the respective influence of the dominant roughness wavelength and the RMS roughness on the development of an EHD film. In the conditions tested, the only parameter that had a significant influence was the RMS roughness of the specimen, which affected the lift-off speed and the minimum film thickness. The influence of sliding on the film build-up was found to be negligible at the sliding speeds considered.

Micro-EHD films were observed to develop at the ridges. With increasing speed, a macro-EHD horse-shoe shape was eventually formed, analogous to that seen with smooth surfaces. It was found that, at the highest speeds studied, the macro-scale deformation of the rough surface matched the deformation observed on a smooth ball at the same conditions.

The maps of film thickness of one specimen were used to calculate the deformation field which was then subject to an inverse solution model to calculate the pressure field. Counter-intuitively the pressure at the peaks increased with speed while it decreases in the valley. This phenomenon was explained by the formation of a micro-EHD film at the top of the ridges.

Finally the surface lift-off, and hence the transition between mixed / lubrication and full EHD regime, was shown to be closely linked to the average film thickness in the contact and the roughness recovery.

Most of the time, bearing raceways are finished using a grinding process. However, the hard-turning process that has been used to produce the rough samples tested in this study appears as a cost effective alternative. In particular, by using this process for the finishing, companies can avoid the need of buying both a turning machine and a grinding machine. Also, hard-turning is a much quicker process than grinding which requires changing grinding disk several times in order to achieve a certain finish.

From the results of this research, a number of recommendations can be drawn up concerning the hard-turning of rolling element bearing's raceways. First, it has been shown that the wavelength of the asperities did not affect the film build-up. As this parameter is in direct proportion of the feed rate of the cutting tools, it means that higher rates could be used in the finish of raceways. This would lead to higher production rate by reducing the duration of the process and also increase the number of raceways that can be finished by one tool since for each process the tool will have to travel a smaller distance. To avoid asperity contact it has been shown that the amplitude of the roughness had to be kept low. This is not always practicable at realistic costs, however the choice of a larger radius for the cutting tools combined with a higher feed-rate tend to lead to lower asperity height which is a cost effective alternative.

The pressure measured at the asperity peaks were shown to far exceed the Hertz pressure. This can have critical practical consequences in the choice of additives such as friction modifiers. As a matter of fact, some friction modifiers act by forming a protective layer at the

top of roughness asperities. In case the pressure is too high, such additives may simply stop being effective because of the harsh conditions. This suggests that, in some cases, a more refined estimation of the pressure could be needed in order to be sure that the lubricant act as required.

# Chapter 7 - Friction Measurements

## 7.1. Smooth Surface Case

Following the methodology described in Chapter 5 -the friction was measured with the two oils, initially using smooth balls (Rq = 20nm). Stribeck curves at various SRRs are displayed on Figure 7-1.

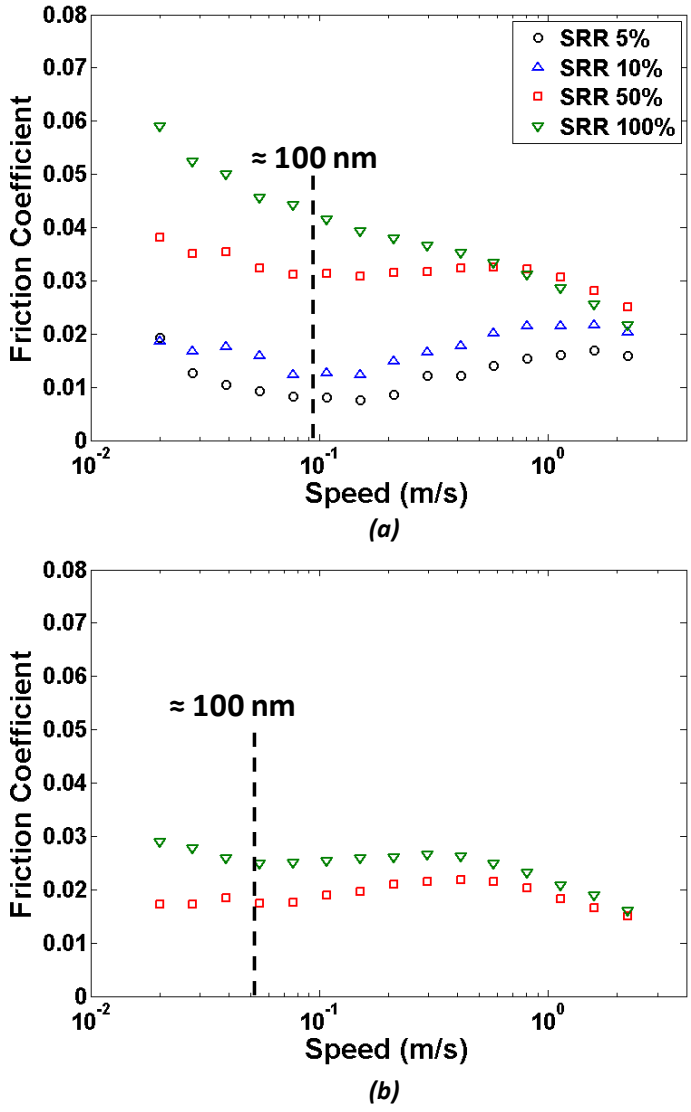


***Figure 7-1:** Stribeck in the Smooth case for various SRRs with (a) T68 and (b) the Group I oil; the oil film thickness at which the transition from mixed to full EHD lubrication is also shown ($P_{mean}$ = 3.5 x $10^8$ Pa, T = 40 °C)*

In addition to the SRRs used for film thickness measurements, Stribeck curves were also measured at **5%** and **10% SRRs** with T68.

For any given entrainment speed tested, the friction was generally found to increase with the SRR. In principle, the friction increases with SRR until it peaks. When the sliding speed becomes high enough, the friction starts decreasing due to the lubricant film heating up, this decreases the effective viscosity thus causing the reduction in friction. Practical rolling bearings generally operate at low SRRs, below this peak. In the current set-up, most of the friction measurements are below the peak because of the low contact pressures. A notable exception can be seen in the T68 curves at the highest entrainment speeds and SRRs (and thus at the highest sliding speeds), where the Stribeck at SRR = 100% falls below the one at SRR = 50%. Another interesting feature is that, for given oil, all the curves seem to converge toward the same curve at high speed.

All the curves start rather high, and then they start decreasing. Apart from the Stribeck curve of T68 at SRR = 100%, they all reach a first minimum at low speeds before the friction starts going up again. The classical explanation is that at low film thickness the contact operates in mixed lubrication where friction results from a combination of fluid friction and boundary friction. When full separation occurs the friction is dominated by the fluid friction and starts increasing again, so that this minimum is usually considered to be the transition from mixed lubrication to full film lubrication. It has been found that in the case of both oils, this occurs at a film thickness of about 100 nm. For a composite RMS roughness of 20 nm, this means that the transition happens at $\boldsymbol{\lambda \approx 5}$. These results are in line with results from previous authors (Evans and Johnson [66], Lafountain et al. [59]). In principle, above $\boldsymbol{\lambda \approx 3}$, there should only be minimal contact, so the transition to full film might be expected there. A hypothesis

made by some other authors (Jefferis and Johnson [68]) is that, even though there is full separation, the traction remains dominated by the local shear rate at the top of asperities where a micro-EHD films forms and the pressure is high. If the pressure is localized, the viscosity of the lubricant will be much higher than that expected if the average or Hertz pressure is considered, which will increase the local viscosity. In addition, the film thickness at the top of asperities will be thinner than the nominal film thickness so the shear rate will be higher. These two phenomena may contribute to make the friction high in this regime even if there is no actual solid-to-solid contact.

Above $\boldsymbol{\lambda > 5}$ it is evident on all curves that the friction does not increase indefinitely with speed, at the highest speeds it starts decreasing again. Lafountain et al. [59] explains this by the fact that at high shear rate the lubricant starts to heat-up, which decreases the viscosity and causes a drop in friction. To prove their hypothesis, they estimated the temperature rise in the contact and used it to obtain “thermally corrected curves”.

An alternative way of plotting the Stribeck curves also due to Lafountain et al. [59] consists in calculating the mean shear rate, from the ratio of the sliding speed and the central film thickness.

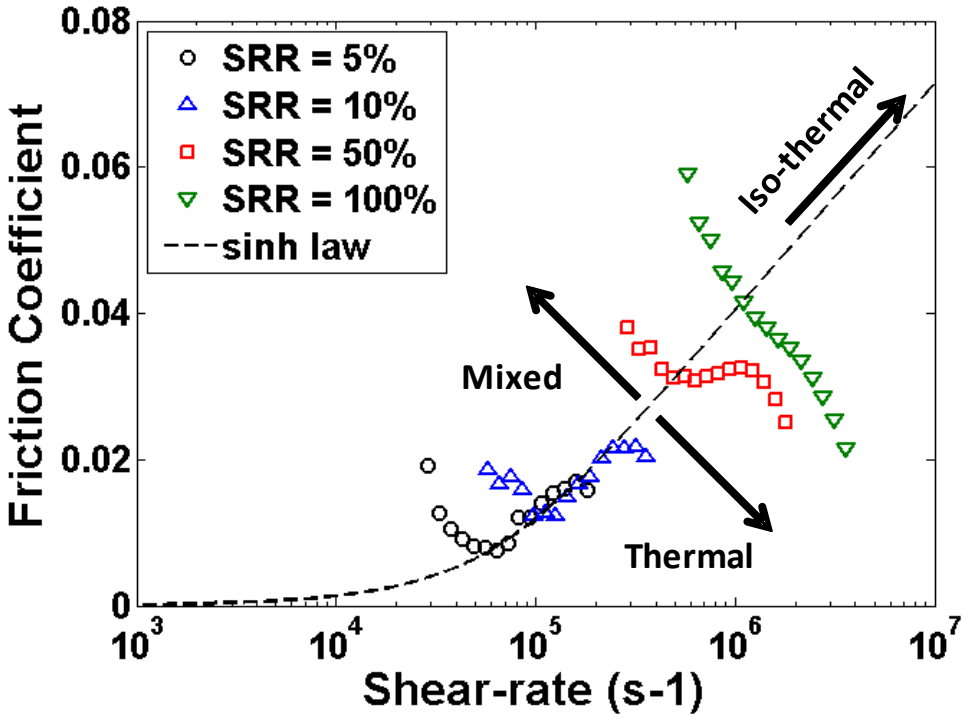


***Figure 7-2:** Friction against shear-rate at different SRRs with T68, the different lubrication regimes are shown along with a sinh curve*

Alongside the friction measurement, a theoretical friction curve using an Eyring rheology model has been plotted on Figure 7-2 (with $\boldsymbol{\alpha = 19.2\ GPa^{-1}}$ and $\boldsymbol{\tau_E = 4.7\ MPa}$). It can be seen that for the low SRRs in full film conditions, the theoretical curve describes relatively well the evolution in friction for $\boldsymbol{\lambda > 5}$. At high SRRs and shear-rates, this curve does not seem model the friction well. A classical explanation is that this drop in friction comes from thermal effects. To test this hypothesis the temperature rise in the contact had to be estimated. This was done using equation (32) taken from Spikes and Jie [64]. It consists in separating the temperature rise into a "mean flash temperature rise" which corresponds to the transient rise in temperature of the surfaces as they cross the contact and a mean oil temperature rise due to shearing:

$$\Delta\bar{T} = \Delta\bar{T}_{surf} + \Delta\bar{T}_{oil} \qquad \textbf{(32)}$$

$$= \frac{1}{(2\pi K\rho c)^{0.5}} \left(\frac{2a}{U}\right)^{0.5} \bar{\tau}\,\Delta U + \frac{h}{8K_{oil}}\,\bar{\tau}\,\Delta U$$

where $K$ and $K_{oil}$ are the respective thermal conductivities of the material and the oil , $\rho$ the density of the material, $c$ its specific heat, $a$ the half width of the contact, $U$ the entrainment speed, $\Delta U$ the sliding speed, $\tau$ the mean shear stress over the contact and $h$ the central film thickness. This formula considers that the two contacting materials are the same, however in this study the ball was in steel and the disk in glass. To calculate the flash temperature rise, the flash temperature was calculated twice, assuming steel / steel and glass / glass contacts. Then, according to Archard [119], the temperature rise can be calculated *via*:

$$\frac{1}{T_{total}} = \frac{1}{T_{steel}} + \frac{1}{T_{glass}} \quad (33)$$

In the range of conditions tested and **SRR = 5%** the temperature rise was found to be negligible, which is consistent with the fact that the friction curve at this SRR follows the Eyring model (see Figure 7-2). At higher SRRs the temperature rise was found to be more significant.

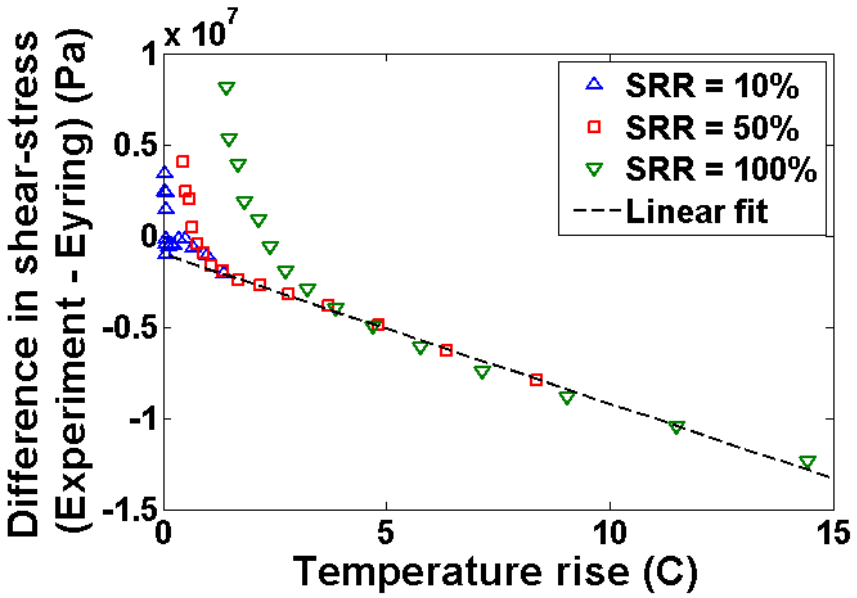


***Figure 7-3:** Difference between measured shear-stress and Eyring model vs. calculated temperature rise*

This rise in temperature will affect the shear-stress a lot. As shown on Figure 7-3, the deviation of the measured friction from the Eyring model evolves linearly with increasing temperature at higher temperature rises, the gradient of this straight line being **-0.83 MPa/°C**. This linear evolution along with the value of the slope is consistent with what Spikes and Zhang [120] showed. Using this gradient and the calculated temperature rise the measured friction data have been thermally corrected. As shown on Figure 7-4 the corrected curves seem to fall very close to the Eyring model, which supports the thermal origin of the drop in friction at high SRRs and shear rates.

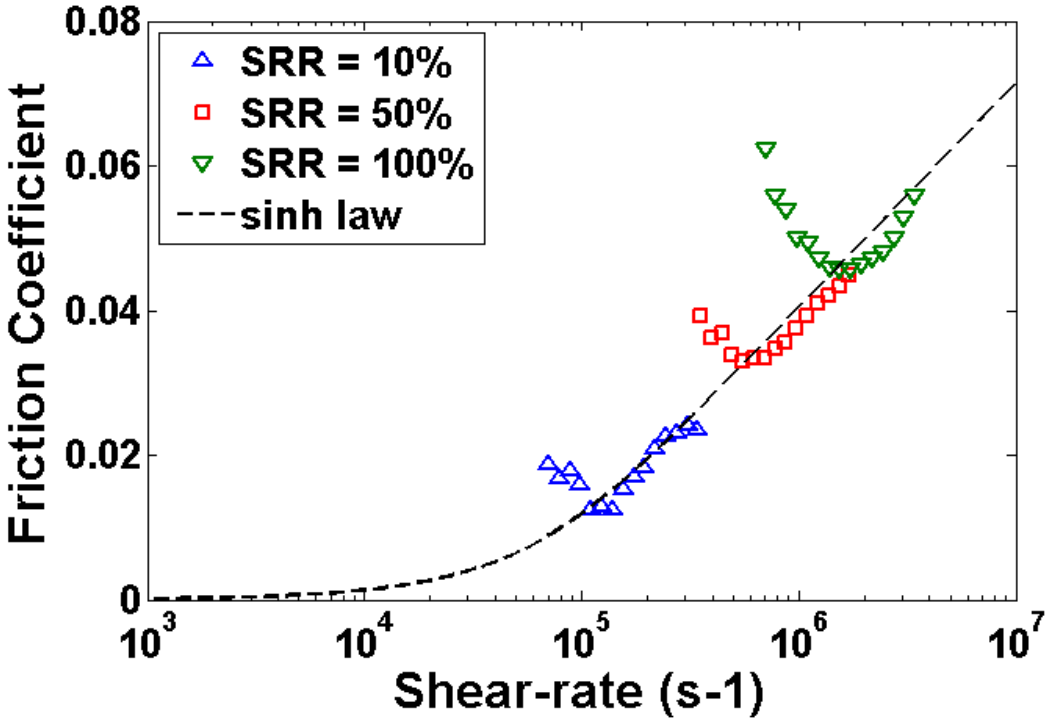


***Figure 7-4:** Thermally corrected friction curves vs. shear-rate; the sinh law is also plotted*

For the Group I oil, the friction *vs.* shear rate relationship is shown on Figure 7-5 with a *sinh* law (with $\alpha$ **= 14.9 GPa$^{-1}$** and $\tau_E$**= 3.0 MPa**). These curves are not thermally-corrected.

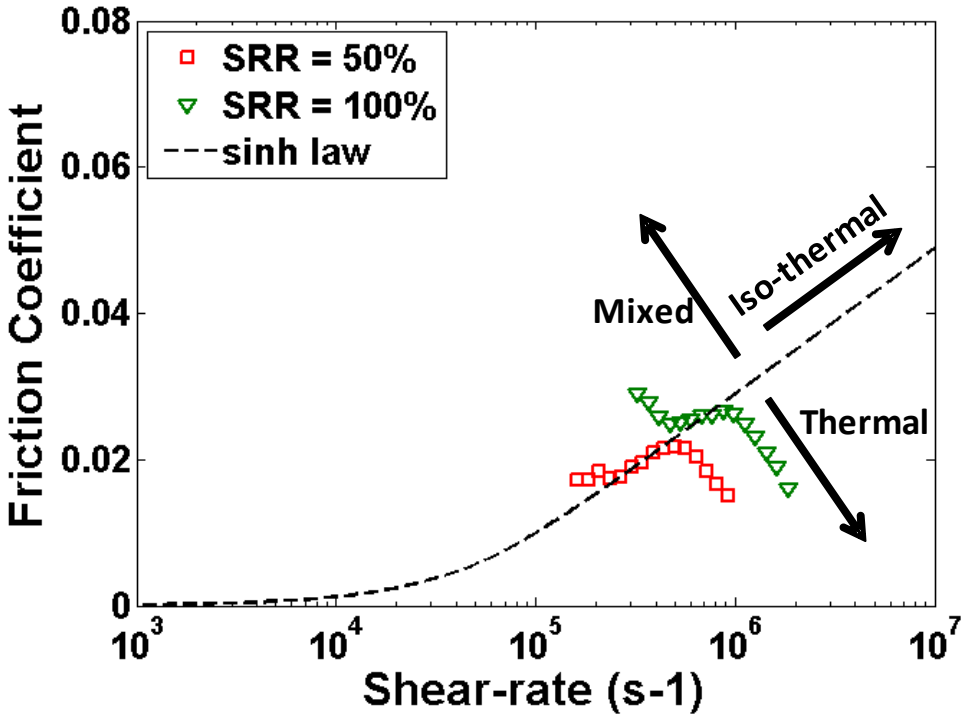


***Figure 7-5:*** ***Friction against shear-rate at different SRRs with the group I oil, the different lubrication regimes are shown along with a sinh curve***

This time, the fit seems to work well up to higher shear-rate, even without thermal correction, for both SRR =50% and SRR =100% when the contact enters full films which can be related to lower shear rates for the same sliding speed as the film is thicker so that the shear heating is moderate compared to T68. It could also be linked to different thermal properties of the two lubricants.

To conclude, most of the curves show similar behaviour:

- When $\boldsymbol{\lambda < 5}$, the contact operates in mixed lubrication, which does not mean that there is necessarily solid-to-solid contact as even in if the contacting surfaces are fully separated the asperities may still influence the pressure and the shear-rate. The micro-EHD film that forms at the asperities may have a decisive influence on the friction.

- For $\boldsymbol{\lambda > 5}$, two behaviours can be observed. Either the friction follows a trend well described by a *sinh* relationship with shear stress (for example) and increases with speed, or the friction decreases with speed. It has been shown that the latter case is linked to higher sliding speeds and/or higher shear-rates and is probably due to shear heating.
- The results on T68 at **SRR = 100%** suggest that if the sliding speed is high it is possible to observe a contact completely dominated by thermal effects for the speeds tested in this study.

## 7.2. Rough Surface Case

### *7.2.1. Results*

Friction measurements were carried out on rough balls under the same operating conditions as used on the smooth specimens.

The Stribeck curves measured in the case of a smooth and the three rough specimens for T68 and the group I oil are shown respectively in Figure 7-6a and b and Figure 7-7a and b. It can be noted that at low speeds, the rough specimens systematically generate a higher friction compared to the smooth specimen. In most cases, as the speed increase and the film builds up, the friction starts decreasing down to the point where it coincides with the friction of the smooth specimen. The latter can be interpreted as the fact that the lubricant provides full separation between the surfaces so that the roughness does not affect the friction any more. In some measurements, (specimen 1 with T68 and specimen 2 with the Group base oil), a slight difference in friction remains at high speed. It is believed that this comes either from experimental error or some drift in the offset.

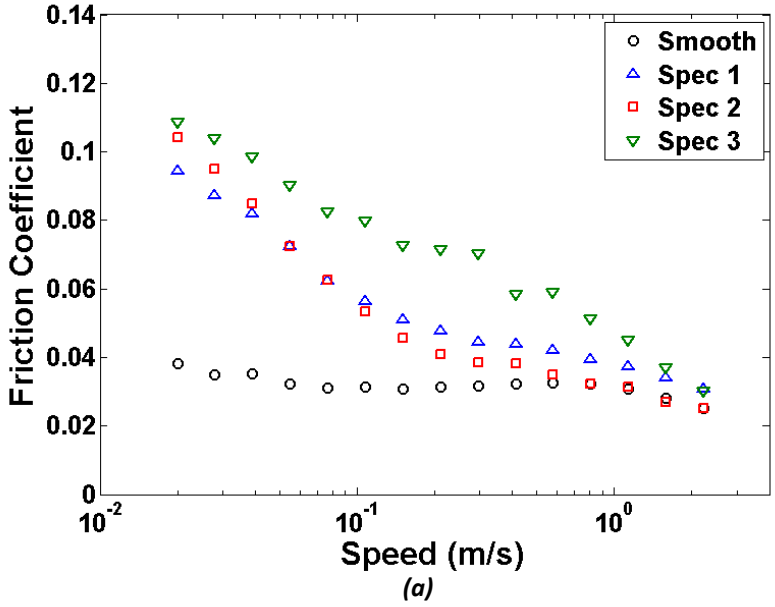


*(a)*

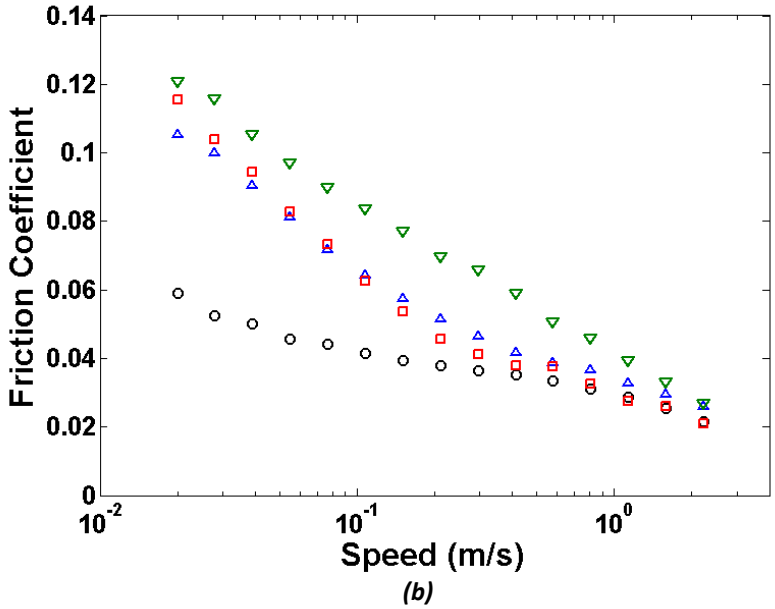


*(b)*

***Figure 7-6**: Comparison of the Stribeck curves for smooth and rough specimens, with T68 (a) at SRR = 50% and (b) SRR = 100%*

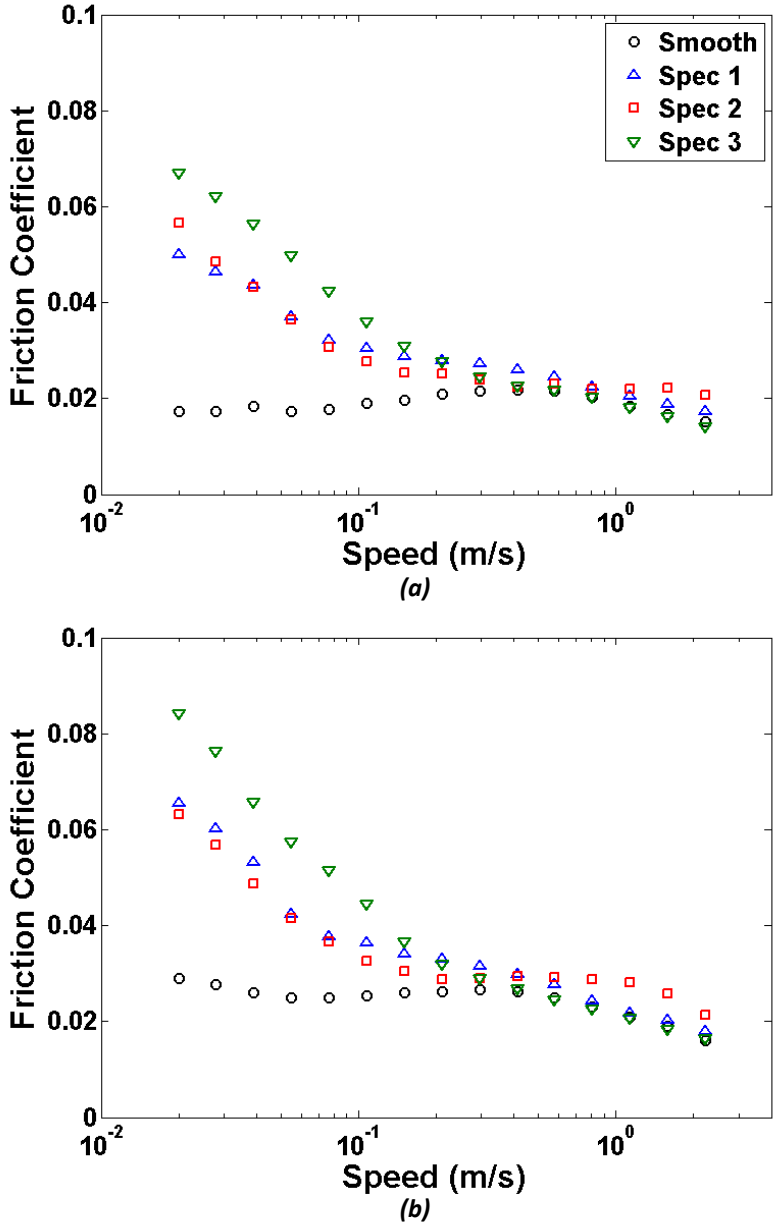


***Figure 7-7:** Comparison of the Stribeck curves for smooth and rough specimens, with the Group I oil (a) at SRR = 50% and (b) SRR = 100%*

Specimens 1 and 2, that have different wavelengths but the same peak-to-valley height, produce very similar friction in all conditions. The peak-to-valley height has much more influence as the friction measured with specimen 3 was significantly higher than the other specimens.

As expected, a higher SRR gives a higher friction.

The results obtained with the two oils follow similar trends. The only differences are in the level of friction and the transition speed at which the rough surface friction becomes coincidental with the smooth surface friction. This latter point can be explained by the fact that the more viscous Group I base oil generates a thicker film so that the transition to full EHD lubrication occurs at lower speed.

In order to quantify the increase of friction directly due specifically to the roughness, the difference in friction coefficient between the smooth values and the rough values is plotted in Figure 7-8.

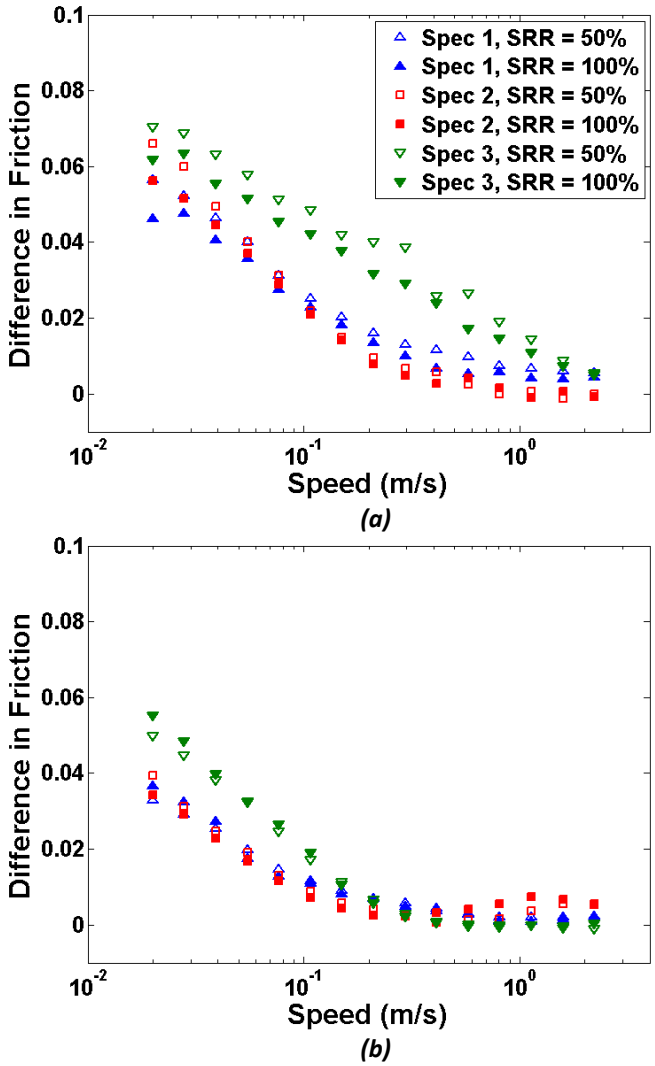


***Figure 7-8:*** ***Difference in friction coefficient between the smooth case and the rough case with (a) T68 and (b) the Group I base oil***

It can be seen that the increase in friction due to the roughness is independent of the SRR. This distinction between "smooth" and "rough" surface friction is different from the usual separation between "fluid" and "boundary" friction (see for example Lu et al. [121]), it just expresses how the difference in pressure distribution and shear rate due to the roughness affects the friction. It is interesting because in both the rough and smooth surface cases, the results of the previous chapter show that the average pressure and shear rate are the same, hence "smooth" surface friction ought to be interpreted as the "average" case.

### *7.2.2. Influence of the SRR*

Like in the smooth case, a higher SRR results in a higher friction. In the rough case, the friction is also affected by the SRR, however when the "smooth" part of the friction is subtracted from the friction, as shown on Figure 7-8, there is no more difference between the measurements taken at different SRR. If $\mathbf{F_{50}}$, $\mathbf{F_{100}}$, $\mathbf{S_{50}}$ and $\mathbf{S_{100}}$ are the friction produced at a **SRR = 50%** and a **SRR = 100%** for respectively a rough and a smooth specimen at the same speed and loads, then there is the following relationship:

$$F_{50} - S_{50} = F_{100} - S_{100} \quad \textbf{(34)}$$

$$=> S_{100} - S_{50} = F_{100} - F_{50}$$

Another way of looking at these results is that the increase in friction due to a higher SRR will be the same whether the surface is rough or not. Hence the friction can be split in a "smooth" component that will vary with the SRR and a rough component that is independent of it. In order to validate this observation, additional tests were carried-out at **SRR = 5%** and **10%**. It can be seen on Figure 7-9 that for a wide range of SRRs the difference in friction between the rough and smooth cases remains only dependent on the entrainment speed and that the sliding has no effect.

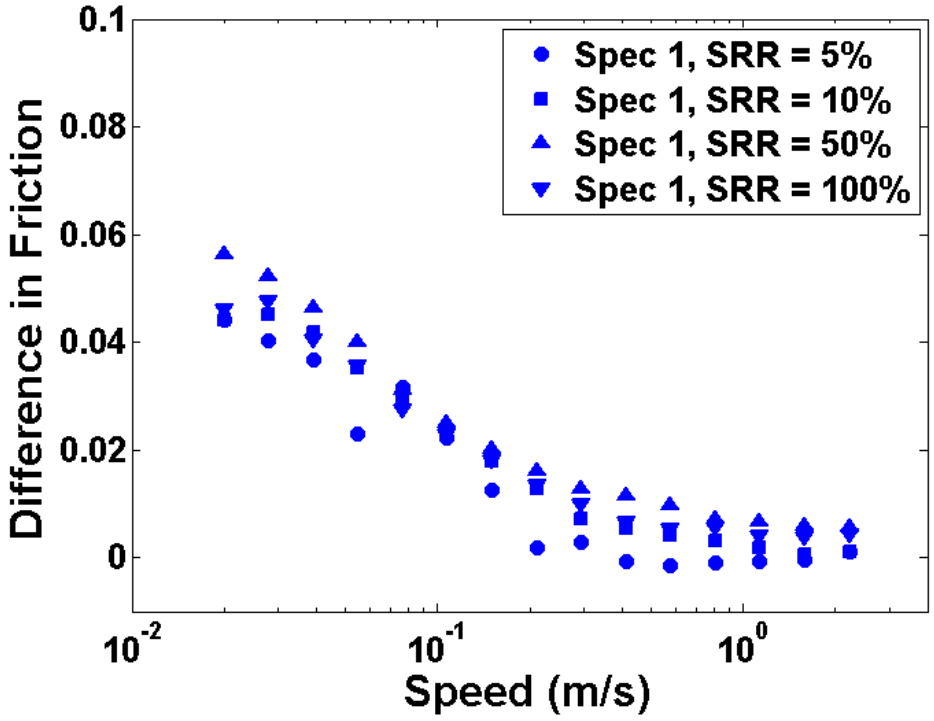


***Figure 7-9:** Influence of the SRR on the difference in friction between the specimen 1 and a smooth specimen*

The independence on SRR of the rough component is obvious if it is originates solid-to-solid contact, in which case the local friction coefficient will be the boundary friction coefficient. Given the high pressures measured at the asperity peaks; another explanation for the independence on the SRR of the rough component could be that the fluid locally reaches a limiting shear-stress at asperity near-conjunctions.

In the case of the smooth component, it was shown in the previous chapter that with rough specimens, the film thickness varied around a central line that was well represented by the smooth case at the same entrainment speed. This difference in film thickness distribution gives rise to a shear rate distribution in which the shear rate is a maximum at the asperity peaks where the film thickness is much thinner and a minimum in the valleys. However, as the average film thickness is the same. Similarly, the pressure was found to be highly concentrated at the asperity peak and much lower in the valleys but pressure distribution varied around the smooth case. The smooth component of the friction seems to be affected

by these average values of the shear-rate and the pressure distribution rather than the local variations. In particular it was shown in the previous section that thermal effects had to be taken into account in order to explain the evolution of the smooth component of friction. As the increase of friction due to the roughness is independent on the SRR, it can be deduced that the thermal effect smooth and rough surfaces similarly. This validates experimentally the work by Johnson and Greenwood [122] who showed that a mean temperature approach can be used to estimate the temperature rise in an EHD contact.

### *7.2.3. Influence of the Roughness Parameters*

In a very similar fashion to what was observed in the film thickness measurement, the wavelength of the specimen was not found to have any influence on the friction measured.

Regarding the effect of the peak-to-valley height or RMS roughness, the lambda ratios can be compared. This can be done as the EHD film thickness was measured for all the surfaces under the same test conditions. The lambda ratio is defined as:

$$\lambda = \frac{h_{AVG}}{RMS} \tag{35}$$

where $h_{AVG}$ is the measured average film thickness as explained in the previous chapter and ***RMS*** is the composite roughness of the contacting surfaces. Given that the disk is very smooth (RMS ≈ 5 nm) the composite RMS will be dominated by the RMS roughness of the ball. The values used for the ***RMS*** of the rough specimens are the ones listed in Table 2, where both specimens 1 and 2 have an RMS of 150 nm, and specimen 3 has an RMS of 270 nm and the smooth specimen an RMS roughness of 20 nm.

The Stribeck curves previously measured are plotted against the lambda ratio in Figure 7-10a and b for T68 and Figure 7-11a and b for the Group I oil.

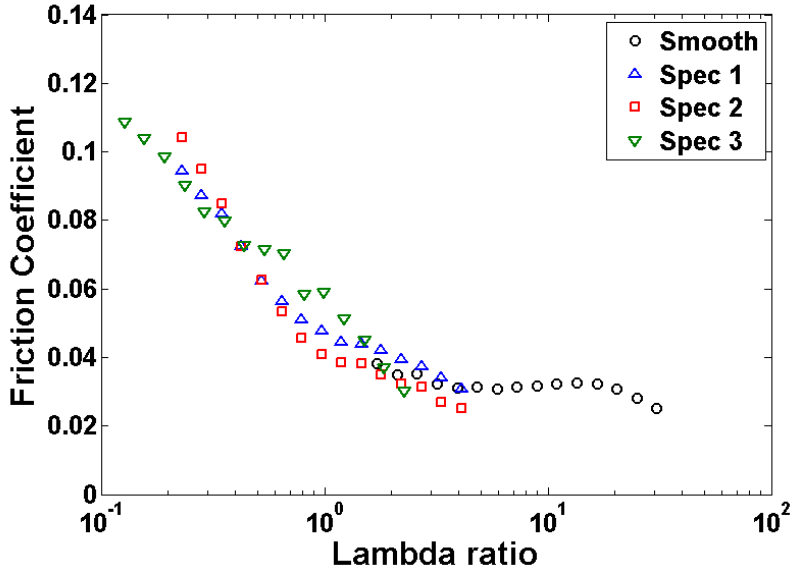


*(a)*

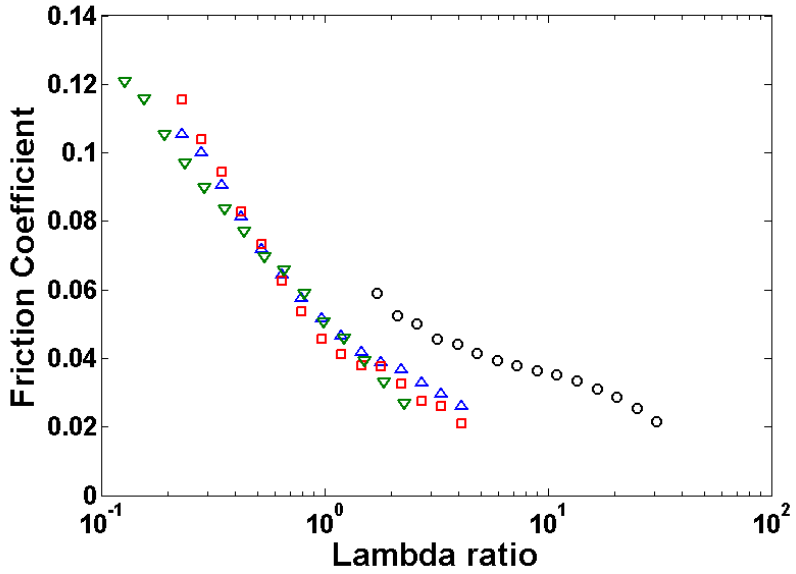


*(b)*

***Figure 7-10**: Friction against lambda ratio for with T68 (a) at SRR = 50% and (b) SRR = 100%*

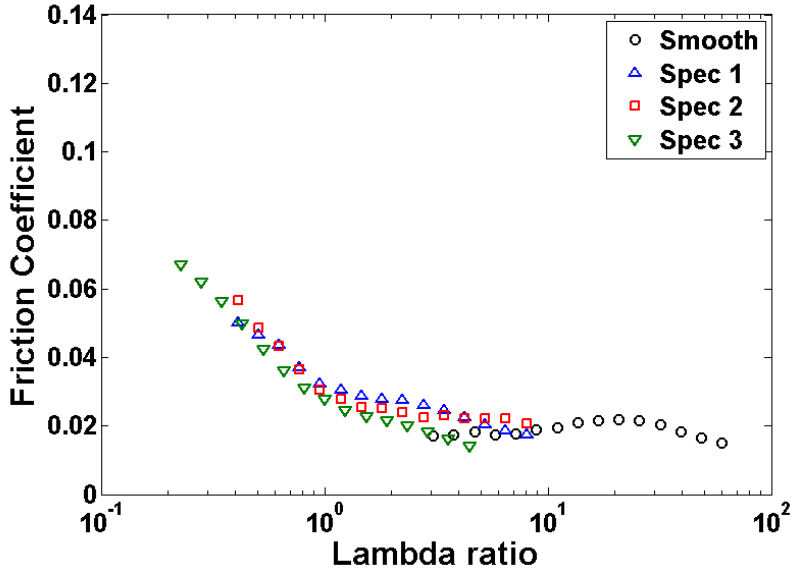


*(a)*

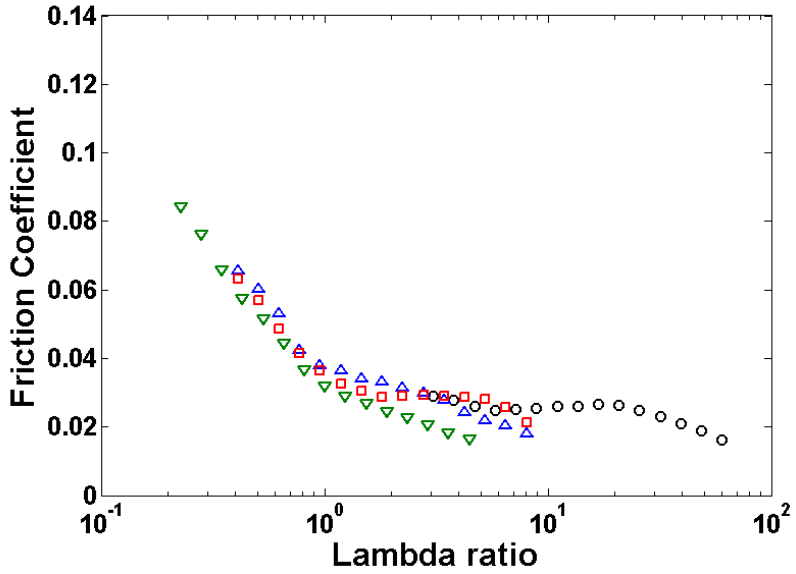


*(b)*

***Figure 7-11:** Friction against lambda ratio for with the Group I oil (a) at SRR = 50% and (b) SRR = 100%*

In each graph, there seems to be continuity between the different Stribeck curves measured with different roughness and the smooth case except for Figure 7-10b in which the smooth case does not lie on the same curve as the rough cases. However if an RMS of 30 nm is considered for the smooth case, the smooth curve coincides with the other Stribeck curves. In practice this increase in the RMS roughness could come from some scratches on the disk coating that will change the composite roughness. As the composite RMS roughness is

dominated by the roughness of the rougher surface, the lambda ratio in the rough cases would not be affected by such a moderate increase in the disk roughness (for example if it increases from 5 to 20 nm).

It is clear that the roughest specimen generates a higher level of friction than the other specimens, but, as all the Stribeck curves show, this can be solely interpreted as a decrease in lambda ratio and an increase in solid-to-solid contact.

The difference in friction between the rough cases and the smooth case versus lambda ratio is shown on Figure 7-12 for all the specimens and SRR and the two oils.

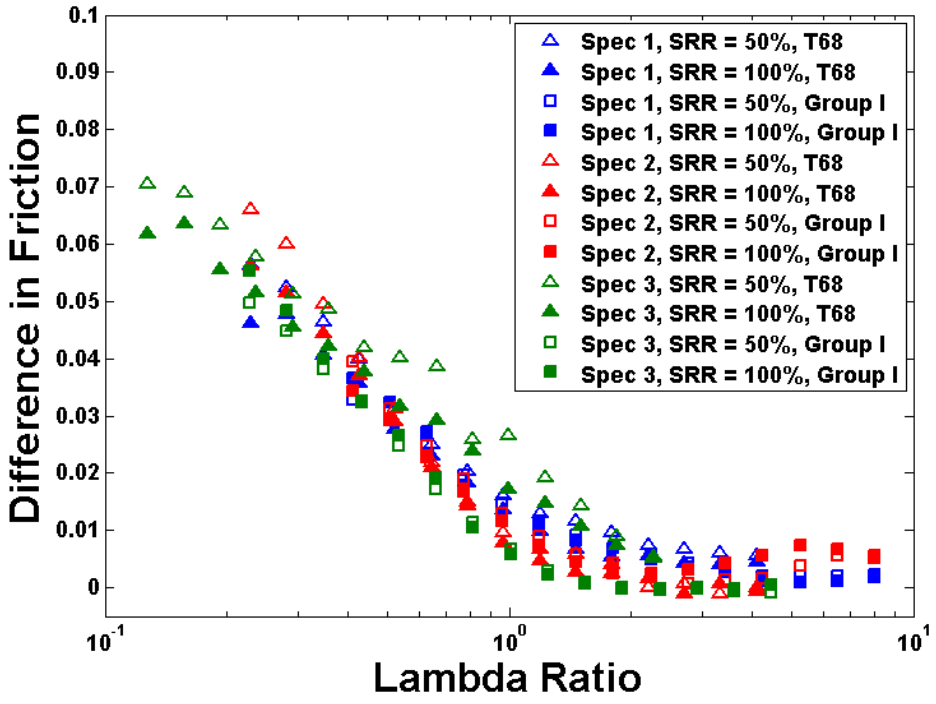


***Figure 7-12:** Difference in friction versus lambda ratio for the three specimens, the two SRRs and the two oils tested*

It can be seen that all the curves appear to belong on the same master curve. This curve shows that the transition from mixed-lubrication to full EHD lubrication occurs at a lambda ratio that is between 2 and 5, which is in accordance with most previous studies (Bair and Winer [65], Evans and Johnson [66]).

The fact that the increase in friction due to the roughness is the same for the two oils also seems to suggest that its origin is asperity contacts. However this may also be fortuitous and the two oils might have a similar limiting shear stress.

### *7.2.4. Relationship with the Minimum Film Thickness*

In order to assess the influence of the roughness on the friction, it is interesting to look at the point where the friction stops being higher than the friction in the smooth case for the same SRR and entrainment speeds, which means that the difference in friction shown in Figure 7-8 becomes 0 (or level out, given there might be experimental errors). As the film thickness was measured at the same time it was also possible to observe directly whether there remained any contact or not at this point.

The evolution with entrainment speed of the difference in rough and smooth frictions was plotted along with the minimum film thickness in Figure 7-13 and Figure 7-14, for respectively T68 and the Group I oil.

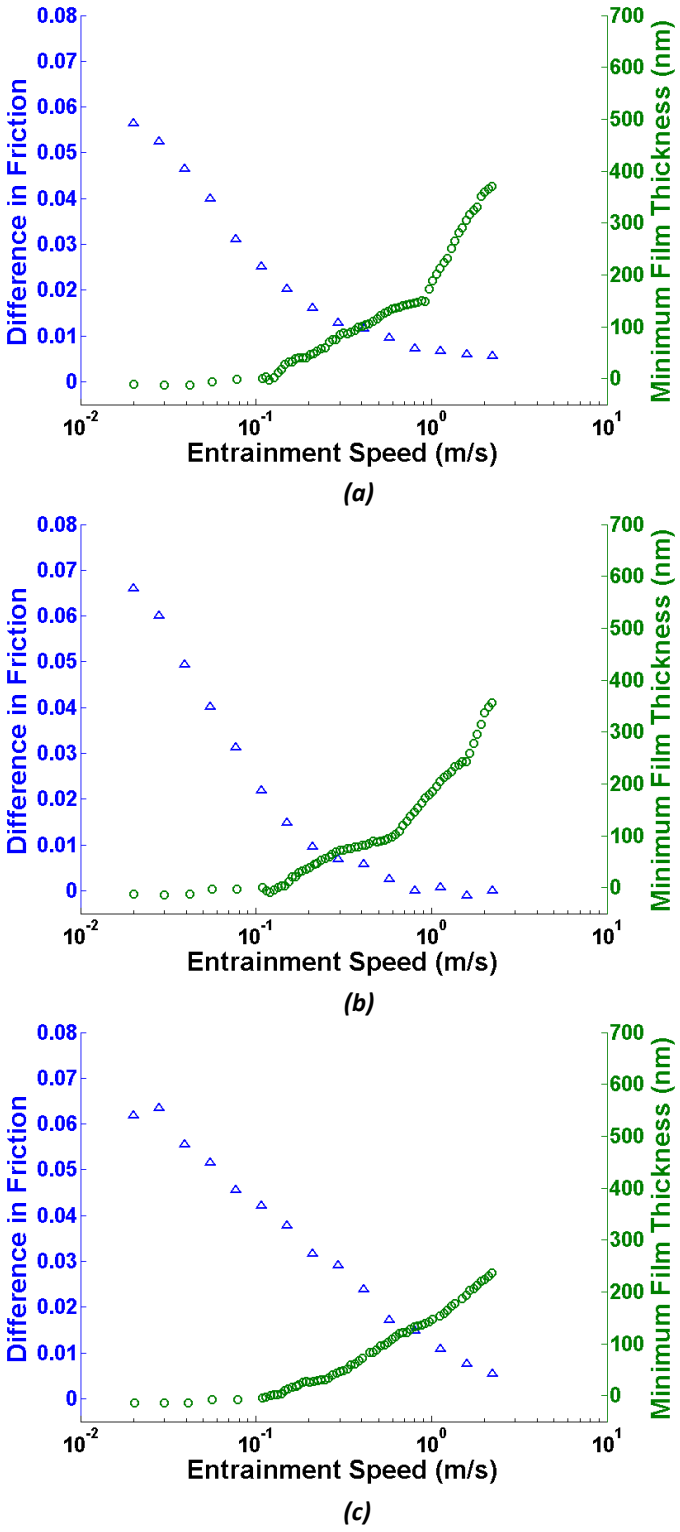


***Figure 7-13:*** *Evolution with the entrainment speed of the difference in friction between rough and smooth frictions and the corresponding minimum film thickness, in the case of T68 for (a) specimen 1, (b) specimen 2 and (c) specimen 3*

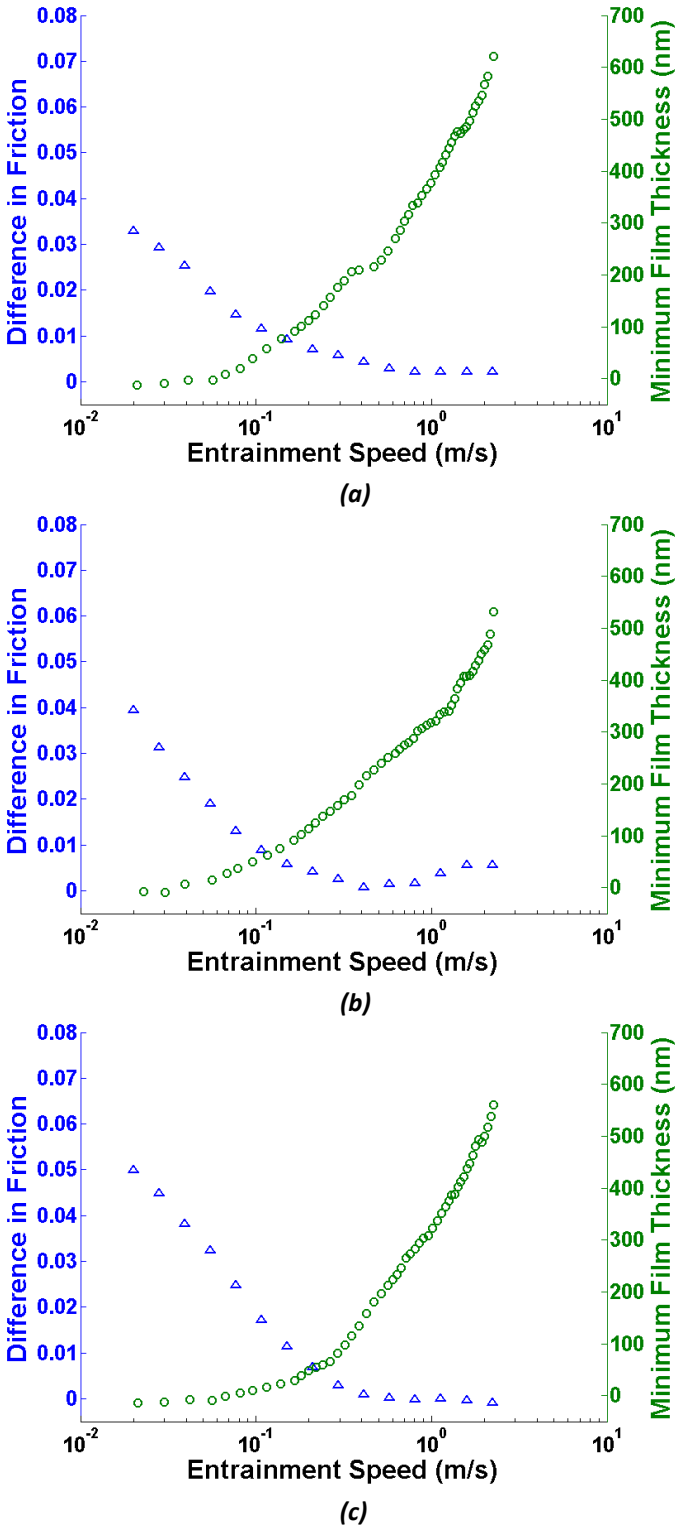


***Figure 7-14:*** ***Evolution with the entrainment speed of the difference in friction between rough and smooth frictions and the corresponding minimum film thickness, in the case of the group I oil for (a) specimen 1, (b) specimen 2 and (c) specimen 3***

As expected, the evolution of the two measurements have opposite trends: the difference in friction is high at low speed and decreases as the lubricant film builds up, until it stabilizes while the minimum film starts flat and increases with speed.

One conventional description of the mixed-lubrication regime consists in separating the friction into a fluid component and a boundary one. The results shown here somewhat contradict this assumption. In every case, after lift-off, the roughness continues to have some influence on the friction, and it is only when the lubricant film separates all the contacting surfaces with a few hundred nanometres that this influence vanishes completely.

Although it is counter-intuitive, this effect could be expected when considered in parallel with the pressure results of the previous chapter. It was shown that as the lubricant film builds up, the pressure is redistributed toward the asperity peaks forming a micro-EHD film. This peak of pressure at the asperity, even in the case of a full lubricant film, can explain the delay between the full-separation of the contacting surfaces and the convergence between rough and smooth friction. The fact that it does not depend on the SRR, as seen in section 7.2.2, suggests that the increase in friction is not only due to solid-to-solid contact but also that the fluid must be reaching a limiting shear-stress.

However, the surface lift-off does seem to affect the rate at which the friction converges toward the smooth friction.

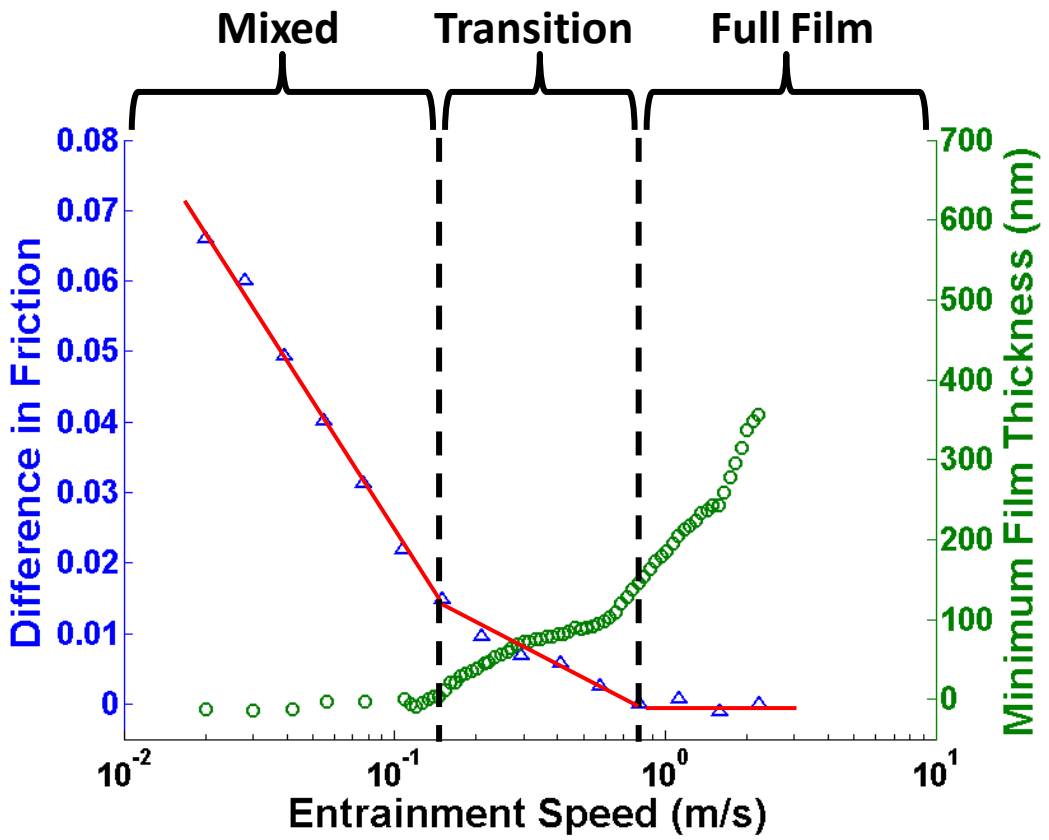


***Figure 7-15:** Reproduction of Figure 7-13b showing the transition between the mixed and the full film regime and how the rate of friction variation is affected*

Another possible explanation for this delay could be that the film thickness is measured only in the central square of the contact, while the friction is averaged over the whole contact. It is possible that greater asperity contact occurs in the region outside the centre, giving higher friction than expected for the measured film thickness.

### *7.2.5. Prediction of Friction*

As previously stated, the full prediction of the friction given the roughness parameters and the oil property does not seem possible within the current state of the discipline. That being said, there have been some formulas proposed to calculate the friction in the mixed regime, knowing the lambda ratio, the boundary friction and the fluid friction. In particular, Olver and Spikes [102] suggested the equation:

$$\mu = \mu_f + \frac{\mu_b - \mu_f}{(1+\lambda)^m} \quad (36)$$

where $\boldsymbol{\mu}$ is the coefficient of friction, $\boldsymbol{\mu_f}$ the fluid friction and $\boldsymbol{\mu_b}$ the boundary friction, λ the lambda ratio and m, though they do not explain the derivation of this. According to the authors, m should be around two. In our experiments, we found that the best results were obtained for m between 2 and 3 and $\boldsymbol{\mu_b}$ **= 0.14** which is a reasonable value for a steel on glass contact.

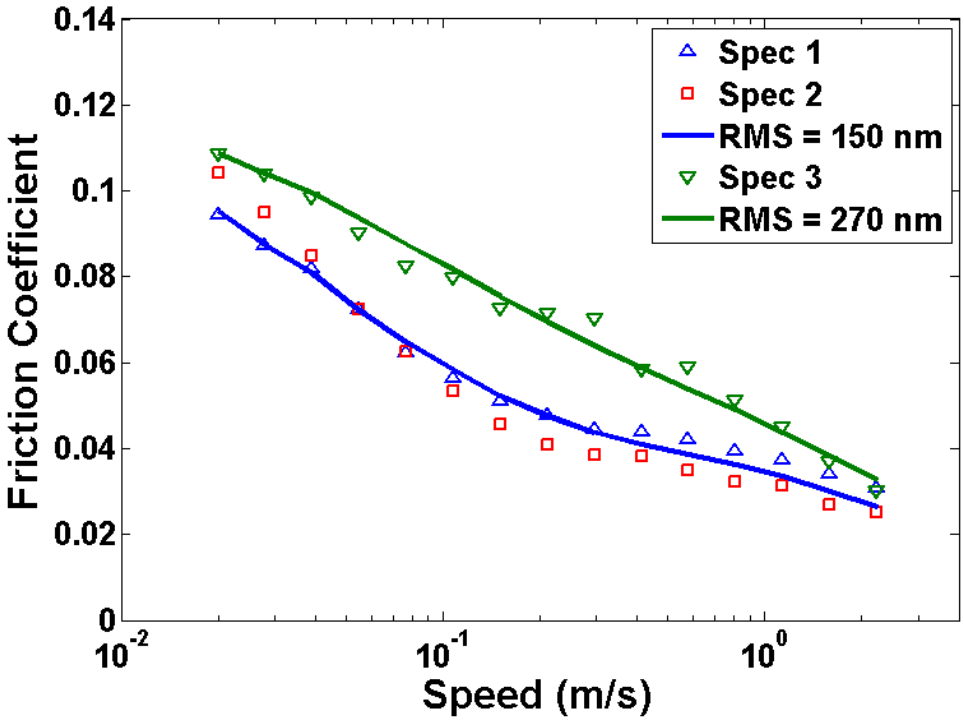


***Figure 7-16:** Stribeck curves at 50% with T68 showing the prediction from equation (36)*

Figure 7-16 compares measurements with the predictions of Eq. 36 where the predictions are shown as solid lines. It can be seen that fits are quite good, especially as they seem to predict non-trivial characteristics of the curves, such as the concavity of the higher RMS Stribeck curve and the convexity of the lower RMS ones.

## 7.3. Conclusion of the Chapter

This chapter focused on the effect on friction of the same rough ball specimens whose lubricant film thicknesses had been measured in chapter 6. First the smooth case was addressed for the two test oils. The two oils showed analogous behaviours:

- For $\boldsymbol{\lambda < 5}$, the friction started high and decreased with rising entrainment speed and film build-up, this was interpreted as the contact operate under mixed-lubrication and moving from boundary lubrication towards EHD lubrication.
- For $\boldsymbol{\lambda > 5}$, the friction followed the friction predicted by the Eyring model but started deviating from it at higher shear rates. This was well explained by the shear heating of the lubricant that decreases the effective viscosity and so the friction.
- For a same entrainment speed range, the friction was found to increase with the applied SRR which was explained by the relatively low pressures inside the contact

The friction produced by the same specimens whose film thickness measurements had been presented in chapter 6 was measured under the same operating conditions. Results show:

- The rough specimens generate more friction than the smooth one in the same conditions. This is related to lower minimum film thickness and higher pressure at the asperity peaks.
- Similarly to the film thickness build-up, the friction was not affected by the wavelength of the specimens but was strongly dependent on the peak-to-valley height
- When the film thickness becomes sufficiently thick, the friction tends toward the friction produced at the same speed by a smooth specimen. The effect of the roughness vanishes when the film is thick enough.

- It was found that the friction could be separated into a “smooth” component equal to the friction produced by a smooth specimen under the same operating conditions, and a “rough” component. This rough component is independent of the SRR which suggests either some extra solid-to-solid contact or that the lubricant at the asperities reaches a limiting shear stress or both.
- The friction convergence toward the smooth case was shown to occur after the lift-off of the surface, which support the second hypothesis above
- A very simple equation using only one parameter and the boundary friction value was found to predict quite well the friction observed with rough specimen

The effect of the wavelength and roughness of the surface on the friction were found to be analogous to that on the film thickness, hence the recommendations for machining process suggested at the end of the previous chapter remain valid. It has also been found that the ubiquitous use of the lambda ratio is justified even when the surfaces are complex. In particular, the friction generated by a rough surface can be estimated by knowing its lambda ratio and the friction produced by a smooth surface. For a particular industrial application, it becomes possible to estimate the friction of a rough component by performing a cheap friction test on a smooth specimen (or use existing data) in similar operating conditions. The lambda ratio can then easily be optimized in order to minimize the production cost while respecting the friction loss targets.

# Chapter 8 - Conclusions and Future Work

## 8.1. Conclusions

The aim of this research was to investigate the effect of longitudinal roughness on the film thickness build-up and friction in non-conformal contact. These types of contact are typical of applications such as rolling bearings or gears. Additionally, in real applications the contacting surfaces are never perfectly smooth but show some roughness features that appear during the manufacturing process. When oriented along the rolling-sliding direction these roughnesses are very similar to what can be seen on rolling element some bearing raceways. This study focuses on an experimental investigation of this particular type of roughnesses. To do so, steel ball specimens with parallel ridges were prepared using a hard-turning process. This process enabled production of roughnesses that were characterized by a dominant amplitude and wavelength. Several specimens were produced with a range of these two parameters.

The tests were all carried-out on a ball-on-disk rig in which a non-conformal contact is produced between a steel ball and a glass disk and which enables the simultaneous measurement of the film thickness and the friction.

A technique based on optical interferometry was chosen to measure the film thickness as it was found to be the most accurate within the range of film thickness studied. To enable the study rough surfaces, the original test rig set-up had to be modified. First, a duo-chromatic system using a green and a red LED was designed in order to extend greatly the range of film thickness that could be measured. This new illumination system was coupled with a triggering

system based on the ball position. This made it possible to identify a particular rough region on the ball at the beginning of the test and then trigger the camera at exactly the same spot so that the film thickness build-up could be observed in the same location as the speed increased. A novel procedure for the post-processing of the interferograms was developed and it was shown that this could help the conversion of complex interferograms, as obtained with rough surfaces, into very accurate film thickness maps.

Tests were carried over a range of entrainment speeds that enabled the contact to be studied from boundary, through mixed to full film conditions. The effect of sliding was also investigated. The film thickness measurements showed:

- At low speeds the roughness ridges were elastically flattened when they entered the loaded area reducing the effective RMS roughness. As the speed increased and the lubricant film built-up, the lubricant filled up the valleys, allowing the original roughness to partially recover.
- Micro-EHD films were observed at the top of the asperities and at higher speeds a macro horse-shoe shaped film formed, similar to that observed in smooth surfaces.
- The effect of roughness on the film thickness could be seen as fluctuation of the film thickness around a central line average, which was close to being the smooth film thickness observed in the same conditions. Consequently, in all the specimens tested, the average film thickness in the central area of the contact was very close to the smooth film thickness. The fluctuations thus implied that the minimum film thickness at the top of asperities was much thinner while the maximum was much thicker than in the smooth case. The minimum and maximum film thickness depended on the RMS roughness of the surface but not on the wavelength.

- The lift-off the surface, *i.e* when the surfaces separate completely, was found to occur at higher speed than the smooth case. This speed varied with the RMS roughness of the specimen tested but not with the wavelength.
- In the loaded area, an important reduction of the composite roughness was observed. As the film built-up, the roughness was found to recover significantly, but at different rates depending on the undeformed RMS roughness of the specimen. Specimen with similar RMS roughness but different wavelengths recovered at the same rate.
- No effect of sliding could be observed on the film thickness build-up, which was the same in rolling-sliding as in nominally pure rolling.

With accurate film thickness maps of the entire contacting area, the deformation field could be calculated and then used to estimate the pressure distribution in a rough EHD contact. An important concentration of pressure at the top of the asperities was observed. The pressure peaks were found to increase with speed. This was linked to the recovery of the roughness ridges that redistributed the pressure toward the peaks, which eventually led to the development of micro-EHD films previously mentioned.

In parallel to the film thickness measurements the friction was also measured. The results correlated very well with the film thickness and pressure measurements:

- All the rough specimens generated more friction than the smooth case except at very high speeds; this was well explained by a lower lambda ratio. At very high speeds and film thickness the influence of the roughness vanished and the friction was equal to the smooth surface friction.
- Similarly to the film thickness measurement, the friction was influence by the RMS roughness of the specimen but not by its wavelength

- The friction could be split into a “smooth” component equal to the friction measured in the same condition with a smooth specimen and a “rough” component that was found to be independent of the SRR. This suggests that the increase of friction is either due to more solid-to-solid contact or the existence of a limiting shear stress.
- The friction was compared to the minimum film thickness. A delay between the surface lift-off and the convergence of the friction toward the smooth surface friction was observed, which means that the roughness continues to influence the friction even though there is no solid-to-solid contact. This is in strong agreement with the film thickness and pressure measurements that showed a micro-EHD film forming and peaks of pressure significantly above the Hertz pressure at the top of the asperities.
- The film thickness measurements and the friction are definitely linked and a model was shown to give reasonable prediction of the friction from the knowledge of the lambda ratio

## 8.2. Future Work

Following this work, a number of developments could be made.

First, concerning the technique to measure the film thickness, the limitation of the techniques previously were presented, in particular the problems of uneven illumination and reflectivity. A solution was found, but this technique could be further improved. A few suggestions are as follows.

- Using only one interferogram and an edge detection algorithm to identify the fringes, a normalization procedure similar to the one described in this work could be applied. This would have the advantage of reducing the number of images taken during one

experiment as each image would be treated independently. Applying this technique to a rough surface would probably require higher resolution images so that the continuity of the fringes is ensured.

- Using the above technique, the film thickness could be mapped outside of the contact area (apart from the cavitation zone), as long as the gap stays below the coherence length of the light source
- Some authors distrust optical interferometry-based film thickness measurements because the refractive is pressure dependent. However, as shown by a number of researchers, using pressure measurements from an inverse model it is possible to correct the film thickness measurement by using the relationship between the refractive index and the pressure (Lorentz-Lorentz relationship).
- The lighting could also be improved if lasers were used instead of LEDs and a third blue light was added

Concerning, potential future work on rough surfaces, the double approach of systematically measuring the film thickness and the friction at the same time could be applied to a much larger range of roughness geometries. In particular, the effect of the orientation of parallel ridges could be investigated (perpendicular or oblique), as this is of particular relevance in some practical application (*e.g.* gears). A number of authors have already studied the influence on film thickness of these types of roughnesses but not with the same accuracy or to such high speeds, and the correlation with the friction was never made.

Another type of roughness that is of great interest is the random (isotropic) roughness case. A few studies have already researched this type of roughness but they used surfaces with very low roughness. To obtain these, they took steel balls of lower polishing grades so that they

were naturally rougher. During the current project, a method to produce random roughness was investigated which consisted of using a barrelling machine based on a cylinder filled with abrasive powder and the specimen to be roughened. By rotating the cylinder for hours or days, the powder will slowly scratch the specimen and will generate a very consistent roughness throughout. By varying the particle size and probably other parameters such as their hardness, it was found to be possible to tune the final roughness and obtain specimens with similar roughness repeatably. An example of such random specimen is shown on Figure 8-1; this one was obtained with an alumina powder with an average particle size of 10 µm. This approach could be used in future work to investigate the influence of random roughness on EHD lubrication.

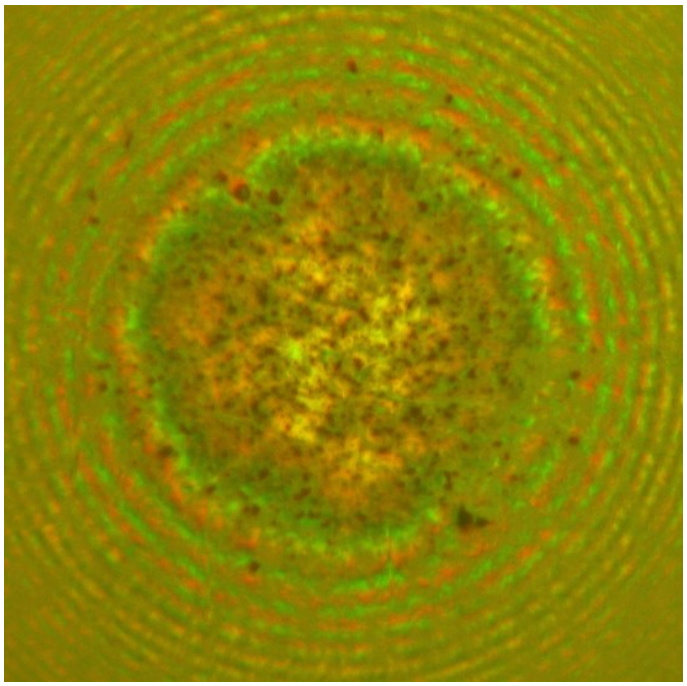

***Figure 8-1:** Example of a random roughness obtained with a barrelling machine using alumina powder with an average particle size of 10 µm*

Finally, more work could be done on the relationship between film thickness and friction in rough EHD contact. With the current set-up and methodology, the shear rate and the pressure can be reasonably estimated since film thickness data is available. Using a large set of traction

curves produced with a MTM, such that all the conditions of shear rate and pressure encountered in the rough EHD contact are covered, it could be possible to create shear stress maps. It would be interesting to see if the total friction can be predicted that way and also compare the shear stress distribution obtained that way with the one obtained using other techniques such as an infrared camera.

# Chapter 9 - References


1. Hertz H, “Über die Berührung Fester Elastischer Körper,” ***J. für die reine und Angew. Math.***, **92** (1881), pp. 156–171.

2. Johnson KL, *Contact Mechanics*. Cambridge University Press; 1987.

3. Chu PSY, Cameron A, “Pressure-Viscosity Characteristics of Lubricating Oils,” ***J. Inst. Pet.***, **48** (1962), pp. 147–150.

4. Roelands CJA, “Correlational Aspects of the Viscosity · Temperature · Presure Relationship of Lubricating Oils,” ***PhD Thesis, TU Delft***, (1966).

5. Crouch RF, Cameron A, “Viscosity-Temperature Equations for Lubricants,” ***J. Inst. Pet.***, **47** (1961), pp. 307–313.

6. Kligerman Y, Etsion I, Shinkarenko A, “Improving Tribological Performance of Piston Rings by Partial Surface Texturing,” ***J. Tribol.***, **127** (2005), pp. 632–638.

7. Thomas T, *Rough surfaces, second edition*. Imperial College Press; 1999.

8. Crook AW, “The lubrication of rollers,” ***Philos. Trans. R. Soc. Ser. A, Math. Phys. Sci.***, **250** (1958), pp. 387–409.

9. Archard JF, Kirk MT, “Lubrication at Point Contacts,” ***Proc. R. Soc. A Math. Phys. Eng. Sci.***, **261** (1961), pp. 532–550.

10. Dyson A, Naylor H, Wilson AR, “The Measurement of Oil-film Thickness in Elastohydrodynamic Contacts,” ***Proc. Inst. Mech. Eng.***, **180** (1965), pp. 119–134.

11. Heemskerk RS, Vermeiren KN, Dolfsma H, “Measurement of Lubrication Condition in Rolling Element Bearings,” ***ASLE Trans.***, **24** (1982), pp. 519–527.

12. Sibley LB, Orcutt FK, “Elasto-hydrodynamic Lubrication of Rolling-contact Surfaces,” ***ASLE Trans.***, **4** (1961), pp. 234–249.

13. Grubin AN, “Investigation of the Contact of Machine Components,” ***Cent. Sci. Res. Inst. Technol. Mech. Eng.***, **30** (1949).

14. Furey MJ, “Metallic Contact and Friction between Sliding Surfaces,” ***ASLE Trans.***, **4** (1961), pp. 1–11.

15. Crook AW, “Elastohydrodynamic Lubrication of Rollers,” ***Nature***, **190** (1961), pp. 1182–1183.

16. Johnston GJ, Wayte R, Spikes HA, “The Measurement and Study of Very Thin Lubricant Films in Concentrated Contacts The Measurement and Study of Very Thin Lubricant Films in Concentrated Contactso,” ***Trib. Trans.***, **34** (1991), pp. 187–194.

17. Cann PM, Spikes HA, Hutchinson J, “The Development of a Spacer Layer Imaging Method (SLIM) for Mapping Elastohydrodynamic Contacts,” ***Tribol. Trans.***, **39** (1996), pp. 915–921.

18. Luo J, Wen S, Huang P, “Thin Film Lubrication. Part I. Study on the Transition Between EHL and Thin Film Lubrication Using a Relative Optical Interference Intensity Technique,” ***Wear***, **194** (1996), pp. 107–115.

19. Reddyhoff T, Choo JH, Spikes H, Glovnea RP, “Lubricant Flow in an Elastohydrodynamic Contact Using Fluorescence,” ***Tribol. Lett.***, **38** (2010), pp. 207–215.

20. Reddyhoff T, Harper P, “Ultrasonic Measurement of Film Thickness in Mechanical Seals,” ***Seal. Technol.***, (2006), pp. 7–11.

21. Cameron A, Gohar R, “Theoretical and Experimental Studies of the Oil Film in Lubricated Point Contact,” ***Proc. R. Soc. A Math. Phys. Eng. Sci.***, **291** (1966), pp. 520–536.

22. Kirk MT, “Hydrodynamic Lubrication of ‘Perspex,’” ***Nature***, **194** (1962), pp. 965–966.

23. Gohar R, Cameron A, “The Mapping of Elastohydrodynamic Contacts,” ***ASLE Trans.***, **10** (1967), pp. 215–225.

24. Foord CA, Hammann WC, Cameron A, “Evaluation of Lubricants Using Optical Elastohydrodynamics,” ***ASLE Trans.***, **11** (1968), pp. 31–43.

25. Hariharan P, *Optical Interferometry (Second Edition)*. Academic Press; 2003.

26. Wedeven LD, “Optical Measurements in Elastohydrodynamic Rolling-Contact Bearings,” ***PhD Thesis, Univ. London***, (1970).

27. Kaneta M, Sakai T, Nishikawa H, “Effects of Surface Roughness on Point Contact EHL,” ***Tribol. Trans.***, **36** (1993), pp. 605–612.

28. Wedeven LD, Evans D, Cameron A, “Optical Analysis of Ball Bearing Starvation,” ***J. Lubr. Technol.***, **93** (1971), pp. 349–361.

29. Cusano C, Wedeven LD, “The Effects of Artificially-Produced Defects on the Film Thickness Distribution in Sliding EHD Point Contacts,” ***J. Lubr. Technol.***, **104** (1982), pp. 365–375.

30. Westlake FJ, Cameron A, “Fluid Film Interferometry in Lubrication Studies,” ***Nature***, (1967).

31. Westlake FJ, Cameron A, “A Study of Ultra-Thin Lubricant Films Using an Optical Technique,” ***Proc. Inst. Mech. Eng. Conf. Proc.***, **182** (1967), pp. 75–78.

32. Spikes HA, Guangteng G, “Properties of Ultra-Thin Lubricating Films Using Wedged Spacer Layer Optical Interferometry,” ***Tribol. Ser.***, **12** (1987), pp. 275–279.

33. Guangteng G, Spikes HA, “Boundary Film Formation by Lubricant Base Fluids,” ***Tribol. Trans.***, **39** (1996), pp. 448–454.

34. Smeeth M, Spikes HA, Gunsel S, “Boundary Film Formation by Viscosity Index Improvers,” ***Tribol. Trans.***, **39** (1996), pp. 726–734.

35. Guangteng G, Cann PM, Olver A V, Spikes HA, “Lubricant Film Thickness in Rough Surface, Mixed Elastohydrodynamic Contact,” ***J. Tribol.***, **122** (2000), pp. 65–76.

36. Kaneta M, Nishikawa H, Kameishi K, Sakai T, Ohno N, “Effects of Elastic Moduli of Contact Surfaces in Elastohydrodynamic Lubrication,” ***J. Tribol.***, **114** (1992), pp. 75–80.

37. Hartl M, Krupka I, Poliscuk R, Liska M, “An Automatic System for Real-Time Evaluation of EHD Film Thickness and Shape Based on the Colorimetric Interferometry,” ***Tribol. Trans.***, **42** (1999), pp. 303–309.

38. Gustafsson L, Hoglund E, Marklund O, “Measuring Lubricant Film Thickness with Image Analysis,” ***Proc. Inst. Mech. Eng.***, **208** (1994), pp. 199–205.

39. Hartl M, “Differential Colorimetry: Tool for Evaluation of Chromatic Interference Patterns,” ***Opt. Eng.***, **36** (1997), pp. 2384–2391.

40. Molimard J, “Etude Experimentale du Regime de Lubrification en Film Mince - Application aux Fluides de Laminage,” ***PhD Thesis, Insa Lyon***, (1999).

41. Choo JW, Olver A V, Spikes HA, “Influence of Surface Roughness Features on Mixed Film Lubrication,” ***Lubr. Sci.***, **15** (2003), pp. 219–232.

42. Marklund O, Gustafsson L, “Interferometry-based Measurements of Oil-film Thickness,” ***Proc. Inst. Mech. Eng. Part J J. Eng. Tribol.***, **215** (2001), pp. 243–259.

43. Jackson A, Cameron A, “An Interferometric Study of the EHL of Rough Surfaces,” ***A S L E Trans.***, **19** (1976), pp. 50–60.

44. Wedeven LD, Cusano C, “Elastohydrodynamic Film Thickness Measurements of Artificially Produced Surface Dents and Grooves,” ***A S L E Trans.***, **22** (1979), pp. 369–381.

45. Cusano C, Wedeven LD, “Elastohydrodynamic Film Thickness Measurements of Artificially Produced Nonsmooth Surfaces,” ***A S L E Trans.***, **24** (1979), pp. 1–14.

46. Krupka I, Hartl M, “The Effect of Surface Texturing on Thin EHD Lubrication Films,” ***Tribol. Int.***, **40** (2007), pp. 1100–1110.

47. Pettersson U, Jacobson S, “Textured Surfaces for Improved Lubrication at High Pressure and Low Sliding Speed of Roller/Piston in Hydraulic Motors,” ***Tribol. Int.***, **40** (2007), pp. 355–359.

48. Etsion I, “State of the Art in Laser Surface Texturing,” ***J. Tribol.***, **127** (2005), pp. 248–253.

49. Koszela W, Pawlus P, Galda L, “The Effect of Oil Pockets Size and Distribution on Wear in Lubricated Sliding,” ***Wear***, **263** (2007), pp. 1585–1592.

50. Mourier L, Mazuyer D, Lubrecht AA, Donnet C, “Transient Increase of Film Thickness in Micro-Textured EHL Contacts,” ***Tribol. Int.***, **39** (2006), pp. 1745–1756.

51. Kaneta M, Cameron A, “Effects of Asperities in Elastohydrodynamic Lubrication,” ***J. Lubr. Technol.***, **102** (1980), pp. 374–378.

52. Choo JW, “The Influence of Surface Roughness on the Lubrication of Concentrated Contacts,” ***PhD Thesis, Univ. London***, (2003).

53. Choo JW, Olver A V, Spikes HA, “The Influence of Transverse Roughness in Thin Film, Mixed Elastohydrodynamic Lubrication,” ***Tribol. Int.***, **40** (2007), pp. 220–232.

54. Hamrock BJ, Dowson D, *Ball Bearing Lubrication: Elastohydrodynamics of Elliptical Contacts*. Wiley; 1981.

55. Choo JW, Olver A V, Spikes HA, Dumont M-L, Ioannides E, “The Influence of Longitudinal Roughness in Thin-Film, Mixed Elastohydrodynamic Lubrication,” ***Tribol. Trans.***, **49** (2006), pp. 248–259.

56. Krupka I, Sperka P, Hartl M, Xue Jin S, Xiao Yang C, “Effect of Real Longitudinal Surface Roughness on Lubrication Film Formation within Line Elastohydrodynamic Contact,” ***Tribol. Int.***, **43** (2010), pp. 2384–2389.

57. Choo JW, Glovnea RP, Olver A V, Spikes HA, “The Effects of Three-Dimensional Model Surface Roughness Features on Lubricant Film Thickness in EHL Contacts,” ***J. Tribol.***, **125** (2003), pp. 533–542.

58. Mourier L, Mazuyer D, Lubrecht AA, Donnet C, Audouard E, “Action of a Femtosecond Laser Generated Micro-cavity Passing through a Circular EHL Contact,” ***Wear***, **264** (2008), pp. 450–456.

59. Lafountain AR, Johnston GJ, Spikes HA, “The Elastohydrodynamic Traction of Synthetic Base Oil Blends,” ***Tribol. Trans.***, **44** (2001), pp. 648–656.

60. De Vicente J, Stokes JR, Spikes HA, “Lubrication Properties of Non-adsorbing Polymer Solutions in Soft Elastohydrodynamic (EHD) Contacts,” ***Tribol. Int.***, **38** (2005), pp. 515–526.

61. Reddyhoff T, Spikes HA, Olver A V, “Improved Infrared Temperature Mapping of Elastohydrodynamic Contacts,” ***Proc. Inst. Mech. Eng. Part J J. Eng. Tribol.***, **223** (2009), pp. 1165–1177.

62. Yagi K, Kyogoku K, Nakahara T, “Measurements of Temperature Distributions around Longitudinally Grooved Rough Surfaces in Sliding Elastohydrodynamic Point Contacts,” ***Tribol. Trans.***, **49** (2006), pp. 482–489.

63. Reddyhoff T, Spikes HA, Olver A V, “Compression Heating and Cooling in Elastohydrodynamic Contacts,” ***Tribol. Lett.***, **36** (2009), pp. 69–80.

64. Spikes H, Jie Z, “History, Origins and Prediction of Elastohydrodynamic Friction,” ***Tribol. Lett.***, **56** (2014), pp. 1–25.

65. Bair S, Winer W, “Regimes of Traction in Concentrated Contact Lubrication,” ***J. Lubr. Technol.***, **104** (1982), pp. 382–386.

66. Evans CR, Johnson KL, “The Influence of Surface Roughness on Elastohydrodynamic Traction,” ***Proc. Inst. Mech. Eng.***, **201** (1987), pp. 145–150.

67. Nanbu T, Chiba N, Kano M, Yasuda Y, Ushijima K, “The Effect of Surface Texture on Traction Performance in a Traction Drive,” ***JSAE Rev.***, **24** (2003), pp. 135–140.

68. Jefferis JA, Johnson KL, “Traction in Elastohydrodynamic Contacts,” ***Proc. Inst. Mech. Eng.***, **182** (1967), pp. 281–291.

69. Nanbu T, Yasuda Y, Ushijima K, Watanabe J, Zhu D, “Increase of Traction Coefficient due to Surface Microtexture,” ***Tribol. Lett.***, **29** (2007), pp. 105–118.

70. Britton RD, Elcoate CD, Alanou MP, Evans HP, Snidle RW, “Effect of Surface Finish on Gear Tooth Friction,” ***J. Tribol.***, **122** (2000), pp. 354–360.

71. Klemz BL, “Stressed Measured by Photoelasticity in Lubricated Line Contact,” ***PhD Thesis, Univ. London***, (1970).

72. Jubault I, Mansot JL, Vergne P, Mazuyer D, “In-situ Pressure Measurements using Raman Microspectroscopy in a Rolling Elastohydrodynamic Contact,” ***J. Tribol.***, **124** (2002), pp. 114–120.

73. Himmel D, Mansot JL, Bercion Y, Lubrecht AA, “In Situ Raman Microspectrometry of Lubricated Tribologic Contacts. Part Two: Simultaneous Measurements of Pressure, Lubricant Film Thickness and Temperature Distributions in a Running EHD Contact,” ***Tribol. Lett.***, **41** (2010), pp. 131–144.

74. Höhn BR, Michaelis K, Kreil O, “Influence of Surface Roughness on Pressure Distribution and Film Thickness in EHL-Contacts,” ***Tribol. Int.***, **39** (2006), pp. 1719–1725.

75. Cann PM, Spikes HA, “Measurement of Pressure Distribution in EHL—Development of Method and Application to Dry Static Contacts,” ***Tribol. Trans.***, **48** (2005), pp. 474–483.

76. Kannel JW, Bell JC, Allen CM, “Methods for Determining Pressure Distributions in Lubricated Rolling Contact,” ***A S L E Trans.***, **8** (1965), pp. 250–270.

77. Safa MMA, Anderson JC, Leather JA, “Transducers for Pressure, Temperature and Oil Film Thickness Measurement in Bearings,” ***Sensors and Actuators***, **3** (1982), pp. 119–128.

78. Molimard J, Querry M, Vergne P, Krupka I, Hartl M, “Calculation of Pressure Distribution in EHD Point Contacts from Experimentally Determinated Film Thickness,” ***Tribol. Int.***, **38** (2005), pp. 391–401.

79. Dowson D, Higginson GR, Whitaker a V, “Elasto-hydrodynamic Lubrication: a Survey of Isothermal Solutions,” ***J. Mech. Eng. Sci.***, **4** (1962), pp. 121–126.

80. Olver A V, Guangteng G, Spikes HA, “Film Thickness and Pressure in Micro-EHD Contacts,” ***Tribol. Ser.***, **38** (2000), pp. 503–510.

81. Krupka I, Vrbka M, Vaverka M, Polscuk R, Hartl M, “Effect of Surface Dents on Contact Pressure in Elastohydrodynamic Contacts,” ***Proc. Inst. Mech. Eng. Part J J. Eng. Tribol.***, **223** (2009), pp. 683–693.

82. Love AEH, “The Stress Produced in a Semi-Infinite Solid by Pressure on Part of the Boundary,” ***Philos. Trans. R. Soc.***, **228** (1929), pp. 377–420.

83. Sayles RS, “Basic Principles of Rough Surface Contact Analysis using Numerical Methods,” ***Tribol. Int.***, **29** (1996), pp. 639–650.

84. Cole SJ, Sayles RS, “A Numerical Model for the Contact of Layered Elastic Bodies With Real Rough Surfaces,” ***J. Tribol.***, **114** (1992), pp. 334–340.

85. Ju Y, Farris TN, “Spectral Analysis of Two-Dimensional Contact Problems,” ***J. Tribol.***, **118** (1996), pp. 320–328.

86. Nogi T, Kato T, “Influence of a Hard Surface Layer on the Limit of Elastic Contact—Part I: Analysis Using a Real Surface Model,” ***J. Tribol.***, **119** (1997), pp. 493–500.

87. Kadiric A, Sayles RS, Ioannides E, “Thermo-Mechanical Model for Moving Layered Rough Surface Contacts,” ***J. Tribol.***, **130** (2008), pp. 1–14.

88. Lubrecht AA, Ioannides E, “A Fast Solution of the Dry Contact Problem and the Associated Sub-Surface Stress Field , Using Multilevel Techniques,” ***J. Tribol.***, **113** (1991), pp. 128–133.

89. Polonsky IA, Keer LM, “Fast Methods for Solving Rough Contact Problems: A Comparative Study,” ***J. Tribol.***, **122** (2000), pp. 36–41.

90. Kang YS, Sadeghi F, Ai X, “Debris Effects on EHL Contact,” ***J. Tribol.***, **122** (2000), pp. 711–720.

91. Reynolds O, “On the Theory of Lubrication and Its Application to Mr. Beauchamp Tower’s Experiments, Including an Experimental Determination of the Viscosity of Olive Oil,” ***Philos. Trans. R. Soc.***, (1886), pp. 191–203.

92. Lubrecht AA, Ten Napel WE, Bosma R, “Multigrid, an Alternative Method for Calculating Film Thickness and Pressure Profiles in Elastohydrodynamically Lubricated Line Contacts,” ***J. Tribol.***, **108** (1986), pp. 551–556.

93. Lubrecht AA, Ten Napel WE, Bosma R, “Multigrid, an Alternative Method of Solution for Two-Dimensional Elastohydrodynamically Lubricated Point Contact Calculations,” ***J. Tribol.***, **109** (1987), pp. 437–443.

94. Almqvist T, Larsson R, “The Navier – Stokes Approach for Thermal EHL Line Contact Solutions,” ***Tribol. Int.***, **35** (2002), pp. 163–170.

95. Hartinger M, Dumont M-L, Ioannides E, Gosman AD, Spikes HA, “CFD Modeling of a Thermal and Shear-Thinning Elastohydrodynamic Line Contact,” ***J. Tribol.***, **130** (2008), pp. 1–16.

96. Hirst W, Moore AJ, “The Elastohydrodynamic Behaviour of Polyphenyl Ether,” ***Proc. R. Soc.***, **344** (1975), pp. 403–426.

97. Johnson KL, Tevaarwerk JL, “Shear Behaviour in Elastohydrodynamic Oil Films,” ***Proc. R. Soc.***, **356** (1977), pp. 215–236.

98. Bair S, Winer WO, “Shear Strength Measurements of Lubricants at High Pressure,” ***J. Lubr. Technol.***, **101** (1979), pp. 251–257.

99. Evans CR, Johnson KL, “Regimes of Traction in Elastohydrodynamic Lubrication,” ***Proc. Inst. Mech. Eng.***, **200** (1985), pp. 313–322.

100. Bair S, “Recent Developments in High-Pressure Rheology of Lubricants,” ***Tribol. Ser.***, **30** (1995), pp. 169–187.

101. Chittenden RJ, Dowson D, Dunn JF, Taylor CM, “A Theoretical Analysis of the Isothermal Elastohydrodynamic Lubrication of Concentrated Contacts. I. Direction of Lubricant Entrainment Coincident with the Major Axis of the Hertzian Contact Ellipse,” ***Proc. R. Soc. A Math. Phys. Eng. Sci.***, **397** (1985), pp. 245–269.

102. Olver A V, Spikes HA, “Prediction of Traction in Elastohydrodynamic Lubrication,” ***Proc. Inst. Mech. Eng. Part J J. Eng. Tribol.***, **212** (1998), pp. 321–332.

103. Jacod B, Venner CH, Lugt PM, “A Generalized Traction Curve for EHL Contacts,” ***J. Tribol.***, **123** (2001), pp. 248–253.

104. Greenwood JA, Williamson JBP, “Contact of Nominally Flat Surfaces,” ***Proc. R. Soc.***, **295** (1966), pp. 300–319.

105. Greenwood JA, Tripp JH, “The Contact of Two Nominally Flat Rough Surfaces,” ***Proc. Inst. Mech. Eng.***, **185** (1970), pp. 625–633.

106. Tzeng ST, Saibel E, “Surface Roughness Effect on Slider Bearing Lubrication,” ***A S L E Trans.***, **10** (1967), pp. 334–348.

107. Christensen H, “Stochastic Models for Hydrodynamic Lubrication of Rough Surfaces,” ***Proc. Inst. Mech. Eng.***, **184** (1970), pp. 1013–1026.

108. Johnson KL, Greenwood JA, Poon Y, “A Simple Theory of Asperity Dynamic Lubrication Contact in Elastohydrodynamic Lubrication,” ***Wear***, **19** (1972), pp. 91–108.

109. Chow LSH, Cheng HS, “The Effect of Surface Roughness on the Average Film Thickness between Lubricated Rollers,” ***J. Lubr. Technol.***, (1976), pp. 117–124.

110. Patir N, Cheng HS, “An Average Flow Model for Determining Effects of Three-Dimensional Roughness on Partial Hydrodynamic Lubrication,” ***J. Lubr. Technol.***, **100** (1978), pp. 12–17.

111. Lubrecht AA, Ten Napel WE, Bosma R, “The Influence of Longitudinal and Transverse Roughness on the Elastohydrodynamio Lubrication of Circular Contacts,” ***J. Tribol.***, **110** (1988), pp. 421–426.

112. Lubrecht AA, Venner CH, “Elastohydrodynamic Lubrication of Rough Surfaces,” ***Proc. Inst. Mech. Eng. Part J J. Eng. Tribol.***, **213** (1999), pp. 397–404.

113. Hooke CJ, Venner CH, “Surface Roughness Attenuation in Line and Point Contacts,” ***Proc. Inst. Mech. Eng. Part J J. Eng. Tribol.***, **214** (2000), pp. 439–444.

114. Wang J, Venner CH, Lubrecht AA, “Amplitude Reduction in EHL Line Contacts under Rolling Sliding Conditions,” ***Tribol. Int.***, **44** (2011), pp. 1997–2001.

115. Jacod B, Venner CH, Lugt PM, “Influence of Longitudinal Roughness on Friction in EHL Contacts,” ***J. Tribol.***, **126** (2004), pp. 473–481.

116. Spikes HA, Cann PM, “The Development and Application of the Spacer Layer Imaging Method for Measuring Lubricant Film Thickness,” ***Proc. Inst. Mech. Eng. Part J J. Eng. Tribol.***, **215** (2001), pp. 261–277.

117. Krupka I, Hartl M, “Experimental Study of Microtextured Surfaces Operating Under Thin-Film EHD Lubrication Conditions,” ***J. Tribol.***, **129** (2007), pp. 502–508.

118. Venner CH, Morales-Espejel GE, “Amplitude Reduction of Small Amplitude Waviness in Transient Elastohydrodynamically Lubricated Line Contacts,” ***Proc. Inst. Mech. Eng. Part J J. Eng. Tribol.***, **213** (1999), pp. 487–504.

119. Archard JF, “The Temperature of Rubbing Surfaces,” ***Wear***, **2** (1958), pp. 438–455.

120. Spikes HA, Zhang J, “Reply to the Comment by Scott Bair, Philippe Vergne, Punit Kumar, Gerhard Poll, Ivan Krupka, Martin Hartl, Wassim Habchi, Roland Larson on ‘History, Origins and Prediction of Elastohydrodynamic Friction’ by Spikes and Jie in Tribology Letters,” ***Tribol. Lett.***, **58** (2015), pp. 1–6.

121. Lu X, Khonsari MM, Gelinck ERM, “The Stribeck Curve: Experimental Results and Theoretical Prediction,” ***J. Tribol.***, **128** (2006), p. 789.

122. Johnson KL, Greenwood JA, “Thermal Analysis of an Eyring Fluid in Elastohydrodynamic Traction,” ***Wear***, **61** (1980), pp. 353–374.